Electrochemical reduction of carbon dioxide and water to syngas ($CO + H_2$) at room temperature

by

Dr. Charles Delacourt

under the supervision of

Prof. John Newman

Environmental Energy Technologies Division,
Lawrence Berkeley National Laboratory

and

Department of Chemical Engineering,
University of California Berkeley

2006-2007

Abstract

Electrochemical reduction of carbon dioxide and water
to syngas ($CO + H_2$) at room temperature
by
Dr. Charles Delacourt
under the supervision of
Prof. John Newman

In chapter 1, a new electrolysis-cell design for simultaneous electrochemical reduction of CO_2 and H_2O to make syngas ($CO + H_2$) at room temperature (25°C) is developed, based on a technology very close to that of proton-exchange-membrane fuel cells (PEMFC), i.e., based on the use of gas-diffusion electrodes so as to achieve high current densities. While a configuration involving a proton-exchange membrane (Nafion) as electrolyte is shown to be unfavorable for CO_2 reduction, a modified configuration based on the insertion of a pH-buffer layer (aqueous $KHCO_3$) between the silver-based cathode catalyst layer and the Nafion membrane allows for a great enhancement of the cathode selectivity for CO_2 reduction to CO (ca. 30 mA/cm^2 at a potential of -1.7 to -1.75 V vs. SCE). A CO/H_2 ratio of 1/2, suitable for methanol synthesis, is obtained at a potential of ca. -2 V vs. SCE and a total current density of ca. 80 mA/cm^2. An issue that has been identified is the change in product selectivity upon long-term electrolysis. Results obtained with two other cell designs are also presented and compared.

In chapter 2, transport phenomena in an ion-exchange membrane containing both H^+ and K^+ are described using the multicomponent diffusion (extended Stefan-Maxwell) equations. Expressions for macroscopic transport parameters, i.e., conductivity, proton transference number, water electro-osmotic coefficient, and transport parameters characterizing diffusion at zero current, are derived as a function of the binary interaction parameters, $\mathscr{D}_{ij}$, used in the multicomponent transport equations. As experimental data for only four transport properties are available in the literature, the six $\mathscr{D}_{ij}$'s cannot be determined in

an unequivocal manner. It is in harmony with the data that is large, and linear variations of $ln(\mathscr{D}_{ij})$ with y_{HM} are assumed for the other $\mathscr{D}_{ij}$'s. Values for the slopes of those linear variations are refined by nonlinear least-square regression on the four experimental transport properties. General governing equations to describe completely transport in the membrane with H^+ and K^+ are presented, and the model is used with particular boundary conditions to describe the behavior of the membrane in the CO_2–H_2O electrolyzer. This provides some insights on macroscopic quantities such as the ohmic drop and water transport that are relevant for cell operation. This work is a preliminary study to the complete model of the electrolysis cell developed in chapter 4.

In chapter 3, experimental data for CO_2 (and H_2O) reduction to CO (and H_2) on flat gold and silver electrodes in $KHCO_3$ and $NaClO_4$ aqueous electrolytes and at room temperature are analyzed using a steady-state mathematical model. Rate constants and charge transfer coefficients for CO_2 and H_2O reduction reactions are derived from the experimental data, assuming that the rate-determining steps for CO_2 and H_2O reduction reactions are the formation of $CO_2^{\bullet -}$ and $H^{\bullet}$ radicals adsorbed at the electrode surface on both metal electrodes, respectively. It is found that CO_2 reduction to CO is positively shifted by ca. 370 mV on gold as compared to silver, while hydrogen evolution is positively shifted by only ca. 110 mV. This explains why higher CO current efficiencies are obtained on gold (ca. 90% for gold as compared to only ca. 68% for silver in potassium bicarbonate). The current fade for CO evolution at low electrode potential is related to the current increase for hydrogen evolution, which yields a high pH increase and CO_2 concentration decrease at the electrode surface. Finally, an analysis of data for various CO_2 partial pressures in equilibrium with the electrolyte is performed, in which the effect of acid-base reactions coupled with the CO evolution reaction is accounted for.

In chapter 4, the cell design for CO_2 reduction to CO (and simultaneous H_2O reduction to H_2) proposed in chapter 1, similar to a proton-exchange-membrane fuel cell but with a silver catalyst at the cathode and a pH buffer layer (aqueous $KHCO_3$) between the cathode

catalyst layer and the membrane, is tested with two different gold catalysts for which the overpotential for CO evolution is lower. The cell can operate at CO current densities as high as -135 mA/cm^2 (on supported Au catalyst). The general framework for treating equilibrated reactions and equilibrated interfacial mass transfer in a multiphase medium is derived and used to set forth a mathematical model of the electrolysis cell. At low current density, the model accounts for the experimental data pretty well, using the rate constant values obtained on flat Ag and Au electrodes in chapter 3. The influence of CO_2 partial pressure in the cathode gas channel and $KHCO_3$ concentration in the buffer layer are studied both experimentally and with the model, confirming that the rate-determining step for CO evolution reaction likely involves CO_2 species as the reactant, and not HCO_3^-. The model is further used to analyze various features of the cell operation that can explain the cell resistance increase and the decrease of CO efficiency at high current density. A decay in CO efficiency is observed upon operation, which is more severe on the supported Au catalyst. The model suggests that this decay in efficiency is not correlated with the electrolyte dilution in the buffer layer with operation time. Finally, the model is used to predict the behavior of a cell design based on a porous anion-exchange membrane instead of the aqueous buffer layer.

Contents

List of Figures

List of Tables

Acknowledgments

I am much indebted to my adviser, Prof. J. Newman (UCB and LBNL), who devoted a lot of his time to educate me on the mathematical modeling of electrochemical systems. Prof. Newman has always made himself available to discuss my work, even once I was back to my home country and was still working on the mathematical modeling part.

Also, I gratefully acknowledge:

- P. L. Ridgway (LBNL) for his great help in the experiments, especially the glass-cell experiments. P. Ridgway is a coauthor of two papers related to this work (see the List of Publications).

- J. B. Kerr (LBNL) for his help in providing guidelines for the design of the electrolysis cell, as well as for the high-performance-capillary-electrophoresis analyses. He is a coauthor of a paper related to this work (see the List of Publications).

- G. Mariansky, N. Taksatorn, T. Pica, and D. Bhatnagar (undergraduate students at UCB) for their help in the experiments.

- L. Beer (Postdoc at LBNL) for her help in high-performance-capillary-electrophoresis analyses.

- M. Fojas (graduate student at UCB) for interesting discussions on how to prepare membrane-electrode assemblies.

- V. Battaglia, V. Srinivasan, A. Weber, P. Ross, and R. Kostecki (LBNL) for interesting discussions related to this topic.

- Prof. Newman group members for all the interesting discussions and exchange of ideas, their support and friendship.

Financial support was provided by the Helios Solar Energy Research Center, which is supported by the Director, Office of Science, Office of Basic Energy Sciences of the U.S. Department of Energy under Contract No. DE-AC02-05CH11231, and by LBNL Laboratory Directed Research and Development funds.

List of Publications related to this work

1. Design of an electrochemical cell making syngas (CO + H_2) from CO_2 and H_2O reduction at room temperature
C. Delacourt, P. L. Ridgway, J. B. Kerr, and J. Newman
J. Electrochem. Soc., **155(1)**, B42-B45 (2008).

2. Mathematical Modeling of a Cation-Exchange Membrane Containing Two Cations
C. Delacourt and J. Newman
J. Electrochem. Soc., **155(11)**, B1210-B1217 (2008).

3. Mathematical Modeling of CO_2 Reduction to CO in Aqueous Electrolytes. I.- Kinetic Study on Planar Silver and Gold Electrodes
Charles Delacourt, Paul Ridgway, and John Newman
In proofs, *J. Electrochem. Soc.*, Oct. 2010.

4. Mathematical Modeling of CO_2 Reduction to CO in Aqueous Electrolytes II.- Study of an Electrolysis Cell Making Syngas (CO + H_2) from CO_2 and H_2O Reduction at Room Temperature
C. Delacourt and J. Newman
In proofs, *J. Electrochem. Soc.*, Oct. 2010.

Chapter 1

Design of an electrochemical cell making syngas (CO + H_2) from CO_2 and H_2O reduction at room temperature

1.1 Introduction

Renewable energies such as solar, wind, or hydro are good candidates as alternatives to fossil fuels since they are CO_2-neutral and therefore do not contribute to the greenhouse effect. Their main drawback (especially solar and wind) is that they are not available on demand, and therefore the energy produced needs to be stored. One option is to store this energy as a liquid fuel, such as methanol. This can be achieved by converting solar energy into electricity through photovoltaic arrays, and then by using this electricity to produce fuels by electrolysis. Various hypothetical pathways are sketched in figure 1.1. The top one involves a photovoltaic device, which makes the electricity to electrolyze water to H_2 (and O_2 as a

by-product). The hydrogen is reacted with CO_2 in a water-gas-shift reactor to make CO (and H_2O), then the CO/H_2 mixtures are reacted to form methanol. Note that these two latter operation units can be combined together to make methanol directly from CO_2 and H_2.[1] The second pathway combines the water electrolyzer together with a water-gas-shift reactor into an electrochemical reactor able to reduce simultaneously H_2O to H_2 and CO_2 to CO. The example of methanol synthesis has been chosen, but the syngas can be used for making various kinds of liquid fuels, such as synthetic diesel, by using the Fischer-Tropsch process, for instance. In the last hypothetical process, methanol would be directly produced by an electrochemical cell fed with CO_2 and H_2O.

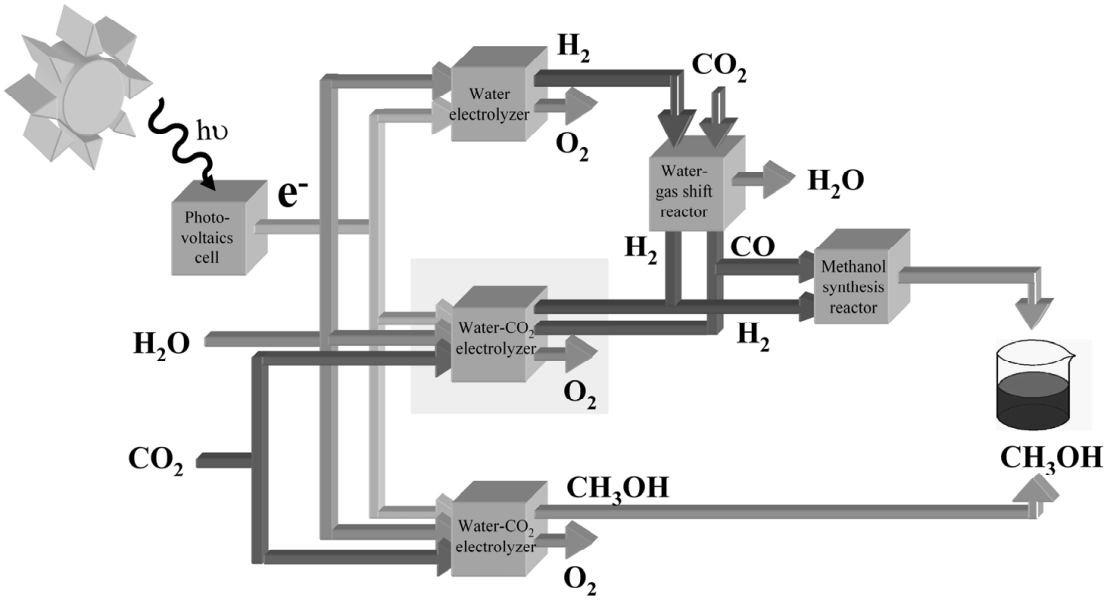

Figure 1.1: Various electrochemically-based pathways for the synthesis of methanol from carbon dioxide.

Besides intensive research on photovoltaic devices in order to improve their efficiency while lowering their cost for large-scale applications, effort has to be concentrated on the design of high efficiency electrochemical cells through the development of improved catalysts and their incorporation into efficient engineering platforms designed for high-current-density operation. Our work has been focused on the electrochemical cell for the preparation of

syngas through the reduction of CO_2 and H_2O. This work is based on the numerous contributions in the literature on CO_2 reduction and on a trial-and-error method. However, a more useful goal is to optimize the design through the use of mathematical modeling that includes the kinetics of heterogeneous and homogeneous reactions as well as mass-transport parameters of the various species, and which is developed in the next chapters. This goal will improve our understanding of the complex system, and more specifically of the factors that control the selectivity of the parallel reactions of H_2 and CO evolution.

In the first section, basic design considerations are laid out for the cell design. Then, after a description of the experimental set-up and techniques, results obtained with silver-based cathodes in different cell configurations are presented and discussed.

1.2 General design considerations

A "low-temperature" technology (room temperature in this study) was chosen, although high-temperature electrolysis (800 to 900°C) could be an attractive alternative, and is currently under consideration by other groups.[2] Because of the relatively low solubility of CO_2 in water under ambient conditions (ca. 0.033 mol/L), a technology based on gas-diffusion electrodes was used since it alleviates mass-transport limitations across the gas/liquid interface and to the catalyst surface, thereby allowing the cell to operate at higher current densities. The use of an ion-exchange membrane as the electrolytic medium is convenient so as to limit gas crossover resulting in a decrease of the current efficiency of the cell. Finally, catalysts capable of reduction of CO_2 to CO at low overpotentials needed to be selected. From reports on the use of various metal catalysts for CO_2 reduction in aqueous media,[3–9] it was determined that different CO_2-reduction products could be obtained depending on the nature of the catalyst (Figure 1.2). This has also been discussed in many reviews on CO_2 electroreduction.[10–12] Ag and Au turn out to be highly selective for CO_2 reduction to CO.[3,8,9] To a certain extent, Zn could be used (advantages in terms of cost) although it is less

selective, as formate is formed in substantial amounts together with CO.[3,8,9] Furthermore, as the H_2 evolution is favorable with the Ag and Au catalysts in aqueous media, substantial amounts of H_2 are obtained together with CO at those catalysts. If one expects to feed the gaseous effluents directly from the cell into a fuel-synthesis reactor, the current efficiencies of CO and H_2 need to be controlled so as to obtain an appropriate CO/H_2 ratio for whatever fuel we want to make (for instance, $CO/H_2 = 1/2$ for methanol). This ratio is generally dependent upon a variety of operating parameters such as current density, feed rate, pH and temperature, and therefore this makes the optimization of such a system relatively complex. Finally, for long-term durability considerations, side reactions must be minimized, particularly those that lead to degradation of the catalyst (and result in a change of its selectivity for the products) or electrolyte structures.

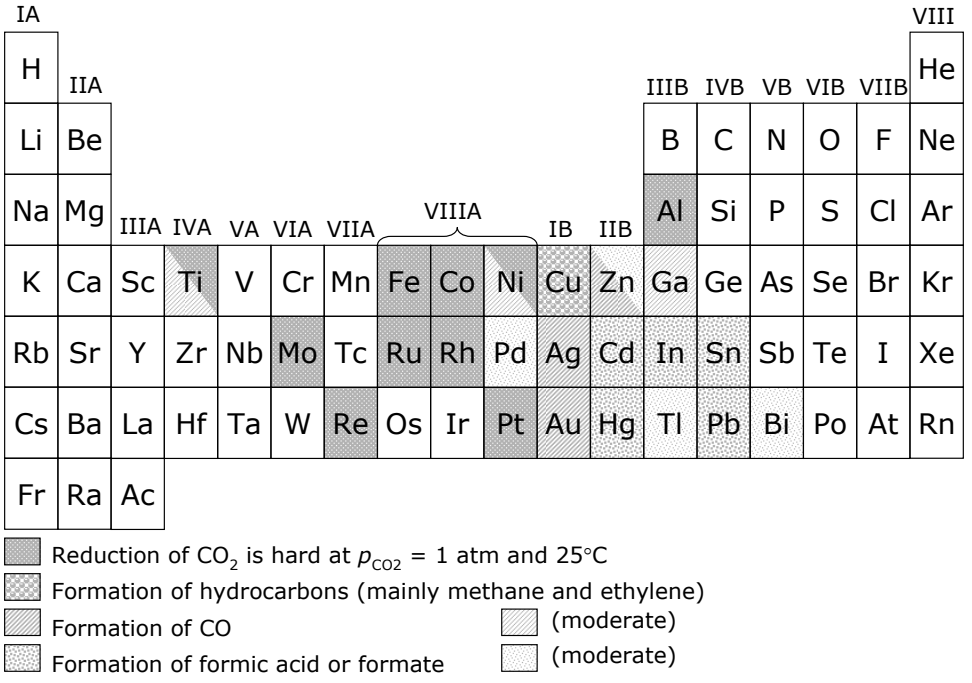

Figure 1.2: Classification of the different metal catalysts for CO_2 reduction according to the reduction products.

1.3 Experimental

1.3.1 Cell description and experimental Setup

The electrochemical cell and the experimental set-up are quite similar to systems that are used for fuel-cell studies. A diagram of this set-up is given in Figure 1.3. The cell is composed of two blocks in which channels have been machined and are used as current collectors as well as to feed gaseous (or liquid) reactants to the anode and cathode. The cathode block is made of graphite (treated to make it nonporous). Since it was found that graphite oxidized upon electrolysis at the anode, polytetrafluoroethylene (PTFE) was chosen as material for the anode block. A platinum screen placed between the PTFE block and the electrode was used as current collector. It was connected to the external circuit by means of a platinum wire through the PTFE block. The membrane-electrode assembly (MEA, surface 1 cm^2) was placed between the 2 blocks. The whole sandwich was pressed between two aluminum frames with eight bolts of diameter 0.635 cm fastened with a torque of 8.5 N m. A saturated-calomel reference electrode (SCE) was used and was connected to the electrolytic medium at the cathode side through a salt bridge (3 mm away from the cathode), consisting of 1.5 mm-internal-diameter plastic tubing filled with 0.5 M $KHCO_3$ supported on glass fiber (except for the cell configuration involving a proton-exchange membrane as electrolyte, in which case 0.5 M HCl was used).

Carbon dioxide from a compressed tank (4.8 research grade, 99.998%) was purified by means of an activated carbon filter (Supelcarb HC, Sigma Aldrich). The CO_2 flowrate to the cathode was set to ca. 20 mL/min (referred to room temperature and pressure conditions, i.e. 25±1°C and 1.013 bar, resp.) by a mass-flow controller (MKS type M100B and 1259C/2259C piloted by a channel readout type 247C) which was initially calibrated for this particular gas. For the cell configurations involving solely a $CO_{2(g)}$ flow, CO_2 was humidified at room temperature prior to entering the cathode. For the cell configuration involving a two-phase flow of $CO_{2(g)}$ and an aqueous $KHCO_3$ solution, CO_2 was directly mixed with the $KHCO_3$

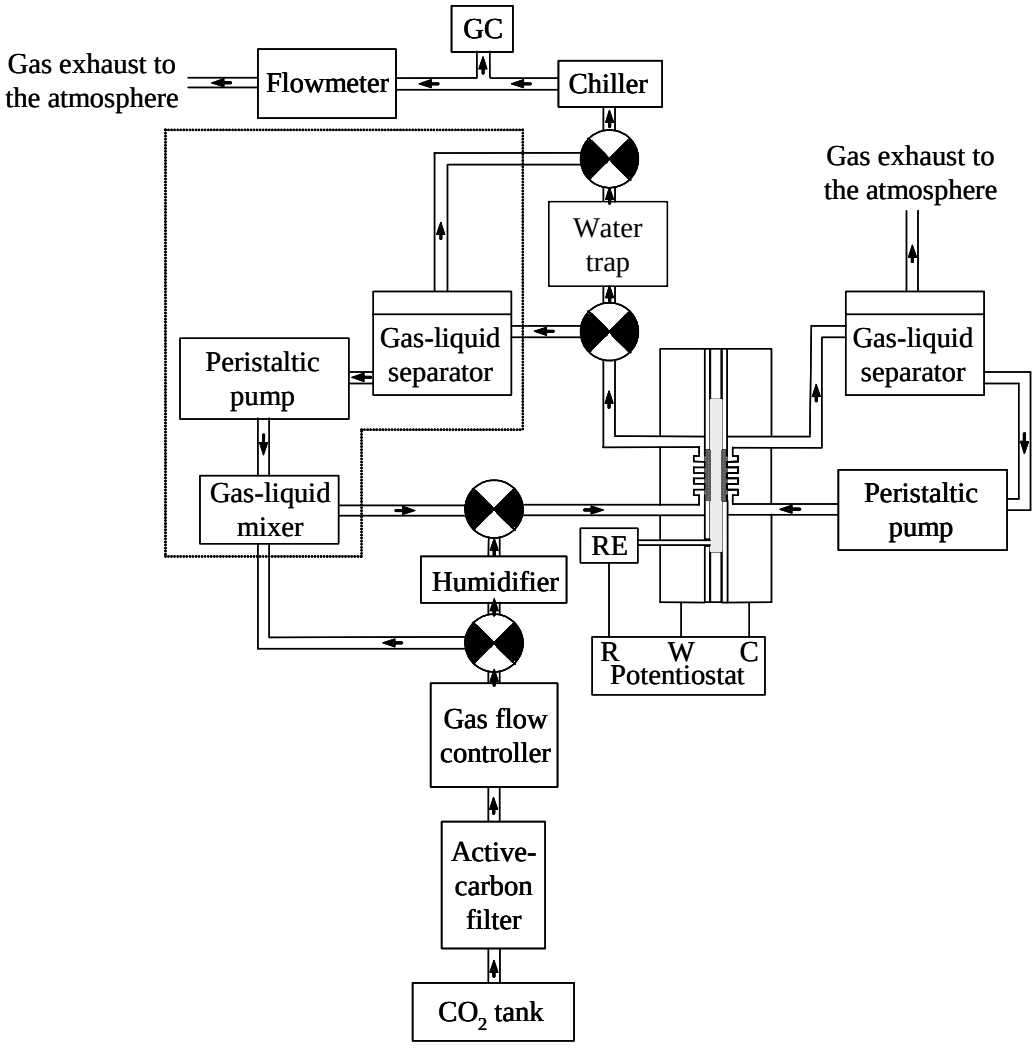

Figure 1.3: Process and instrument diagram for the laboratory-scale production of syngas from CO_2 and H_2O reduction. The part surrounded by dotted lines is used only for the cell based on a cation-exchange membrane in the K^+-form.

solution just before entering the cathode side of the cell. $KHCO_3$ solution was recirculated at a flow rate of 27 mL/min by using a peristaltic pump (Cole Parmer Instruments, model no. 7520-25) between the gas/liquid mixer and a gas/liquid separator from which the gas was recovered for analysis. For both configurations, the exhausted gas from the cathode (or from the gas/liquid separator) was then introduced into a "chiller" (or condenser) in order

to lower the water partial pressure before being introduced into a gas chromatograph (Micro GC 3000, Agilent Technologies) equipped with a molecular sieve column (capillary column, 320 μm diam., 10 m length, molecular sieve 12 μm) and a thermal-conductivity detector (TCD). At the cathode outlet, a flow meter was used to measure accurately the gas flowrate to allow measurement of faradaic efficiencies. At the anode, a liquid flow composed of pure deionized (DI) water (or an aqueous KOH solution for the cell configuration based on a Nafion membrane in the K^+-form) was recirculated by means of a peristaltic pump with a flowrate of 27 mL/min between the electrode and a gas/liquid separator, allowing gaseous products to exhaust into the atmosphere.

Galvanostatic electrolyses were conducted at room temperature and pressure by means of a potentiostat (Gamry Instruments, PCI4 potentiostat/galvanostat/ZRA) recording both the cathode potential and the anode potential versus the reference electrode. Current density is expressed as the total current divided by the geometric surface area of the electrodes (1 cm^2 for all cells). The faradaic (or current) efficiency η_i of a gaseous product i is determined by means of

$$\eta_i = \frac{n_i F x_i F_m}{I}, \tag{1.1}$$

where n_i is the number of electrons exchanged, F Faraday's constant, x_i the mole fraction of the gas i in the gaseous mixture analyzed (also equal to the volume fraction if gases are assumed to be ideal), F_m the molar flow rate in mol/s, and I the total current (A). The molar flow rate is derived from the volume flow rate F_v by the relation $F_m = pF_v/RT$, with p the atmospheric pressure (Pa), R the ideal gas constant, and T the temperature (K).

When a cell based on a buffer layer was used, the aqueous electrolyte supported in the glass fibers was analyzed for formate, oxalate, and other possible anionic CO_2-reduction products by means of high-performance capillary electrophoresis (HPCE, Agilent 3D Capillary Electrophoresis System) with a method detailed by Geiser et al.[13] Because these analyses were carried out at the end of the electrolyses, only an average faradaic efficiency could be determined (in contrast to the faradaic efficiencies of gases, for which an instantaneous value

is obtained) according to

$$\langle \eta_i \rangle = \frac{n_i c_i V_s F}{It}, \tag{1.2}$$

where n_i, F, and I have the same definition as in equation 1.1, c_i is the concentration of the analyte in mol/L, V_s is the total volume of the sample in L (containing the electrolyte from the buffer layer), and t the total duration of the electrolysis in s.

1.3.2 Preparation of membrane-electrode assemblies

Regardless of the cell design, the catalyst used at the cathode was silver (pure unsupported silver with an average particle diameter of 1 μm, Alfa Aesar Inc., or supported silver on vulcan XC-72, E-TEK Inc.), and the catalyst used at the anode was an unsupported Pt/Ir 1/1 alloy (E-TEK, Inc.). Furthermore, both anodes and cathodes were designed so that the loading of catalyst in the catalyst layer was close to 8 to 10 mg/cm^2. The proportions of the other components in the catalyst layer were: x wt.% acetylene black carbon (this percentage being referred to the total weight of catalyst + carbon, and ranging from 0 to 60 according to the experiments) + 20 wt.% of a polymer the selection of which depends on the cell configuration (this percentage being referred to the total weight of the catalyst layer). When the electrode was in contact with a layer of an aqueous electrolyte supported in glass fibers (Whatman GF/D, 2.7 μm pore size), the polymer consisted of PTFE initially in the form of an aqueous suspension (TE3859, du Pont de Nemours Inc.). When the electrode was in contact with an ion-exchange membrane (except for the cell based on a Nafion membrane in the K^+-form for which PTFE-based gas-diffusion electrodes were used), the polymer was of the same nature as the membrane material. For the cation-exchange membrane (Nafion 117, 1100 g/eq, 175 μm thickness in dry conditions, du Pont de Nemours, Inc.), a 5 wt.% solution of perfluorosulfonic acid–polytetrafluoroethylene copolymer (Sigma Aldrich, Inc.) was employed. For the anion-exchange membrane (polyethersulfone-based membrane, FAA type, 30 to 50 μm thickness in dry conditions, Fumatech, GmbH), the company provided solutions of two precursors that react to form the polymer by cross-linkage when mixed

together in a defined amount.

The catalyst, the polymer solution or dispersion, and, when used, the carbon, were mixed together, leading to a dispersion that was spread or painted onto a woven microporous gas-diffusion layer (LT 1200 W, mean pore size 0.9 μm, 260 to 270 μm thickness, E-TEK Inc.). At the anode side where no gas-diffusion layer was employed, the catalyst layer was deposited on the ion-exchange membrane by using the decal-transfer procedure.[14] In order to ensure a good ionic contact between the membrane and the catalyst layer, a hot pressing of these two parts at 450 bars was performed for 5 minutes at 125°C for the cation-exchange membrane and at 100°C for the anion-exchange membrane. Because the ionomer form of the anion-exchange membrane (AEM) was in the Cl^--form, the whole MEA was subsequently immersed for 1 hour at room temperature in a 1 M KOH solution, rinsed thoroughly, and finally immersed for 10 minutes in DI water.

1.4 Results and discussion

1.4.1 Cells based on a fuel-cell-type configuration

In view of the general design considerations listed above, an electrochemical cell having a design similar to a proton-exchange-membrane fuel cell (PEMFC) appeared to be very suitable. A schematic of such a cell is shown in Figure 1.4a. The expected electrochemical reactions are

$$CO_2 + 2H^+ + 2e^- \rightleftharpoons CO + H_2O, \quad U^\theta = -0.104 \text{ V} \tag{1.3}$$

$$2H^+ + 2e^- \rightleftharpoons H_2, \qquad U^\theta = 0 \text{ V} \tag{1.4}$$

at the cathode and

$$2H_2O \rightleftharpoons O_2 + 4H^+ + 4e^-, \quad U^\theta = 1.229 \text{ V} \tag{1.5}$$

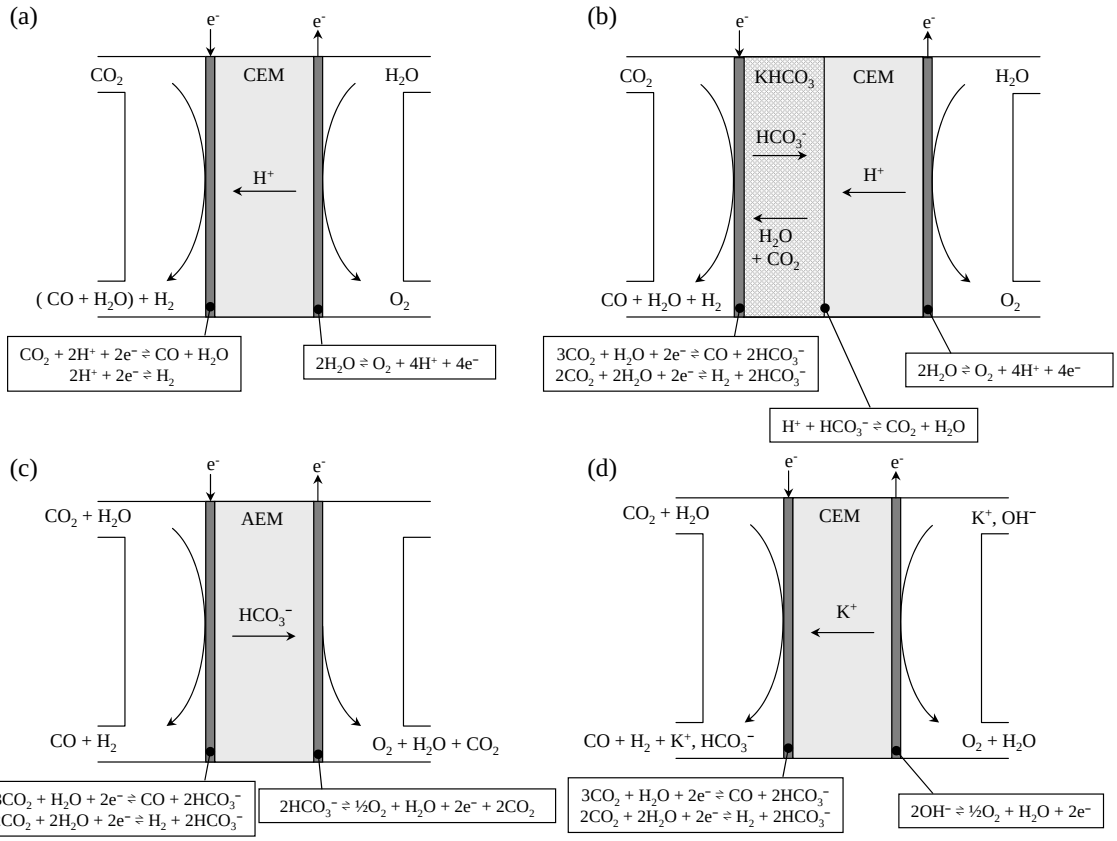

Figure 1.4: (a) Electrochemical cell with a cation-exchange membrane (CEM) as electrolyte. Its design is similar to a PEMFC cell. (b) Modified electrochemical cell with a pH-buffer layer of aqueous $KHCO_3$ between the cathode catalyst layer and the cation-exchange membrane. (c) Electrochemical cell with an anion exchange membrane (AEM) as electrolyte. CO_2 is evolved at the anode and needs to be further separated from the O_2. (d) Electrochemical cell based on a cation-exchange membrane in the K^+-form. K^+-based aqueous electrolytes need to be circulated at cathode and anode sides. An auxiliary process is required to transfer back K^+ ions from the catholyte to the anolyte. For simplification, reactions in configurations (b), (c), and (d) are based on the assumption that all the acid-base reactions are equilibrated.

at the anode. U^θ is the value of the standard electrode potential referred to the hydrogen electrode. This leads to the overall cell reactions for CO, H_2, and O_2 evolution

$$CO_2 \rightleftharpoons CO + 1/2O_2 \tag{1.6}$$

$$H_2O \rightleftharpoons H_2 + 1/2O_2. \tag{1.7}$$

An MEA based on a proton-exchange membrane was built according to the procedure detailed in the experimental section, and was fed with humidified CO_2 at the cathode and pure water at the anode so as to be tested for CO_2 and H_2O reduction. Unfortunately, no gaseous CO_2-reduction products were detected by gas chromatography, and the current efficiency for H_2 was almost 100% at a current density of 20 mA/cm^2 (Figure 1.5). This result is not very surprising if compared with the few publications dealing with CO_2 reduction using a cation-exchange membrane in the H^+ form as an electrolyte. CO_2 reduction on various metals deposited on Nafion was investigated by Cook et al. in solid-polymer-electrolyte cells, with H_2 (10% in Ar) being oxidized on Pt deposited on the anode side of the membrane.[15–17] They mainly focused on methane formation, and the faradaic efficiencies they reported were quite low: ca. 2.6% faradaic efficiency for CH_4 on Cu (which is the best metal catalyst for CO_2 reduction to hydrocarbons), and $< 1\%$ on the other metals (Ni, Ru, Rh, Pd, Ag, Re, Os, Ir, Pt, and Au). Mainly hydrogen was produced. Dewulf et al. reported a total current efficiency of ca. 20% for CO_2 reduction on copper electrodes deposited on Nafion, the CO2-reduction products being mainly methane and ethylene.[18] Importantly, in contrast with Cook's report, the Nafion was in contact with an aqueous solution of H_2SO_4 at the anode side, and increasing the concentration of H_2SO_4 led to a decrease of the faradaic efficiency for CO_2 reduction. In view of all these results, it is likely that the acidity of the membrane shifts the cathode selectivity toward hydrogen evolution.

1.4.2 Buffer-layer-type cells

A literature survey shows that most CO_2 reduction studies were performed in only slightly acidic or slightly basic solutions, and mainly in aqueous potassium bicarbonate ($KHCO_3$).[3,6–9] Therefore, we modified the initial fuel-cell-like configuration by inserting a layer of aqueous $KHCO_3$ between the cathode catalyst layer and the cation-exchange membrane (Figure 1.4b). This layer of thickness 800 μm is made of an inert support (glass fibers) impregnated with an aqueous $KHCO_3$ solution (0.5 mol/L). Because the pH at the cathode

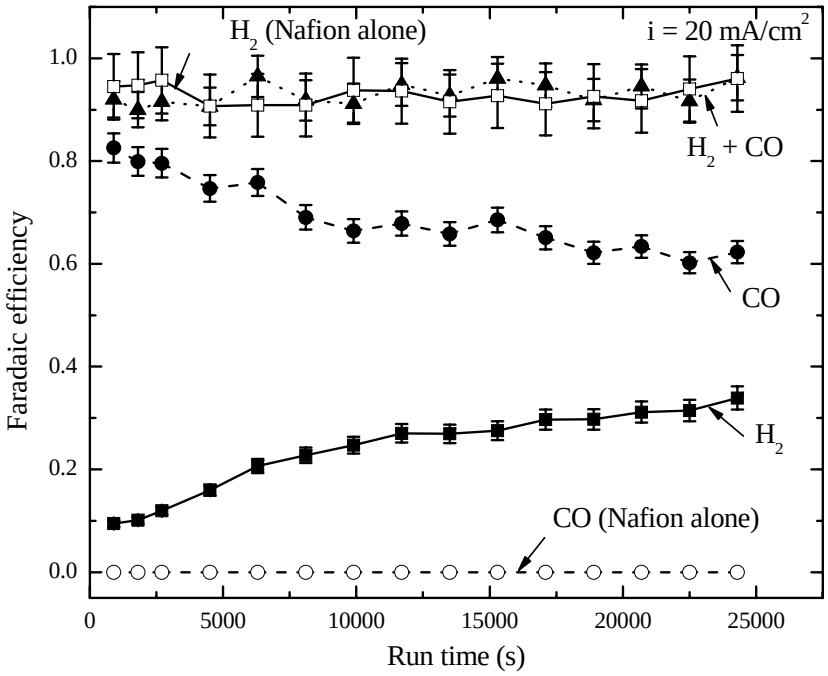

Figure 1.5: Current efficiencies of CO and H_2 obtained for a galvanostatic electrolysis at 20 mA/cm^2 with the fuel-cell-like configuration (open symbols) and with the modified configuration based on a buffer layer of aqueous $KHCO_3$ (filled symbols). Cathode: 10 mg/cm^2 unsupported Ag; flow of 20 mL/min CO_2. Anode: 7.7 mg/cm^2 unsupported Pt/Ir alloy; flow of 27 mL/min recirculated DI water. Detail on error bars is given in Appendix 1.6.1.

is not acidic, the electrochemical reactions of H_2 and CO evolution are written with a proton donor such as H_2O or HCO_3^- rather than H^+

$$CO_2 + H_2O + 2e^- \rightleftharpoons CO + 2OH^-, \quad U^\theta = -0.932 \text{ V} \tag{1.8}$$

$$2H_2O + 2e^- \rightleftharpoons H_2 + 2OH^-, \quad U^\theta = -0.828 \text{ V} \tag{1.9}$$

Note, however, that no hypothesis is made on the mechanisms of both CO and H_2 evolution, which is beyond the scope of this chapter. Reactions 1.8 and 1.9 involve H_2O as proton donor, but HCO_3^- could be used instead. Also, reaction 1.8 may involve HCO_3^- instead of CO_2 as a possible reactant. As these two electrochemical reactions lead to an increase of the

local pH at the electrode, they are coupled with homogeneous acid-base reactions

$$OH^- + CO_2 \rightleftharpoons HCO_3^- \tag{1.10}$$

$$OH^- + HCO_3^- \rightleftharpoons CO_3^{2-} + H_2O \tag{1.11}$$

The anode reaction can be written the same way as it is for the fuel-cell configuration (reaction 1.5). Near the interface between the cation-exchange membrane and the buffer layer, acid-base reactions between the protons coming from the anode and basic species from the buffer layer are expected

$$H^+ + HCO_3^- \rightleftharpoons CO_2 + H_2O \tag{1.12}$$

$$H^+ + CO_3^{2-} \rightleftharpoons HCO_3^- \tag{1.13}$$

$$H^+ + OH^- \rightleftharpoons H_2O \tag{1.14}$$

If we make the assumption that the acid-base reactions are equilibrated, i.e., infinitely fast, the overall reactions for CO and H_2 evolution at the cathode could be written

$$3CO_2 + H_2O + 2e^- \rightleftharpoons CO + 2HCO_3^-, \quad U^\theta = -0.567 \text{ V} \tag{1.15}$$

$$2CO_2 + 2H_2O + 2e^- \rightleftharpoons H_2 + 2HCO_3^-, \quad U^\theta = -0.463 \text{ V} \tag{1.16}$$

Under this assumption, the protons coming from the anode react with bicarbonate ions according to reaction 1.12. The advantage of this notation is that it is independent of the proton donor or the form of CO_2 which is reduced.

A cell with a buffer layer (aqueous 0.5 M $KHCO_3$ supported on glass fiber) between the cathode and the cation-exchange membrane was built and fed with humidified CO_2 at the cathode and pure water at the anode, before being tested for CO_2 and H_2O reduction. Current efficiencies of CO and H_2 obtained with such a cell when operating at 20 mA/cm^2 are shown in Figure 1.5. A large increase in the selectivity for CO evolution over the fuel-

cell-like configuration is observed, with a CO efficiency of 82% and the H_2 efficiency roughly corresponding to the complementary value. A decrease of the CO current efficiency upon run time of ca. 3%/h is observed, together with an increase of the H_2 efficiency. This could be related to a poisoning of the electrode and to a change of the electrolytic medium (buffer layer); this will be further illustrated and discussed below. As a consequence of these results, it appears that the history of the electrode and of the electrolyte is of particular relevance for such studies. Therefore, for each electrolysis performed, a new cell was assembled with a new cathode as well as with a fresh buffer solution. In Figure 1.6, partial current densities of CO and H_2, their sum, and the total current density after 15 minutes of electrolysis are plotted as a function of the cathode potential vs. SCE (which has been corrected for ohmic drop). A potential dependence of the current efficiency is observed, with H_2 evolution becoming predominant at negative potential values (high current densities). The maximum partial current density of CO evolution is ca. 30 mA/cm^2 at a potential of -1.7 to -1.75 V vs. SCE. A CO/H_2 ratio of 1/2, suitable for subsequent methanol synthesis, is obtained at a potential of -2 V vs. SCE and a total current density of ca. 80 mA/cm^2.

The average current efficiencies of soluble CO_2-reduction products, i.e., formate $HCOO^-$ and oxalate $C_2O_4^{2-}$, are listed in Table 1.1. The values are very low ($< 1.5\%$) and cannot account for the difference between the sum of CO and H_2 current efficiencies and 100%, given in table 1.1 as well. It is possible that other CO_2-reduction products were formed and were not identified, which would account for the observed discrepancy (see Appendix 1.6.2 for more discussion).

At this point, it is interesting to compare the present results with those reported in the literature for a Ag catalyst and aqueous $KHCO_3$ as electrolyte; some of them are summarized in Table 1.2. To our knowledge, only one paper deals with CO_2 reduction at a Ag-loaded gas-diffusion electrode.[19] Unfortunately, no current-density values are given. Most of the data have been obtained on flat Ag metallic electrodes. As a general trend, the current efficiencies of CO and H_2 are fairly consistent with each other (except the report by Yano

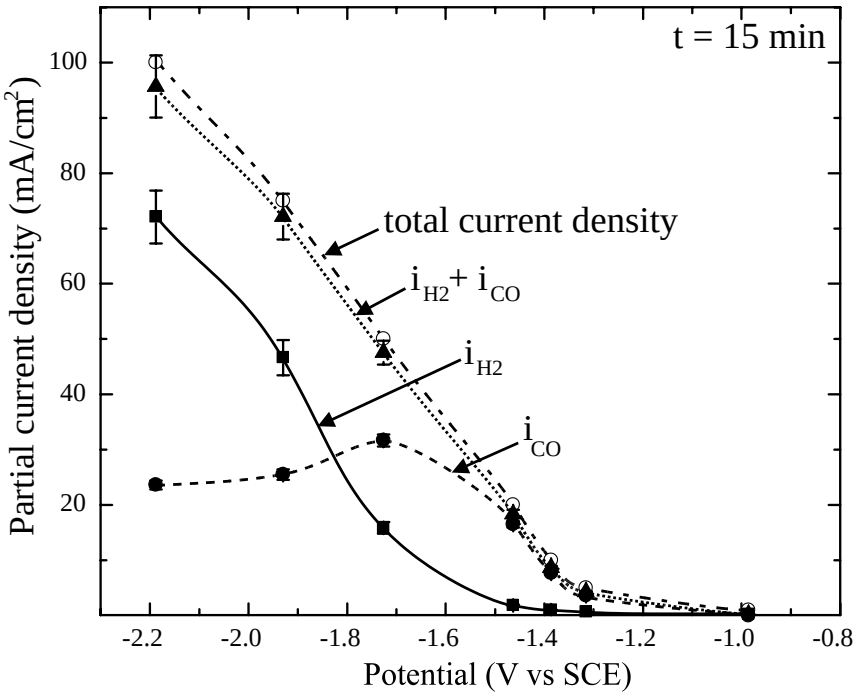

Figure 1.6: Partial current densities of CO and H_2 obtained with the buffer-layer-based cell after 15 min galvanostatic electrolyses. Cathode: ca. 8.5 mg/cm^2 unsupported Ag; flow of 20 mL/min CO_2. Anode: ca. 8.2 mg/cm^2 unsupported Pt/Ir alloy; flow of 27 mL/min recirculated DI water. Potentials are corrected for ohmic drop. Detail on error bars is given in Appendix 1.6.1.

et al.[20] for which a lower CO efficiency is obtained) and with our results (see Figure 1.6). However, a correlation with formate efficiencies is not straightforward. The improvement in using gas-diffusion electrodes is clearly evidenced by comparing current densities, which are roughly one order of magnitude higher than for planar electrodes.

A further evaluation of this type of cell design is possible by looking at the overall performance of the cells. To this end, Figure 1.7 shows plots of the potentials of both electrodes and cell potential as a function of the current density as well as the energy efficiency ε, which is defined as the thermal energy obtained by the combustion of CO and H_2 over

Table 1.1: Average $HCOO^-$ and $C_2O_4^{2-}$ current efficiencies during galvanostatic electrolyses with the buffer-layer-based cell, obtained from analysis of the buffer-layer electrolyte. Cathode: ca. 8.5 mg/cm^2 unsupported Ag; flow of 20 mL/min CO_2. Anode: ca. 8.2 mg/cm^2 unsupported Pt/Ir alloy; flow of 27 mL/min recirculated DI water.

Current density (mA/cm^2)	Average $HCOO^-$ efficiency (%)	Average $C_2O_4^{2-}$ efficiency (%)	$100 - \langle\eta_{CO}\rangle - \langle\eta_{H_2}\rangle$ (%)
1	1.4	—	79.3
5	0.6	0.1	18.7
10	0.3	—	13.9
20	0.3	—	6.9
50	0.7	< 0.05	2.8
75	1.4	< 0.05	2.1
100	0.4	< 0.05	2.0

Table 1.2: Literature survey of the typical current efficiencies of CO, $HCOO^-$, and H_2 obtained during electrolyses on Ag electrodes in aqueous $KHCO_3$ electrolyte saturated with pure $CO_{2(g)}$ at room temperature and pressure. For convenience, potentials are expressed versus SCE.

Electrode	Electrolyte	Current efficiencies	ref.
Ag-based GDEs	0.2 M $KHCO_3$	65 to 80% CO and ca. 15% $HCOO^-$ between -1.74 and -3.04 V vs. SCE ; current density is not given; H_2 efficiency not determined experimentally.	19
Ag planar electrode	0.5 M $KHCO_3$	61.4 to 89.9% CO, 1.6 to 4.6% $HCOO^-$, and 10.4 to 35.3% H_2 at -1.69 V vs. SCE, and 5 mA/cm^2.	3
Ag planar electrode	0.1 M $KHCO_3$	81.5% CO, 0.8% $HCOO^-$, and 12.4% H_2 at -1.61 V vs. SCE and 5 mA/cm^2.	9
Ag planar electrode	0.05 M $KHCO_3$	30% CO, 16% $HCOO^-$, and 50% H_2 at -2.2 V vs. SCE; current density is not given.	7
Ag planar electrode	0.1 M $KHCO_3$	64.7% CO and 28% H_2 at -1.64 V vs. SCE and 1.5 mA/cm^2.	8
Ag planar electrode	0.5 M $KHCO_3$	15 to 20% CO and 60 to 65% H_2 at -2.04 V vs. SCE; current density is not given.	20

the electrical energy consumed during electrolysis. It is calculated according to

$$\varepsilon = \frac{\Delta rH^0_{CO}\eta_{CO} + \Delta rH^0_{H_2}\eta_{H_2}}{2FV} \tag{1.17}$$

with ΔrH^0_{CO} and $\Delta rH^0_{H_2}$ the enthalpies of reactions 1.6 and 1.7 in J/mol, respectively (ΔrH^0_{CO} = 283 kJ/mol and $\Delta rH^0_{H_2}$ = 286 kJ/mol, if liquid H_2O is involved, i.e., higher heating value) and V is the total cell potential (V). At low current density (5 to 20 mA/cm^2), the energy efficiency is almost constant. Unfortunately, it decreases quickly as the current density further increases. This suggests that, besides an improvement of the cathode selectivity towards CO_2 reduction, an improvement of the overall cell performance is required if one wants to meet the targets for a practical implementation.

For the design of such an electrolysis cell, durability is also of major relevance. In Figure 1.8, the faradaic efficiencies of CO and H_2 are reported as a function of the current density for 3 different run times, namely 15, 165, and 285 min. A decrease of the CO efficiency and a corresponding increase of the H_2 efficiency are clearly observed upon time. Noteworthy is that this effect is mainly observed in the low-current-density region ($\leq$ 50 mA/cm^2), for which the initial CO efficiencies are the largest. The origin of this effect has not been clarified yet. This could be possibly due to a change in the buffer layer composition. Although we have shown that formate and oxalate were not formed in significant amounts during the electrolysis, other by-products may accumulate upon electrolysis and thus modify the properties of the buffer layer. An alternative explanation is a poisoning effect of the catalyst. Poisoning effects during CO_2 electroreduction are reported in several papers.[20–24] According to Kostecki et al.,[21] an increase of the total current is observed upon potentiostatic electrolysis, which means that the modified surface of Ag further promotes catalysis of the H_2 evolution reaction (if reaction surface area is assumed constant). Note that this effect, which would translate into a lowering of the cell potential, has not been observed in our constant-current experiments. Some authors are not in agreement with regards to the nature of the poisoning species. Shiratsuchi and Nogami[22] as well as Yano et al.[20] ascribe this poisoning to graphitic carbon deposition at the electrode formed by further reduction of CO according to the reaction

$$CO + H_2O + 2e^- \rightleftharpoons C + 2OH^-, \quad U^\theta = -0.310 \text{ V} \tag{1.18}$$

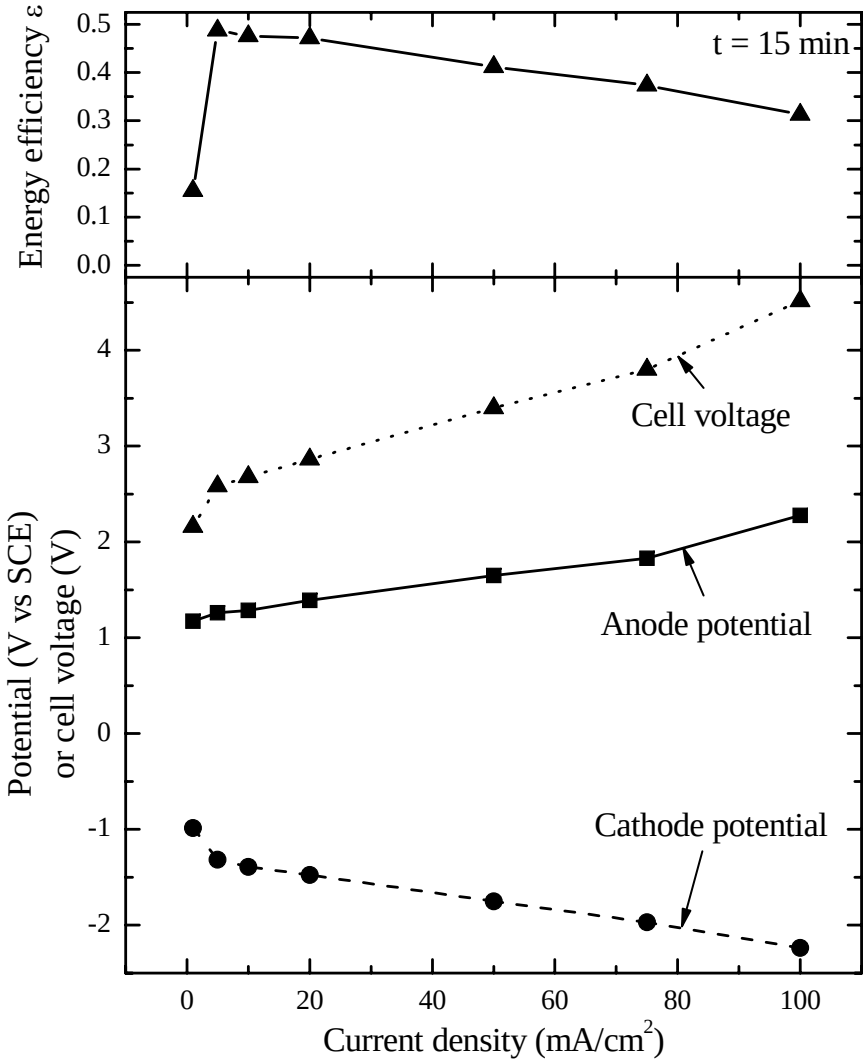

Figure 1.7: Energy efficiency of the overall cell (top) and potential of cathode, anode, and total cell (bottom) obtained with the buffer-layer-based cell after 15 min galvanostatic electrolyses. Same conditions for cathode and anode as in figure 1.6. Potentials are not corrected for ohmic drop.

Kostecki et al. proposed that it would be most likely due to an organic adsorbate, such as formaldehyde HCHO.[21] In order to suppress this poisoning effect, some authors have proposed the use of pulse techniques, aimed at desorbing the intermediates before they can further be reduced to a "poison" by shifting periodically the potential to a less negative

value.[22,23] An analogous method, based on periodic cyclic voltammetric scans, was also envisaged.[21] More recently, a comprehensive study by Hori et al.[24] of CO_2 reduction on Cu electrodes in $KHCO_3$ electrolyte has shown that a poisoning of the electrode was due to the presence of Fe and Zn impurities in the electrolyte, which deposit at the electrode surface and progressively induce a change in product selectivity. This poisoning was mostly avoided by a pre-electrolysis of their electrolytic solutions.

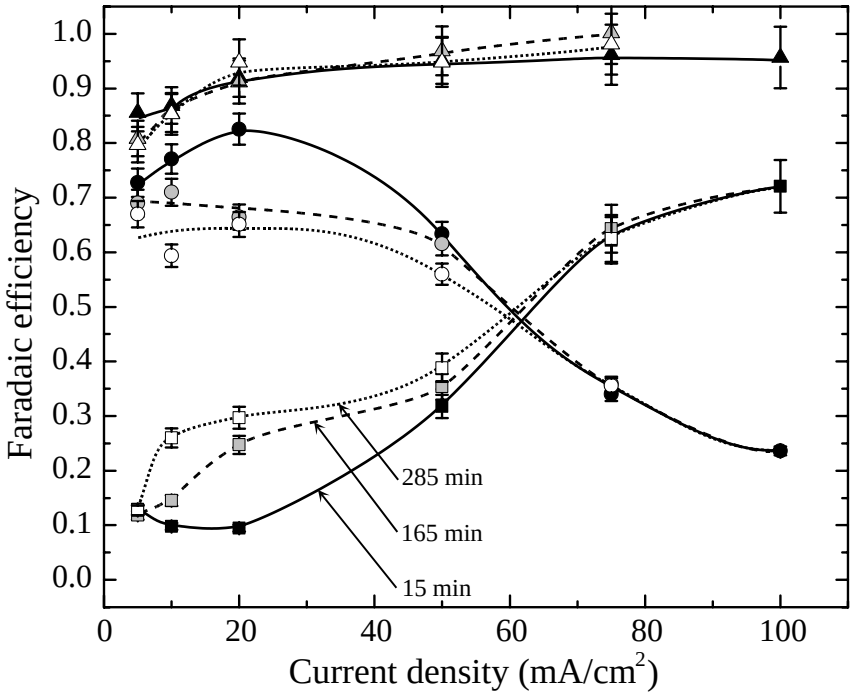

Figure 1.8: Current efficiencies of CO, H_2, and CO + H_2 obtained with the buffer-layer-based cell for different galvanostatic electrolysis run times. Same conditions for cathode and anode as in figure 1.6. Detail on error bars is given in Appendix 1.6.1.

Finally, the influence of the composition of the cathode catalyst layer on the product selectivity and the performance has been studied by varying the carbon content, the Ag-loadings being kept constant at ca. 10.5 mg/cm^2. In Figure 1.9, the CO current efficiencies are given for different compositions as a function of the electrolysis time. For the electrodes based on unsupported silver, an optimum in terms of CO current efficiency is observed for 20 wt.% carbon added. Above this optimum, the addition of carbon leads to a lower initial

CO current efficiency, accompanied by a quicker decrease with time. In every case, the complementary current efficiency corresponds to hydrogen evolution. No further investigation has been carried out to identify the origin of this product selectivity change with time. The optimum value of 20 wt.% carbon is likely to correspond to a trade-off between the porosity of the electrode for efficient CO_2 mass-transport to the catalyst sites and side reactions occurring on carbon (or on possible carbon impurities) Hydrogen evolution can be foreseen as a possible side reaction. One could also envisage side reactions leading to species that may affect the silver-catalyst selectivity. However, these experiments do not support a poisoning of the Ag electrode by metal impurities in the electrolyte as detailed by Hori et al.,[24] as a dependence of the poisoning on carbon content would not be straightforward in this case.

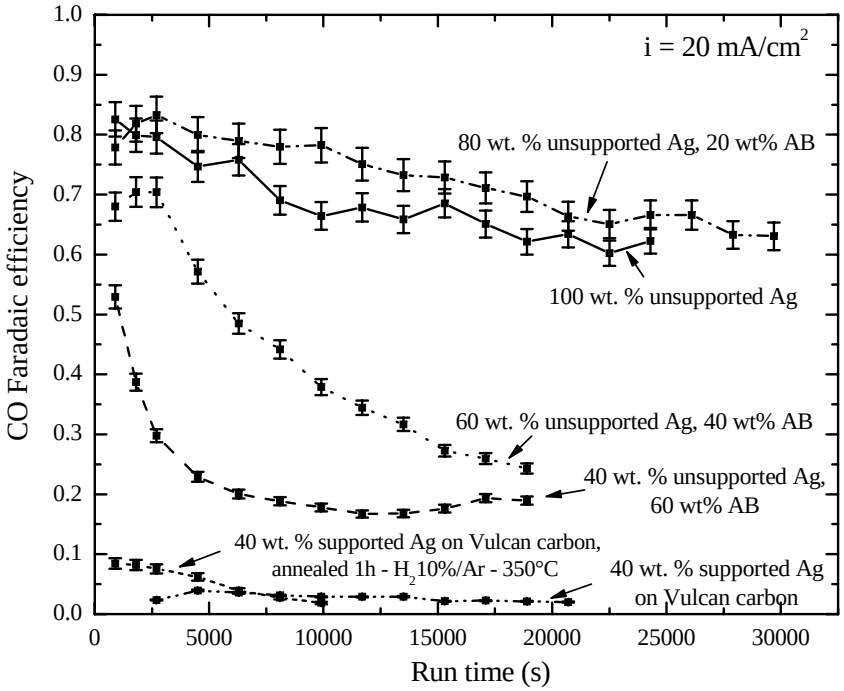

Figure 1.9: Current efficiencies of CO obtained with the buffer-layer-based cell for various compositions of the Ag-based cathode catalyst layer. Cathode: ca. 10.5 mg/cm^2 unsupported Ag; flow of 20 mL/min CO_2. Anode: ca. 9.0 mg/cm^2 unsupported Pt/Ir alloy; flow of 27 mL/min recirculated DI water. Detail on error bars is given in Appendix 1.6.1.

1.4.3 Alternative cell configurations

Besides the cell using a buffer layer between the cathode catalyst layer and the cation-exchange membrane, two other cell designs have been studied and are illustrated in Figures 1.4c and 1.4d. The cell in Figure 1.4c uses an anion-exchange membrane as electrolyte. This should overcome the problem of using a cation-exchange membrane in the H^+ form, as detailed previously. The reactions at the cathode are expected to be similar to those for the buffer-layer-based cell. HCO_3^-, CO_3^{2-}, and OH^- are possible charge carriers in the anion-exchange membrane. At the anode, water oxidation takes place according to overall half-reactions which depend on the nature of the charge carriers

$$2OH^- \rightleftharpoons 1/2O_2 + H_2O + 2e^-, \quad U^\theta = 0.401 \text{ V} \tag{1.19}$$

$$2HCO_3^- \rightleftharpoons 1/2O_2 + H_2O + 2e^- + 2CO_2, \quad U^\theta = 0.765 \text{ V} \tag{1.20}$$

$$CO_3^{2-} \rightleftharpoons 1/2O_2 + 2e^- + CO_2, \quad U^\theta = 0.692 \text{ V} \tag{1.21}$$

Note that, if the acid-base reactions 1.10 and 1.11 are assumed equilibrated, the overall reactions at the cathode are 1.15 and 1.16 for CO and H_2 evolution, respectively, and therefore HCO_3^- is the only charge carrier in the membrane, and oxygen evolution occurs according to reaction 1.20. Because bicarbonate and carbonate ions are possible charge carriers, CO_2 release at the anode is expected (see reactions 1.20 and 1.21). For an overall process prospective, this means that CO_2 has to be separated from the oxygen by-product, and eventually reinjected at the cathode side.

The anion-exchange membrane used is a polyethersulfone-based membrane with bicyclic ammonium groups (Figure 1.10). An MEA with 9.1 mg/cm^2 unsupported silver at the cathode and 8.4 mg/cm^2 unsupported Pt/Ir alloy at the anode was assembled, and fed with humidified CO_2 at the cathode and pure water at the anode before being tested for CO_2 and H_2O reduction. Figure 1.11 clearly shows that mainly H_2 is evolved at the cathode, with CO efficiency around 3% at all currents. This result, although very different from what

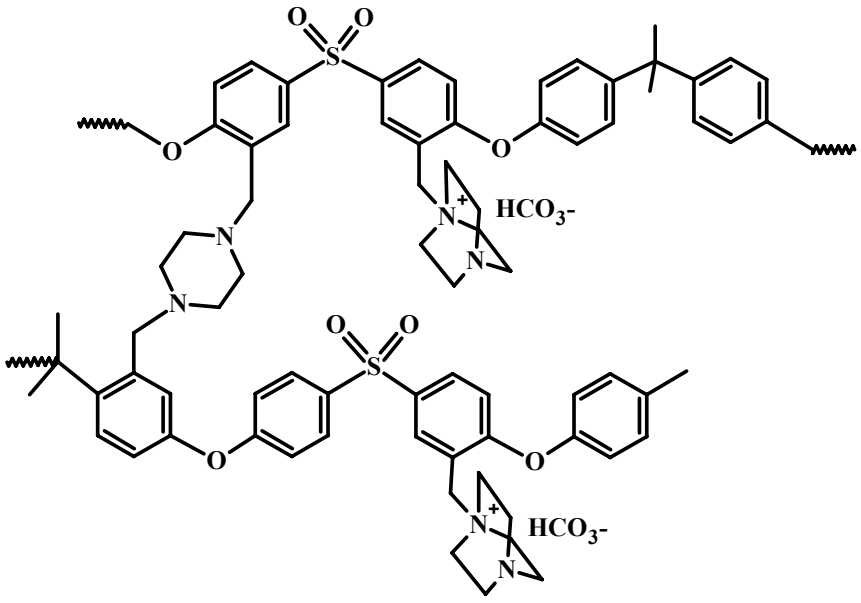

Figure 1.10: Chemical structure of the anion-exchange membrane used in the experiments, which is a polyethersulfone-based membrane with bicyclic ammonium groups.

is obtained with the buffer-layer configuration, is encouraging since CO was detected, in contrast with what we obtained using a proton-exchange membrane. These values are much smaller than the ones reported in the literature by Hori et al. for Ag-coated-AEM electrodes, for which the results are similar to those obtained with the buffer-layer configuration in terms of current efficiency.[25] The reasons for the low CO current efficiencies observed with this cell configuration are not clear; although the partial current density for CO evolution seems to follow a Tafel behavior (see Figure 1.11), it is possible that CO_2 mass-transport limitations due to a low porosity of the catalyst layer could be detrimental for the cathode selectivity toward CO evolution. This statement is supported by the high CO current efficiencies reported by Hori et al.,[25] in which the electrode is made of a porous coating of pure silver directly on the AEM, without the use of any binder. A parametric study of the catalyst-layer composition would be useful in order to understand the observed behavior.

Another cell design tested is based on a Nafion membrane in the K^+ form, and therefore aqueous solutions containing potassium ions need to be circulated at both electrodes. Since

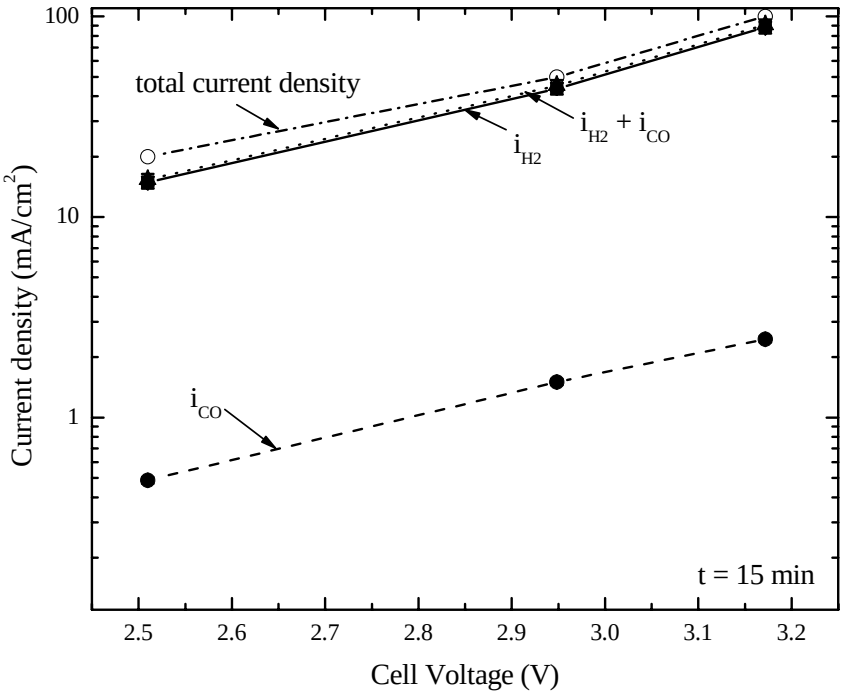

Figure 1.11: Partial current densities of CO and H_2 obtained with the cell based on an anion-exchange membrane after 15 min galvanostatic electrolyses. Cathode: 9.1 mg/cm^2 unsupported Ag; flow of 20 mL/min CO_2. Anode: ca. 8.4 mg/cm^2 unsupported Pt/Ir alloy; flow of 27 mL/min recirculated DI water. The same MEA was used for all the electrolyses. Potentials are not corrected for ohmic drop. Detail on error bars is given in Appendix 1.6.1.

it is well-known that the kinetics of O_2 evolution reaction (OER) is favored in basic media, an aqueous KOH solution has been used at the anode, as detailed in Figure 1.4d. Then, the corresponding reaction involves hydroxide ions according to reaction 1.19. At the cathode, an aqueous solution of $KHCO_3$ was circulated together with a CO_2 flow mixed with the solution just at the inlet of the cell. The series of reactions at the cathode will be the same as for the design with a buffer layer or the one involving an anion-exchange membrane. One of the main issues of this configuration is that the concentration of KOH in the anode compartment decreases upon electrolysis while that of $KHCO_3$ in the cathode compartment increases. Therefore, an auxiliary process would have to be engineered in order to allow the system to operate at steady-state. Also, this design based on electrolytic solutions at

the electrodes constitutes another drawback since leakage (or shunt) currents are expected if several cells are stacked using a bipolar configuration.

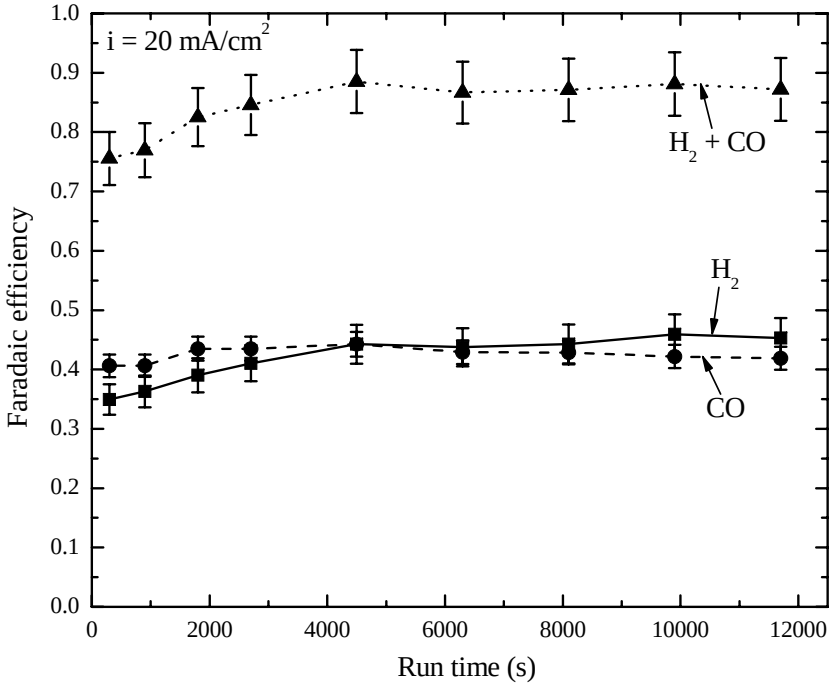

Figure 1.12: Current efficiencies of CO and H_2 obtained with the configuration based on a Nafion membrane in the K^+-form. Cathode: 10.5 mg/cm^2 unsupported Ag; flow of 20 mL/min CO_2. mixed with 27 mL/min recirculated aqueous $KHCO_3$ (0.5 M). Anode: flow of 27 mL/min recirculated aqueous KOH (0.5 M). Detail on error bars is given in Appendix 1.6.1.

A cell was assembled by using such a configuration, and an electrolysis experiment was performed at 20 mA/cm^2 (Figure 1.12). The cathode potential was -1.42 V vs. SCE (corrected for ohmic drop), and the CO efficiency was ca. 40%. This latter value was maintained for at least 3 h electrolysis, which is quite satisfactory. However, the selectivity of the cathode for the CO_2 reduction is lower than with the buffer-layer-based cell (ca. 80%), which is probably due to CO_2 mass-transport issues related with the use of a two-phase flow ($CO_{2(g)}$ + 0.5 M $KHCO_3$) at the cathode in the present configuration.

1.5 Conclusion

Several cell configurations for simultaneous reduction of H_2O and CO_2 to make syngas have been presented, and their performance compared. For convenience in the comparison, the study was limited to silver as the cathode catalyst, which is one of the best metal catalysts for CO_2 reduction to CO, according to the literature. While a configuration derived from PEMFC was shown to be unfavorable for CO_2 reduction, leading to H_2 evolution only, a modified configuration based on the insertion of a pH-buffer layer (aqueous $KHCO_3$) between the cathode catalyst layer and the Nafion membrane allows for a great enhancement of the cathode selectivity for CO_2 reduction to CO. This buffer layer is likely to prevent an excessive amount of protons from reaching the cathode, in which case hydrogen is solely evolved. Even though this design is not suitable in its present form for a practical application (cell resistance too high due to a thick buffer layer, possible flushing out of the electrolyte from the buffer layer due to a net water flux from anode to cathode, see chapter 4), these results provide guidelines for material scientists to design ionomers which provide the right conditions for making syngas. In a following, this cell design is selected and studied in more detail using a mathematical model that takes into account a complete set of heterogeneous and homogeneous reactions having either finite kinetics or considered equilibrated, together with mass transport of the soluble and gaseous species in the buffer layer and the gas-diffusion electrodes and of H^+, K^+, and H_2O in the membrane (chapter 4).

In order to simplify the buffer-layer-based system by combining the properties of the buffer layer and the membrane, a cell configuration involving an anion-exchange membrane in the HCO_3^--form was developed and was shown to be more efficient than the proton-exchange membrane for CO_2 reduction to CO. We believe that this configuration can be significantly improved by an optimization of the catalyst layer to lower CO_2 mass-transport limitations. Note that similar cell configurations recently studied for alkaline polymer-fuel-cell application[26] also suffer from the difficulty of designing catalyst layers with high porosity while ensuring a good ionic contact of the catalyst particles.

Finally, we proposed another cell design consisting in the use of a Nafion membrane in the K^+-form, which allows the oxygen-evolution reaction (OER) to be carried out in alkaline conditions, more favorable for kinetic reasons, and CO_2 reduction to CO at the cathode. However, besides the need for recycling the catholyte and anolyte solutions in an auxiliary process, this design requires a careful optimization of the two-phase flow at the cathode. This latter difficulty probably explains why the performance obtained with this configuration in terms of CO faradaic efficiency is lower than with the buffer layer.

1.6 Appendices

1.6.1 Error bars on current efficiencies

The error bars on current efficiencies and partial current densities were obtained at a confidence level of 95% by combining the errors on both the flowrate measurement and the GC analysis. The error on the flowrate was estimated using Student distribution ($n-1$ degrees of freedom) from a series of n measurements performed during each electrolysis.

The error on the GC analysis was estimated for each product (CO and H_2) using a weighted least-squares linear regression of the corresponding calibration curves. The weighting factors correspond in fact to the inverse of the variance of each calibration point. From estimates of the actual error on a few calibration points, we have shown that the mean-square deviation was almost proportional to x_i; therefore we have set the weighting factor to be proportional to $1/(x_i)^2$ systematically, with x_i the mole fraction of gas i for each standard.

1.6.2 Hypotheses for the sum of current efficiencies < 1

The hypotheses for the sum of current efficiencies < 1 at low current density are listed here:

- Gas leaks: Although the cell is tested for leaks by pressurizing it prior to experiments, small cell leaks may result in a lowering of the current efficiencies. Furthermore, leaks are probably more of a concern at low current density.

- Unidentified side products: The experimental methods for gas phase and buffer layer analysis allow for the detection of most of the possible side products. Products such as gaseous hydrocarbons can be detected by GC (molecular sieve column). Soluble compounds, such as salts of organic acids (e.g., glyoxalate, acetate) are in principle detected by HPCE. For neutral species (e.g., methanol, ethanol, formaldehyde), a few (non-systematic) GC experiments were carried out on the electrolyte (buffer layer) but nothing was detected.

- Product crossover followed by chemical reaction: A few simple calculations were made, so as to figure out whether gas crossover (CO and/or H_2 from cathode to anode and O_2 from anode to cathode) followed by direct chemical reaction could be at the origin of the sum of current efficiencies < 1. Calculations show that crossover is minimal (e.g., 6.5 10^{-3}% for H_2 crossover). Transport of soluble CO_2-reduction products might be pointed out as well; if these products are anions, they should not be present in the cation-exchange membrane and should accumulate in the buffer layer and be detected. Crossover of neutral products is by diffusion only; therefore, it is probably negligible as well.

List of Symbols

c_i	concentration of species i (mol/L)
F	Faraday's constant (96,487 C/mol)
F_m	molar flowrate (mol/s)

F_v	volume flowrate (mol/m^3)
I	total current (A)
n_i	number of electrons exchanged for the formation of reduction product i
p	atmospheric pressure (Pa)
R	ideal-gas constant (8.314 J/mol K)
t	total duration of the electrolysis (s)
T	temperature (K)
U^θ	standard potential referred to the hydrogen electrode (V)
V	total cell potential (V)
V_s	total volume of sample (L)
x_i	mole fraction of product i
ΔrH^0	enthalpy of reaction (J/mol)
ε	energy efficiency
η_i	current efficiency of reduction product i

Chapter 2

Mathematical modeling of a cation-exchange membrane containing two cations

2.1 Introduction

Ion-exchange membranes have been used in numerous industrial processes involving separations and in electrochemical systems. Perfluorinated sulfonic acid (PFSA) membranes are well-known since they have been extensively employed in the chlor-alkali electrolysis process, with the most recognizable one being Nafion from du Pont de Nemours. Later on, these membranes have found another interest as the electrolyte in polymer-electrolyte fuel cells (PEFCs). They have been the object of numerous experimental and modeling studies aimed at understanding their complex transport properties.[27,28] Various types of models were developed, ranging from microscopic,[29] based on statistical mechanics and molecular dynamics, to macroscopic, based on phenomenological transport phenomena. Among the macroscopic models, the hydraulic ones often consider the membrane as composed of two

phases (hydrophilic ionic channels and hydrophobic backbone),[30,31] and the diffusion-type models assume a single phase for the membrane system.[32,33] Composite models combining the hydraulics and diffusion features by the use of two kinds of water (i.e., a liquid-water phase and water in the membrane phase) were also developed.[34] In many of the diffusion-type models, transport properties are taken into account using concentrated solution theory. With a three-species system, composed of the membrane, protons, and water, three transport properties are required to describe the system completely.[35]

The goal of this work is to extend this modeling approach to a four-species system, composed of the membrane, two kinds of cations, and water. The model is then applied to an electrolysis cell making syngas ($CO + H_2$) from simultaneous reduction of CO_2 and H_2O that was designed in the laboratory (Chapter 1). The cell architecture involves a membrane in the K^+ form at zero current. When electrolysis proceeds, water oxidation takes place at the anode, releasing protons into the Nafion membrane.

The outline of this chapter is as follows. In the first part, the transport equations are presented for the particular system, and relations developed between macroscopic (measurable) and phenomenological transport properties ($\mathscr{D}_{ij}$ coefficients). From experimental data reported in the literature by Okada et al.,[36] values of the $\mathscr{D}_{ij}$ coefficients are determined. In the second part, a mathematical model is developed, and is used with boundary conditions close those used in the CO_2–H_2O electrolyzer. H^+ and K^+ are the two cations under consideration in this work, but the procedure detailed below can be applied to any other two cations if experimental transport properties are known. The mathematical model has also been used for evaluating the cation contamination of ion-exchange membranes for fuel cells, and is reported elsewhere.[37]

2.2 Multicomponent diffusion equations

As mentioned in the introduction, concentrated solution theory is used for the system under consideration. For an isothermal system composed of two cations, water, and membrane, the extended Stefan-Maxwell equations read[33, 35, 38]

$$c_{H^+}\nabla\mu_{H^+} = \frac{RT}{c_T}\left(\frac{c_{H^+}\mathbf{N}_{H_2O} - c_{H_2O}\mathbf{N}_{H^+}}{\mathscr{D}_{H^+,H_2O}} + \frac{-c_{M^-}\mathbf{N}_{H^+}}{\mathscr{D}_{H^+,M^-}} + \frac{c_{H^+}\mathbf{N}_{K^+} - c_{K^+}\mathbf{N}_{H^+}}{\mathscr{D}_{H^+,K^+}}\right), \tag{2.1}$$

$$c_{K^+}\nabla\mu_{K^+} = \frac{RT}{c_T}\left(\frac{c_{K^+}\mathbf{N}_{H_2O} - c_{H_2O}\mathbf{N}_{K^+}}{\mathscr{D}_{K^+,H_2O}} + \frac{-c_{M^-}\mathbf{N}_{K^+}}{\mathscr{D}_{K^+,M^-}} + \frac{c_{K^+}\mathbf{N}_{H^+} - c_{H^+}\mathbf{N}_{K^+}}{\mathscr{D}_{K^+,H^+}}\right), \tag{2.2}$$

$$c_{H_2O}\nabla\mu_{H_2O} = \frac{RT}{c_T}\left(\frac{c_{H_2O}\mathbf{N}_{H^+} - c_{H^+}\mathbf{N}_{H_2O}}{\mathscr{D}_{H_2O,H^+}} + \frac{-c_{M^-}\mathbf{N}_{H_2O}}{\mathscr{D}_{H_2O,M^-}} + \frac{c_{H_2O}\mathbf{N}_{K^+} - c_{K^+}\mathbf{N}_{H_2O}}{\mathscr{D}_{H_2O,K^+}}\right), \tag{2.3}$$

and,

$$c_{M^-}\nabla\mu_{M^-} - \nabla p = \frac{RT}{c_T}\left(\frac{c_{M^-}\mathbf{N}_{H^+}}{\mathscr{D}_{M^-,H^+}} + \frac{c_{M^-}\mathbf{N}_{K^+}}{\mathscr{D}_{M^-,K^+}} + \frac{c_{M^-}\mathbf{N}_{H_2O}}{\mathscr{D}_{M^-,H_2O}}\right), \tag{2.4}$$

respectively, where $\mathscr{D}_{ij}$ are binary interaction coefficients between species i and j, and c_T is the total volumetric concentration of species, defined as $c_T = c_{H^+} + c_{K^+} + c_{M^-} + c_{H_2O}$. There are several comments about these equations. As there are three components (HM, KM, and H_2O; $n_c = 3$) and four species in the system (H^+, K^+, H_2O, and M^-, with M^- standing for the membrane; $n_s = 4$), any three of these equations are sufficient to define the problem completely. With the Onsager reciprocal relations, $\mathscr{D}_{ij} = \mathscr{D}_{ji}$, there are six independent coefficients that represent the six transport properties of the system, corresponding to a number equal to $n_s(n_s - 1)/2$.[35, 39] Finally, the driving forces have been defined using the same concept as Bennion,[33, 40] where the membrane is considered as a stationary elastic solid that is able to resist forces that tend to deform it. The flux of membrane, $\mathbf{N}_{M^-}$, is set to zero, as is appropriate in a steady state. To express the electrochemical potential of the four species, first define the electric potential in the membrane Φ, either by choosing an arbitrary reference electrode, or by using the concept of the quasi-electrostatic potential.[35] Let us use

a hypothetical hydrogen reference electrode, in which case one has

$$\nabla\mu_{\mathrm{H^+}} = F\nabla\Phi. \tag{2.5}$$

Note that the potential is defined the same way in most of the fuel-cell studies. A problem may arise in this particular system composed of two cations if the proton concentration goes to zero, in which case another definition for the potential would be more convenient. Gradients of electrochemical potentials of the other ionic species are deduced from equation 2.5

$$\nabla\mu_{\mathrm{K^+}} = \nabla\mu_{\mathrm{KM}} - \nabla\mu_{\mathrm{HM}} + F\nabla\Phi \tag{2.6}$$

and

$$\nabla\mu_{\mathrm{M^-}} = \nabla\mu_{\mathrm{HM}} - F\nabla\Phi. \tag{2.7}$$

The chemical potentials of the neutral combinations of ions (HM and KM) and of water, are expressed as

$$\mu_{\mathrm{HM}} = RT\ln(a^{\theta}_{\mathrm{H^+}}a^{\theta}_{\mathrm{M^-}}f_{\mathrm{H^+}}f_{\mathrm{M^-}}x_{\mathrm{H^+}}x_{\mathrm{M^-}}) + \bar{V}_{\mathrm{HM}}(p-p_0), \tag{2.8}$$

$$\mu_{\mathrm{KM}} = RT\ln(a^{\theta}_{\mathrm{K^+}}a^{\theta}_{\mathrm{M^-}}f_{\mathrm{K^+}}f_{\mathrm{M^-}}x_{\mathrm{K^+}}x_{\mathrm{M^-}}) + \bar{V}_{\mathrm{KM}}(p-p_0), \tag{2.9}$$

and

$$\mu_{\mathrm{H_2O}} = RT\ln(a^{0}_{\mathrm{H_2O}}f_{\mathrm{H_2O}}x_{\mathrm{H_2O}}) + \bar{V}_{\mathrm{H_2O}}(p-p_0), \tag{2.10}$$

respectively. a^{θ}_i is the activity of ion i in a secondary reference state, $a^{0}_{\mathrm{H_2O}}$ is the activity of pure water. The mole fraction of species i, x_i, is defined as $x_i = c_i/c_T$.

2.3 Transport-property relations

To establish a mathematical model of the membrane system in terms of the multicomponent diffusion equations, one needs expressions for the binary interaction parameters, $\mathscr{D}_{ij}$'s. These values are not normally measured directly, and thus they need to be related to more com-

mon macroscopic transport properties. According to Newman, for an electrolytic solution $n_s(n_s-1)/2$ of these transport properties characterize interdiffusion of chemical components even in the absence of current.[39] n_c additional transport properties characterize the electrolytic conduction; these are the electrical conductivity κ and n_c-1 independent transference numbers (namely the proton transference number, t_{H^+}, and the water electro-osmotic coefficient, ξ, for the present case).

The formalism reproduced by Newman and Thomas-Alyea[35] can be used to determine the relationships between the macroscopic transport properties and the $\mathscr{D}_{ij}$'s. Let M^- be taken as species 0, which is convenient since $\mathbf{N}_{M^-}$ is taken to be zero (steady state). The three independent driving forces $c_i\nabla\mu_i$ for H^+, K^+, and H_2O are related to the flux densities through M^0_{ij} coefficients

$$c_i\nabla\mu_i = \sum_{j\neq 0} M^0_{ij}\frac{\mathbf{N}_j}{c_j}, \tag{2.11}$$

with $M^0_{ii} = -\sum_{j\neq i} K_{ij}$ and $M^0_{ij} = K_{ij}$ $(j \neq i)$, where K_{ij} is the friction coefficient between species i and j, expressed as

$$K_{ij} = \frac{RTc_ic_j}{c_T\mathscr{D}_{ij}}. \tag{2.12}$$

Equation 2.11 can be inverted so as to relate the flux densities of species i (H^+, K^+, or H_2O) to the driving forces $c_j\nabla\mu_j$ through

$$\mathbf{N}_i = -\sum_{j\neq 0} L^0_{ij}c_ic_j\nabla\mu_j, \tag{2.13}$$

where the matrix $\mathbf{L}^0$ of L_{ij} coefficients is defined as

$$\mathbf{L}^0 = -(\mathbf{M}^0)^{-1}. \tag{2.14}$$

Note that because $\mathbf{M}^0$ is symmetric, the inverse matrix $\mathbf{L}^0$ is also symmetric, and therefore equation 2.13 defines a set of six independent transport parameters that can be used in place of $\mathscr{D}_{ij}$'s. As for the $\mathscr{D}_{ij}$'s, those coefficients cannot be determined directly from the available

experimental measurements, but relationships between macroscopic transport properties and the L_{ij}^0's can be obtained quite simply, as shown in the following.

2.3.1 Conductivity, proton transference number, and water electro-osmotic coefficient

Experiments aimed at measuring the ionic conductivity, κ, proton transference number, $t_{\mathrm{H^+}}$, and water electro-osmotic coefficient, ξ, are carried out in conditions for which there are no concentration (and pressure) gradients; therefore the gradients of electrochemical potential can be simplified to

$$\nabla\mu_{\mathrm{H_2O}} = 0 \text{ and } \nabla\mu_{\mathrm{H^+}} = \nabla\mu_{\mathrm{K^+}} = F\nabla\Phi. \tag{2.15}$$

Those three transport properties can be derived as a function of the L_{ij}^0 coefficients (see Newman and Thomas-Alyea,[35] pp. 308–309), yielding

$$\kappa = F^2(L^0_{\mathrm{H^+,H^+}}{c_{\mathrm{H^+}}}^2 + 2L^0_{\mathrm{H^+,K^+}}c_{\mathrm{H^+}}c_{\mathrm{K^+}} + L^0_{\mathrm{K^+,K^+}}{c_{\mathrm{K^+}}}^2), \tag{2.16}$$

$$t_{\mathrm{H^+}} = \frac{F^2}{\kappa}(L^0_{\mathrm{H^+,H^+}}{c_{\mathrm{H^+}}}^2 + L^0_{\mathrm{H^+,K^+}}c_{\mathrm{H^+}}c_{\mathrm{K^+}}), \tag{2.17}$$

and

$$\xi = \frac{F^2}{\kappa}(L^0_{\mathrm{H^+,H_2O}}c_{\mathrm{H^+}}c_{\mathrm{H_2O}} + L^0_{\mathrm{K^+,H_2O}}c_{\mathrm{K^+}}c_{\mathrm{H_2O}}). \tag{2.18}$$

Note that $t_{\mathrm{K^+}}$ is defined by a similar expression as $t_{\mathrm{H^+}}$, and that those two quantities sum to unity.

2.3.2 Transport parameters characterizing diffusion at zero current

One seeks expressions of the flux densities of H^+, K^+, and H_2O as a function of the chemical potential gradients of the three components (HM, KM, and H_2O) under zero current. With the general notation $\mu_{j,n} = \mu_j - \frac{z_j}{z_n}\mu_n$, where the membrane is taken as species n, equation 2.13 becomes

$$\mathbf{N}_i = -\sum_{j\neq 0} L^0_{ij} c_i c_j \nabla \mu_{j,n} - \frac{t^0_i \kappa}{z_i F^2} \frac{\nabla \mu_n}{z_n}, \tag{2.19}$$

where t^0_i/z_i corresponds to t_{H^+}, t_{K^+}, and ξ for H^+, K^+, and H_2O, respectively. The first term on the right represents multicomponent diffusion, and the last term is a form for migration. $\nabla\mu_n/z_n$ is further expressed as (see Newman and Thomas-Alyea,[35] p. 48),

$$\frac{\nabla \mu_n}{z_n} = -\frac{F}{\kappa}\mathbf{i} - \sum_{j\neq 0} \frac{t^0_j}{z_j} \nabla \mu_{j,n}, \tag{2.20}$$

which is an extended Ohm's law, accounting for the presence of concentration (and pressure) gradients. Substitution into equation 2.19, to introduce the current density, yields

$$\mathbf{N}_i = -\sum_{j\neq 0} \left(L^0_{ij} c_i c_j - \frac{t^0_i t^0_j \kappa}{z_i z_j F^2} \right) \nabla \mu_{j,n} + \frac{t^0_i \mathbf{i}}{z_i F}. \tag{2.21}$$

One can define a transport coefficient $\mathscr{L}^0_{ij}$,

$$\mathscr{L}^0_{ij} = L^0_{ij} c_i c_j - \frac{t^0_i t^0_j \kappa}{z_i z_j F^2}, \tag{2.22}$$

which maintains the symmetry but shows how the coefficient needs to be modified to describe multicomponent diffusion at zero current instead of zero gradient of the electrochemical potential of species n. Additionally, for the present system, it can be shown that $\mathscr{L}^0_{H^+,H^+} = -\mathscr{L}^0_{K^+,K^+} = -\mathscr{L}^0_{H^+,K^+}$ and $\mathscr{L}^0_{H^+,H_2O} = -\mathscr{L}^0_{K^+,H_2O}$, and as a consequence only three of the six $\mathscr{L}^0_{ij}$'s are independent.

The design of orthogonal experiments, as reported by Pintauro and Bennion[41] for a cation-exchange membrane containing a salt such as NaCl should allow for the unequivocal determination of the three transport parameters κ, t_{H^+}, ξ, as well as the three independent $\mathscr{L}_{ij}^0$'s. Unfortunately, such experimental data are not available in the literature for the present system. To our knowledge, there are only a few reports on transport properties of cation-exchange membranes with two different cations.[36, 42–44] The work by Okada et al.[36, 44] is one of the most comprehensive, as four transport parameters, i.e., the conductivity, the proton transference number, the electro-osmotic coefficient, and the water permeability (denoted L_{p,H_2O}), were determined for various ratios of Na^+/H^+, Li^+/H^+, K^+/H^+, $Rb^+/\ H^+$, and Cs^+/H^+ liquid-equilibrated membranes at 25°C.

Since water permeability values are reported, let us relate this parameter to the transport coefficients $\mathscr{L}_{ij}^0$ previously defined. The water permeability L_{p,H_2O} is defined according to[42]

$$\mathbf{J}_v \approx \bar{V}_{H_2O}^{sln} \mathbf{N}_{H_2O} = -L_{p,H_2O} l \nabla p, \tag{2.23}$$

where $\mathbf{J}_v$ is the volume flowrate across the membrane due to a pressure gradient, $\bar{V}_{H_2O}^{sln}$ is the partial molar volume of water in the solution in contact with the membrane during the measurement, and l is the membrane thickness defined by

$$l = l_{dry,H^+form} \left(\frac{1}{\bar{V}_{HM} c_{M^-}} \right)^{1/3}, \tag{2.24}$$

in which it is assumed that membrane swelling is isotropic, for simplicity, and l_{dry,H^+form} is the thickness of a dry membrane in the proton form. Note that equation 2.23 relies on the assumption that the volume flowrate across the membrane is due solely to a water flux; in other words, the contribution of the fluxes of H^+ and K^+ to the volume flowrate has been neglected.[42] Under the conditions of the water permeability measurement,[42] the gradient of chemical potential of water is solely related to the pressure gradient according to $\nabla \mu_{H_2O} = \bar{V}_{H_2O}^{m} \nabla p$, and, assuming that the chemical potential gradient of water is the main driving force for water flux across the membrane,[42] the relation between the water

permeability and the $\mathscr{L}^0_{ij}$'s reads

$$L_{p,\mathrm{H_2O}} = \mathscr{L}^0_{\mathrm{H_2O},\mathrm{H_2O}} \frac{\bar{V}^{\mathrm{sln}}_{\mathrm{H_2O}} \bar{V}^{\mathrm{m}}_{\mathrm{H_2O}}}{l}. \tag{2.25}$$

As a remark, $\mathscr{L}^0_{\mathrm{H_2O},\mathrm{H_2O}}$ corresponds to the water transport coefficient α defined previously in the literature for a membrane with a single cation.[33, 45]

2.4 Determination of binary interaction parameters

In the previous section, macroscopic transport parameters have been expressed in terms of the binary interaction coefficients L^0_{ij}, and therefore can be directly related to the $\mathscr{D}_{ij}$'s as well. Expressions are not presented here for sake of simplicity. The goal of this section is to determine the values of the $\mathscr{D}_{ij}$'s from the experimental values of transport parameters tabulated in the literature.[36] Since values for only four transport parameters out of six are provided, unequivocal values of $\mathscr{D}_{ij}$'s cannot be obtained. Different approaches are thus attempted to overcome this problem. To begin, $\mathscr{D}^\dagger_{\mathrm{C^+},\mathrm{H_2O}}$, $\mathscr{D}^\dagger_{\mathrm{C^+},\mathrm{M^-}}$, and $(\mathscr{D}^\dagger_{\mathrm{H_2O},\mathrm{M^-}})_{\mathrm{C}}$ are determined from three transport parameters (the ionic conductivity, the electro-osmotic coefficient, and the water permeability) of a membrane containing a single cation $\mathrm{C^+}$ ($\mathrm{C^+}$ standing either for $\mathrm{H^+}$ or $\mathrm{K^+}$). The superscript † in $\mathscr{D}^\dagger_{ij}$ means that the values are determined for a membrane with a single cation $\mathrm{C^+}$. The formulation detailed previously in the literature[33] is used and recalled in the appendix 2.8.2. The values of the three transport parameters and the as-obtained $\mathscr{D}^\dagger_{ij}$ are given in Table 2.1. Unequivocal values are obtained since such a system is composed of three species ($\mathrm{C^+}$, $\mathrm{H_2O}$ and $\mathrm{M^-}$) and therefore is entirely defined by three independent transport parameters.

To determine the parameters for the system of interest, a first approach is to consider the binary interaction parameters to be independent of the fraction of protons in the

Table 2.1: Values of conductivity, electro-osmotic coefficient, and water permeability in ion-exchange membranes either in H^+ form or in K^+ form (by Okada et al.[36]), and values of $\mathscr{D}^{\dagger}_{ij}$ calculated from those three measured transport properties, at $T = 25^{o}$C and $p = 1$ atm.

	K-form	H-form
κ (S/m)	4.57	20.0
ξ	4.82	2.93
α (mol^2/J m s)	4.17 10^{-8}	2.02 10^{-7}
$\mathscr{D}^{\dagger}_{C^+,H_2O}$ (m^2/s)	1.07 10^{-9}	6.60 10^{-9}
$\mathscr{D}^{\dagger}_{C^+,M^-}$ (m^2/s)	1.15 10^{-10}	5.02 10^{-10}
$(\mathscr{D}^{\dagger}_{H_2O,M^-})_C$ (m^2/s)	6.25 10^{-10}	1.05 10^{-9}

membrane y_{HM}, expressed as

$$y_{HM} = \frac{c_{H^+}}{c_{H^+} + c_{K^+}} = \frac{c_{H^+}}{c_{M^-}}. \tag{2.26}$$

However, as two extreme values of $\mathscr{D}^{\dagger}_{H_2O,M^-}$ are obtained (namely $(\mathscr{D}^{\dagger}_{H_2O,M^-})_H$ and $(\mathscr{D}^{\dagger}_{H_2O,M^-})_K$), $\mathscr{D}_{H_2O,M^-}$ cannot be taken as a constant. Thus, $\ln(\mathscr{D}_{H_2O,M^-})$ is linearly interpolated as a function of y_{rmHM} between the two extreme values according to

$$D_{ij} = D^{\dagger}_{ij} \exp\left(m_{ij}(y_{HM} - y^{\dagger}_{HM})\right), \tag{2.27}$$

where $y^{\dagger}_{HM}$ is either equal to 0 or 1 whether $\mathscr{D}^{\dagger}_{ij}$ refers to the membrane in K^+ or H^+ form, respectively. The m_{ij} coefficient is expressed as $m_{H_2O,M^-} = \ln\left(\mathscr{D}^{\dagger}_{H_2O,M^-}\right)_H - \ln\left(\mathscr{D}^{\dagger}_{H_2O,M^-}\right)_K$, and the value is reported in Table 2.2.

Note that the choice of this type of interpolation is arbitrary, as further discussed in the following. Based on this first approach, the values of the four transport properties can be calculated as a function of y_{HM} and compared with the experimental ones (Figure 2.1). As the value of $\mathscr{D}_{H^+,K^+}$ is unknown, different values were attempted. It appears that the largest ($\mathscr{D}_{H^+,K^+} = 1\ 10^6$ m^2/s) value leads to a smaller difference between the experimental and the calculated curves, which means that the interactions between K^+ and H^+ can be

Table 2.2: Values of coefficients m_{ij}, corresponding to the slope of $\ln(\mathscr{D}_{ij}) = f(y_{\mathrm{HM}})$ (see equation 2.27).

	H^+, H_2O	H^+, M^-	K^+, H_2O	K^+, M^-	H_2O, M^-
m_{ij}	0.26	-2.0	5.0	-2.3	0.51

$m_{\mathrm{H_2O,M^-}}$ is expressed as $m_{\mathrm{H_2O,M^-}} = \ln\left(\mathscr{D}^{\dagger}_{\mathrm{H_2O,M^-}}\right)_{\mathrm{H}} - \ln\left(\mathscr{D}^{\dagger}_{\mathrm{H_2O,M^-}}\right)_{\mathrm{K}}$. No m_{ij} is defined for H^+,K^+ since $\mathscr{D}_{\mathrm{H^+,K^+}}$ is set to a very high constant value. Values of m_{ij}'s for the four remaining $\mathscr{D}_{ij}$'s were refined by a least-square nonlinear regression of the four measured transport properties shown in figure 2.2.

neglected. $\mathscr{D}_{\mathrm{H^+,K^+}}$ is thus set to this large arbitrary value in the remainder of this work. However, even with a very high value of $\mathscr{D}_{\mathrm{H^+,K^+}}$, the calculated transport parameters are not in good agreement with the experimental data, meaning that there is an actual dependence of the $\mathscr{D}_{ij}$'s with y_{HM}.

To account for such a dependence, a second approach is undertaken where the $\mathscr{D}_{ij}$ values are adjusted using a least-square nonlinear regression method of the four transport parameters. Just like the interpolation of $\mathscr{D}_{\mathrm{H_2O,M^-}}$, a linear variation of $\ln(\mathscr{D}_{ij})$ as a function of y_{HM} is chosen (equation 2.27). $y^{\dagger}_{\mathrm{HM}}$ is equal to 1 for $\mathscr{D}_{\mathrm{H^+,H_2O}}$ and $\mathscr{D}_{\mathrm{H^+,M^-}}$, and to 0 for $\mathscr{D}_{\mathrm{K^+,H_2O}}$ and $\mathscr{D}_{\mathrm{K^+,M^-}}$. Values of m_{ij} coefficients obtained from the refinement of the four experimental transport properties are given in Table 2.2; the values of transport properties calculated from equation 2.27 using the refined values are overlaid to the experimental data in Figure 2.2; and the values of the $\mathscr{D}_{ij}$'s are represented as a function of y_{HM} in Figure 2.3.

As observed in Figure 2.2, the calculated values of the four transport properties are in good agreement with the experimental ones. However, this does not necessarily support a linear dependence of $\ln(\mathscr{D}_{ij})$ as a function of y_{HM}. Indeed, other functions $\mathscr{D}_{ij} = f(y_{\mathrm{HM}})$ have been tried, and lead to satisfactory adjustments of the experimental transport properties as well. Of course, in this case, the values of $\mathscr{D}_{ij}$ are different from those obtained by the linear interpolation of $\ln(\mathscr{D}_{ij})$ as a function of y_{HM}, although the trends of variation of $\mathscr{D}_{ij}$ with y_{HM} are similar. This demonstrates that although the $\mathscr{D}_{ij}$ values in Figure 2.3 do not have to be considered as very accurate, they provide information on how the $\mathscr{D}_{ij}$'s vary with y_{HM}.

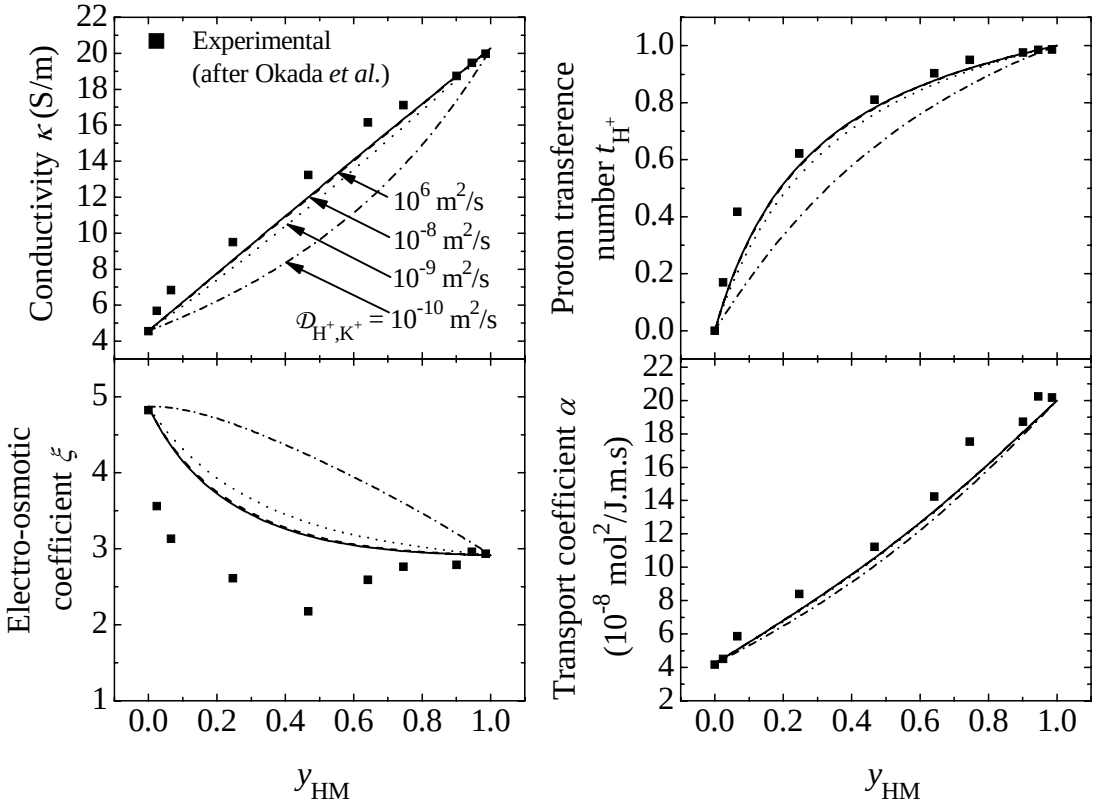

Figure 2.1: Comparisons of the four measured transport properties (data by Okada et al.[36]) and their calculated values obtained by assuming $\mathscr{D}_{H^+,H_2O}$, $\mathscr{D}_{H^+,M^-}$, $\mathscr{D}_{K^+,H_2O}$, and $\mathscr{D}_{K^+,M^-}$ to be independent of y_{HM}. Those values were determined for membranes either in the H^+ form or in the K^+ form. ($\mathscr{D}_{H_2O,M^-}$ was interpolated between the values obtained for each form.) Several values of $\mathscr{D}_{H^+,K^+}$ were attempted.

If one obtains more experimental data points with very little error, a more general form of $\ln(\mathscr{D}_{ij}) = f(y_{HM})$, such as a polynomial, could be used, although there is a trade-off between the robustness of the fit and the number of parameters to refine.

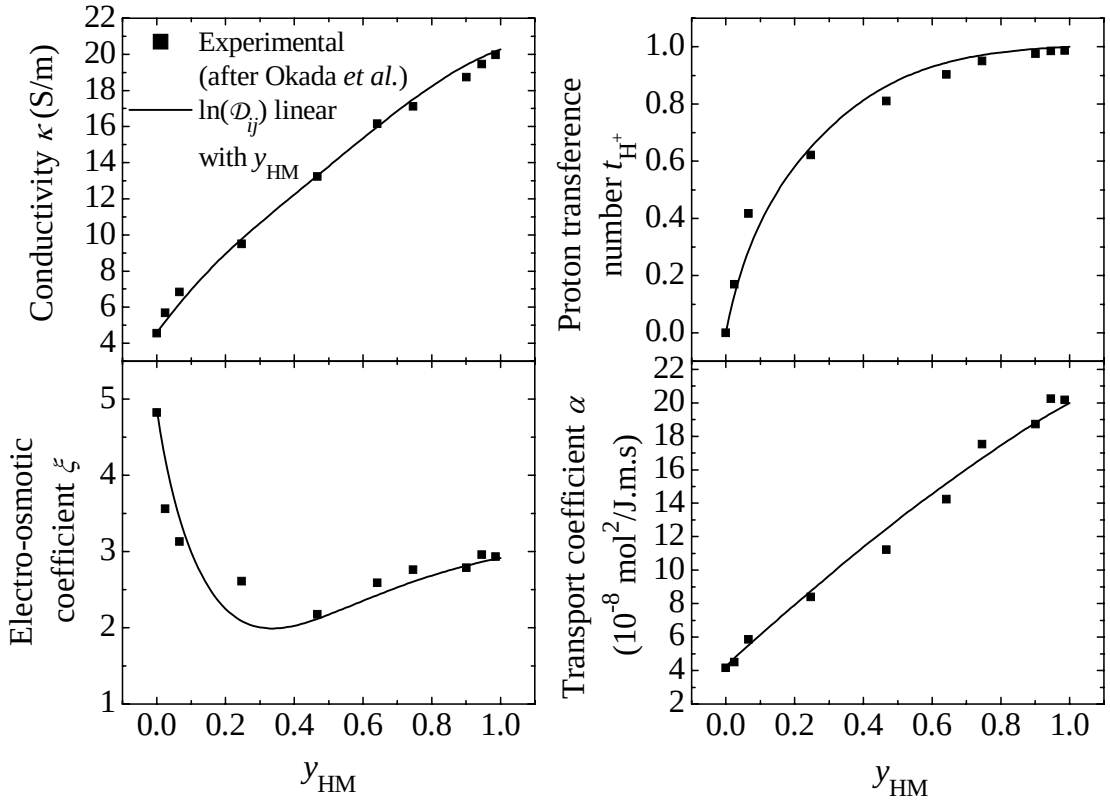

Figure 2.2: Comparisons of the four measured transport properties (data by Okada et al.[36]) and calculated values for which a linear variation of $\ln(\mathscr{D}_{ij})$ with y_{HM} is assumed for $\mathscr{D}_{\mathrm{H^+,H_2O}}$, $\mathscr{D}_{\mathrm{H^+,M^-}}$, $\mathscr{D}_{\mathrm{K^+,H_2O}}$, and $\mathscr{D}_{\mathrm{K^+,M^-}}$. The slopes of those variations were adjusted using a least-square nonlinear regression method to obtain the best fits. $\mathscr{D}_{\mathrm{H_2O,M^-}}$ is interpolated between the values obtained from the membranes in either H^+ or K^+ form.

2.5 Mathematical model of an ion-exchange membrane with two cations

As mentioned in the introduction, one of the goals of this work is to develop an isothermal, steady-state, 1-D mathematical model of the ion-exchange membrane with two cations (H^+ and K^+). This is a boundary-type problem. The governing equations considered for the model are given below, along with some possible boundary conditions.

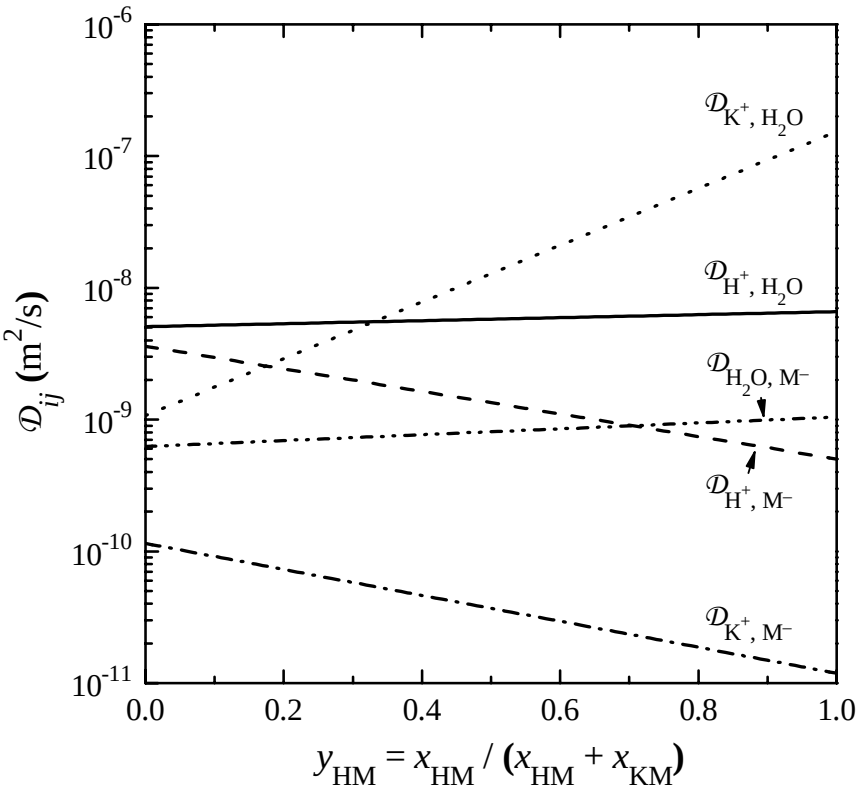

Figure 2.3: Binary interaction parameters $\mathscr{D}_{ij}$ determined from a least-square nonlinear regression method of the four experimental transport properties shown in figure 2.2. $\mathscr{D}_{H^+,K^+}$ is not shown; it was taken to be 10^6 m^2/s.

2.5.1 Governing equations

There are eight unknowns in the present system: the particle fractions, x_{H^+}, x_{K^+}, x_{H_2O}, x_{M^-}, the flux densities along x, N_{H^+}, N_{K^+}, N_{H_2O}, and the electric potential, Φ. Note that $N_{M^-} = 0$ since steady processes are considered; therefore it is not considered an unknown. Eight equations are thus required, among which three diffusion equations out of four are chosen (one is dependent), for instance equations 2.1, 2.2, and 2.4. Because the membrane is stationary at steady state and it is assumed to be at uniform stress, the term $\partial p/\partial x$ in equation 2.4 is set equal to zero. Expressions for the gradients of electrochemical potential of K^+ and M^- are derived from equations 2.6 and 2.7, respectively, by substituting the gradients of chemical potential of HM and KM by the right hand side terms of equations 2.8

and 2.9, respectively. This reads

$$\nabla\mu_{\mathrm{K}^+} = RT\left(\frac{\nabla x_{\mathrm{K}^+}}{x_{\mathrm{K}^+}} - \frac{\nabla x_{\mathrm{H}^+}}{x_{\mathrm{H}^+}}\right) + b\left(\nabla\left({y_{\mathrm{HM}}}^2\right) - \nabla\left({y_{\mathrm{KM}}}^2\right)\right) + F\nabla\Phi \tag{2.28}$$

and

$$\nabla\mu_{\mathrm{M}^-} = RT\left(\frac{\nabla x_{\mathrm{H}^+}}{x_{\mathrm{H}^+}} + \frac{\nabla x_{\mathrm{M}^-}}{x_{\mathrm{M}^-}}\right) + b\nabla\left({y_{\mathrm{KM}}}^2\right) - F\nabla\Phi. \tag{2.29}$$

The terms $\frac{\partial(\bar{V}_i(p-p^0))}{\partial x}$ have been set to zero since these effects are minor and any pressure driven flow is accounted for by the use and coupling of the water transport coefficient. As it was shown that such an ion-exchange membrane behaves as a regular mixture of HM and KM, activity coefficients are expressed as[46]

$$f_{\mathrm{KM}} = f_{\mathrm{K}^+}f_{\mathrm{M}^-} = \exp(\frac{b}{RT}{y_{\mathrm{HM}}}^2) \text{ and } f_{\mathrm{HM}} = f_{\mathrm{H}^+}f_{\mathrm{M}^-} = \exp(\frac{b}{RT}{y_{\mathrm{KM}}}^2), \tag{2.30}$$

where b is a constant taken equal to -151 J/mol.[36] As there are three unknown flux densities, one needs three material balances of the form

$$\frac{\partial N_i}{\partial x} = 0, \tag{2.31}$$

with $i = \mathrm{H}^+$, K^+, and $\mathrm{H_2O}$. (The material balance for M^- was already used in setting $N_{\mathrm{M}^-} = 0$.) The two remaining equations are the sum of the mole fractions,

$$x_{\mathrm{H}^+} + x_{\mathrm{K}^+} + x_{\mathrm{H_2O}} + x_{\mathrm{M}^-} = 1, \tag{2.32}$$

and electroneutrality

$$x_{\mathrm{H}^+} + x_{\mathrm{K}^+} = x_{\mathrm{M}^-}. \tag{2.33}$$

The membrane thickness generally varies with the water content in the membrane, and therefore it has to be considered as an additional unknown of the system, which is carried

across the membrane (scalar invariant) using the equation[47]

$$\frac{\partial l}{\partial x} = 0. \tag{2.34}$$

Another variable, namely, the total number of moles of membrane M^- per cross sectional area (denoted η), is then required and is related to the local membrane concentration c_{M^-} through[47]

$$\frac{\partial \eta}{\partial x} = c_{M^-}. \tag{2.35}$$

2.5.2 Boundary conditions

If the membrane is in contact with a solution in which concentrations of H^+ and K^+ are defined, an ion-exchange reaction between the membrane and the solution occurs at the interface according to

$$H^+_{sln} + KM \rightleftharpoons K^+_{sln} + HM. \tag{2.36}$$

As a first approximation, the rate of this reaction can be assumed fast enough to consider it to be equilibrated, and equilibrium relationship holds at the boundary under consideration

$$\Delta r G^0_{T,P} = -RT \ln \frac{f_{HM} y_{HM} c_{K^+,sln}}{f_{KM} y_{KM} c_{H^+,sln}}, \tag{2.37}$$

where $\Delta r G^0_{T,P}$ is the Gibbs energy of the reaction ($\Delta r G^0_{T,P} = -669.3$ J/mol),[36] y_{KM} is defined with a similar relationship as relation 2.26, and f_{HM} and f_{KM} are the activity coefficients of HM and KM components, defined by equation 2.30. In this equilibrium relationship, activity coefficients of HA and KA (with counterion A in the aqueous solution in contact with the membrane) have been approximated to unity, which supposes that the solution of H^+ and K^+ is dilute.

Another possible boundary condition is the equilibrium relationship between H_2O in the membrane and liquid H_2O in contact with the membrane (as for the ion-exchange reaction,

it is assumed that this is equilibrated). For pure water or a dilute solution (thus assuming that water activity is close to unity), an empirical polynomial relationship between the water content in the membrane λ and the fraction of protons y_{HM} was deduced from the experimental data reported by Okada et al.[36]

$$\lambda = \frac{x_{\mathrm{H_2O}}}{x_{\mathrm{M^-}}} = -3.9578{y_{\mathrm{HM}}}^4 + 8.5846{y_{\mathrm{HM}}}^3 - 10.087{y_{\mathrm{HM}}}^2 + 13.526y_{\mathrm{HM}} + 13.227. \tag{2.38}$$

If the membrane thickness l and total number of moles of membrane $\mathrm{M^-}$ per cross sectional η are solved for, two boundary conditions are required for equations 2.34 and 2.35: η is set to zero at one side of the membrane, and, at the other side, it is related to the membrane thickness using the relationship

$$\eta \approx \frac{{l_{\mathrm{dry,H^+form}}}^3}{\bar{V}_{\mathrm{HM}} l^2}, \tag{2.39}$$

where an isotropic expansion/contraction of the membrane has been assumed..

Finally, other boundary conditions include an arbitrary reference potential, and values for the flux densities, which can be set to a known value or expression such as Faraday's law,

$$N_i = \frac{s_i i}{nF} \tag{2.40}$$

or a zero flux if one of the ions cannot leave the membrane on a given side.

2.6 Application to a CO_2 and H_2O electrolysis cell

The main purpose of this work is to optimize the electrolysis cell (making syngas by simultaneous reduction of CO_2 and H_2O) that was developed in our laboratory and described in chapter 1 by means of a mathematical model. The detailed mathematical model and simulations of the overall cell operation are presented in chapter 4. The cell is composed of a Nafion membrane with an aqueous solution of K^+ (and H^+) on one side and an electrode

evolving oxygen at the other side. Protons are released at the anode side as the oxygen evolution reaction (OER) proceeds and flow across the Nafion toward the aqueous solution. Meanwhile, water is transported in the same direction because of the electro-osmotic flux. We are interested in a mathematical model of the present membrane so as to know how much water is transported per proton, how much the ohmic drop across the membrane is, and how much the membrane swells when the current density is varied.

To answer the above questions, one needs to solve for ten variables, using the governing equations and boundary conditions described above, including equilibrium relationships 2.37 and 2.38 on the cathode side and equilibrium relationship 2.38 on the anode along with a zero-flux condition on K^+ and the flux of protons defined by Faraday's law (eq. 2.40). The system of equations is solved using the subroutine BAND(j),[35] based on a finite-difference method, with 25 mesh points. The thickness of the dry membrane in the proton form is set to $l_{\mathrm{dry,H^+form}} = 178$ μm (Nafion 117), and concentrations of H^+ and K^+ in the aqueous solution are chosen to be 0.1 mol/L. Note that those concentrations do not reflect the actual concentration in the electrolysis, for which the concentration of H^+ is much lower (pH is slightly basic).

The profiles of y_{HM} and λ within the membrane are shown in Figure 2.4 for several values of current density. As expected, while y_{HM} and λ remain constant whatever the current density at the interface between the aqueous solution and the membrane ($x = 0$) (equilibria 2.37 and 2.38 are assumed), values of y_{HM} and λ increase with current density at the anode side of the membrane because protons are released by the OER. It is noteworthy that this side of the membrane is mostly converted to proton-form for a current density of 1 A/cm^2. Figure 2.5 presents the variation of four parameters as a function of the current density, namely, the average proton fraction in the membrane, the membrane thickness l, the electric potential of the membrane at the anode side Φ_{anode}, and β, defined as the ratio of the flux of water over the flux of charge carriers (solely the protons in this case).[48] When increasing the current density, the average proton fraction increases from ca. 0.2 to 0.8 and decreases from

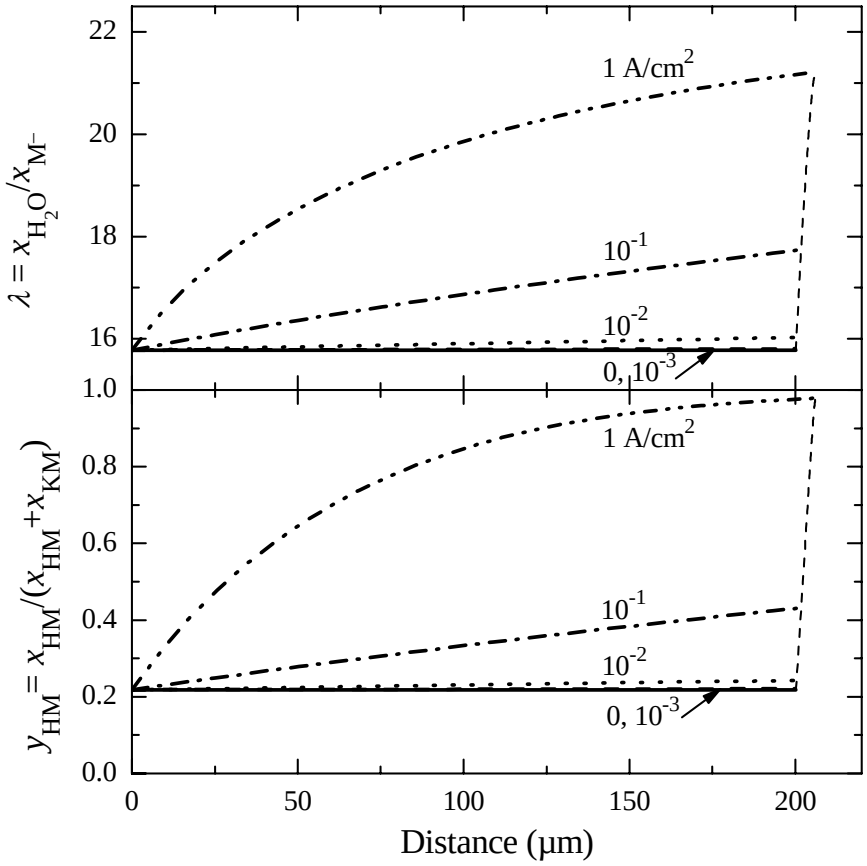

Figure 2.4: Calculated profiles of y_{HM} and λ for various current densities in an ion-exchange membrane used in a CO_2–H_2O electrolyzer. The oxygen anode is on the right, and a flux of protons and water is flowing towards the aqueous solution containing 0.1 mol/L of H^+ and 0.1 mol/L of K^+, which is located on the left boundary. The dry thickness of the membrane in H^+ form is 178 μm (Nafion 117).

ca. 3.5 to 3.05. The membrane potential at the anode side is not linear with the current density, which points out a deviation from a pure ohmic-type behavior of the membrane. In fact, the variation of this potential depends on the way it is defined. For instance, if M^- is taken as the reference species to define the potential, the variation of this latter with the current density is more linear. Finally, one notes that the membrane thickness slightly increases as a function of the current density, as expected by the increase of the average water content. Those simulations provide guidelines for the design and optimization of the electrochemical cell. For instance, they tell us that the net flux of water from the anode

to the aqueous solution will lead to a dilution of this latter solution, thereby decreasing its conductivity with time.

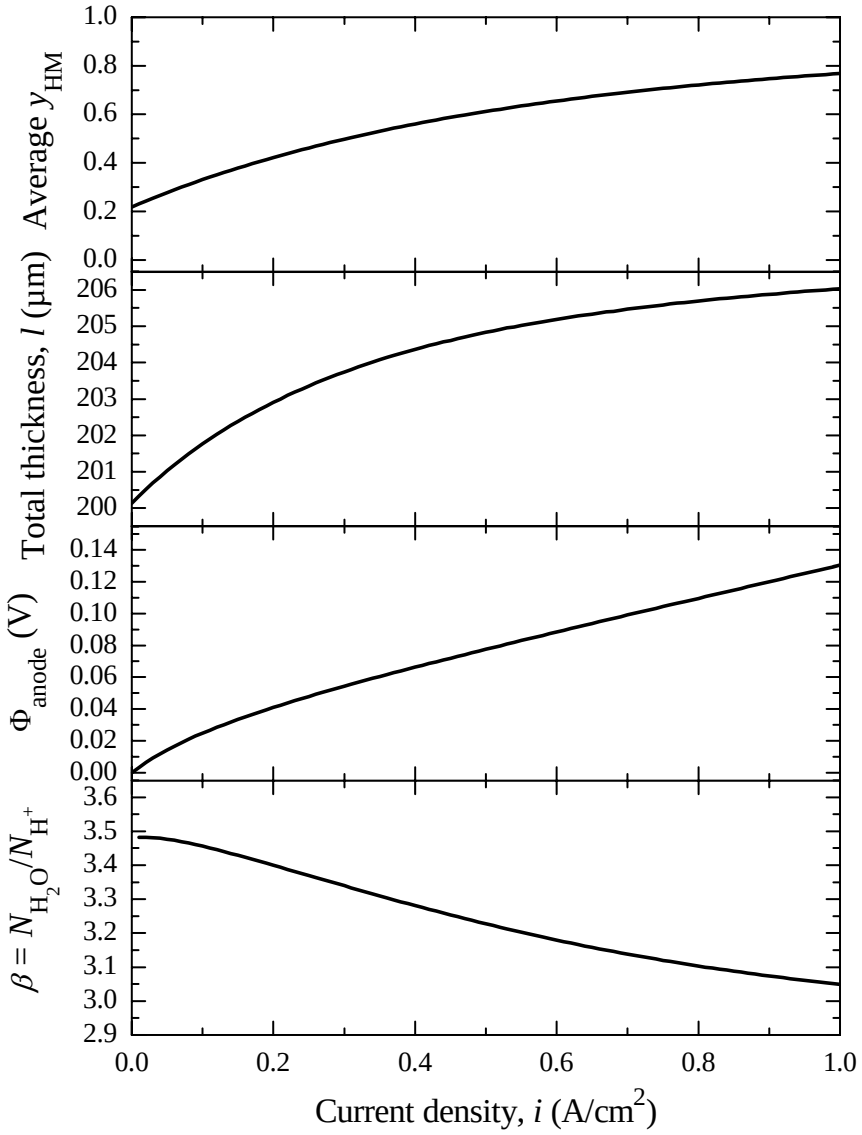

Figure 2.5: Membrane thickness, anode potential, and net water flux per cation flux as a function of the current density in an ion-exchange membrane used in a CO_2–H_2O electrolyzer. The oxygen anode is on the right, and a flux of protons and water is flowing towards the aqueous solution containing 0.1 mol/L of H^+ and 0.1 mol/L of K^+, which is located on the left boundary. The dry thickness of the membrane in H^+ form is 178 μm (Nafion 117).

2.7 Conclusion

Concentrated solution theory, based on the extended Stefan-Maxwell multicomponent transport equations, was successfully applied to describe transport phenomena in an ion-exchange membrane containing two cations, namely, H^+ and K^+. Macroscopic transport properties, i.e., conductivity, H^+ transference number, water electro-osmotic coefficient, and transport parameters characterizing diffusion at zero current, were expressed as functions of the binary interaction parameters, $\mathscr{D}_{ij}$, used in the multicomponent transport equations. As data for only four transport properties are available experimentally, the six $\mathscr{D}_{ij}$'s could not be determined in an unequivocal manner. When $\mathscr{D}_{H^+,H_2O}$, $\mathscr{D}_{H^+,M^-}$, $\mathscr{D}_{K^+,H_2O}$, and $\mathscr{D}_{K^+,M^-}$ were taken to be independent of y_{HM} and equal to values calculated for a membrane with a single cation ($\mathscr{D}_{H_2O,M^-}$ is interpolated between the two extreme values obtained), it was shown that there is no interaction between H^+ and K^+, corresponding to very high values of $\mathscr{D}_{H^+,K^+}$. The next step was to consider a variation of the binary diffusion coefficients with the membrane composition, so as to ensure a better agreement with the four experimental transport properties and the calculated ones for intermediate values of y_{HM}. Linear variations of $\ln(\mathscr{D}_{ij})$ with y_{HM} were assumed, and values of the $\mathscr{D}_{ij}$'s were refined using a nonlinear least-square regression technique for $0 < y_{HM} < 1$. In the second part of this work, a generic mathematical model of the transport phenomena in the membrane was developed, and specific boundary conditions were provided for the case of a membrane used in an electrolysis cell for simultaneous CO_2 and H_2O reduction. The model was used to predict the membrane behavior as a function of the current density, e.g., swelling effects, the ohmic drop, and the net water flux per charge-carrier flux.

2.8 Appendices

2.8.1 Volumetric concentrations and partial molar volumes

The volumetric concentration of species i ($i = H^+$, K^+, H_2O, or M^-) is expressed as

$$c_i = \frac{x_i}{x_{H^+}\bar{V}_{HM} + x_{K^+}\bar{V}_{KM} + x_{H_2O}\bar{V}^{m}_{H_2O}}, \tag{2.41}$$

where $\bar{V}_i$ stands for the partial molar volume of component i. Partial molar volumes $\bar{V}_i$ are normally composition-dependent, but for sake of simplicity, they were considered to be constant, and values were refined by least square nonlinear regression on the membrane density ρ and the water volume fraction θ, expressed as

$$\rho = \frac{x_{H^+}M_{HM} + x_{K^+}M_{KM} + x_{H_2O}M_{H_2O}}{x_{H^+}\bar{V}_{HM} + x_{K^+}\bar{V}_{KM} + x_{H_2O}\bar{V}^{m}_{H_2O}} \tag{2.42}$$

and

$$\theta = \frac{x_{H_2O}\bar{V}^{m}_{H_2O}}{x_{H^+}\bar{V}_{HM} + x_{K^+}\bar{V}_{KM} + x_{H_2O}\bar{V}^{m}_{H_2O}}, \tag{2.43}$$

respectively. The values are reported in table 2.3, and experimental values for density and water volume fraction and the results of the fits are given in figure 2.6.

Table 2.3: Values of partial molar volumes from regression of density and water volume fraction data taken from Okada et al.[36]. The result of the fits is provided in figure 2.6.

	HM	KM	H_2O
$\bar{V}_i$ (cm^3/mol)	566	542	16.3
M_i (g/mol)	1100	1138	18.0

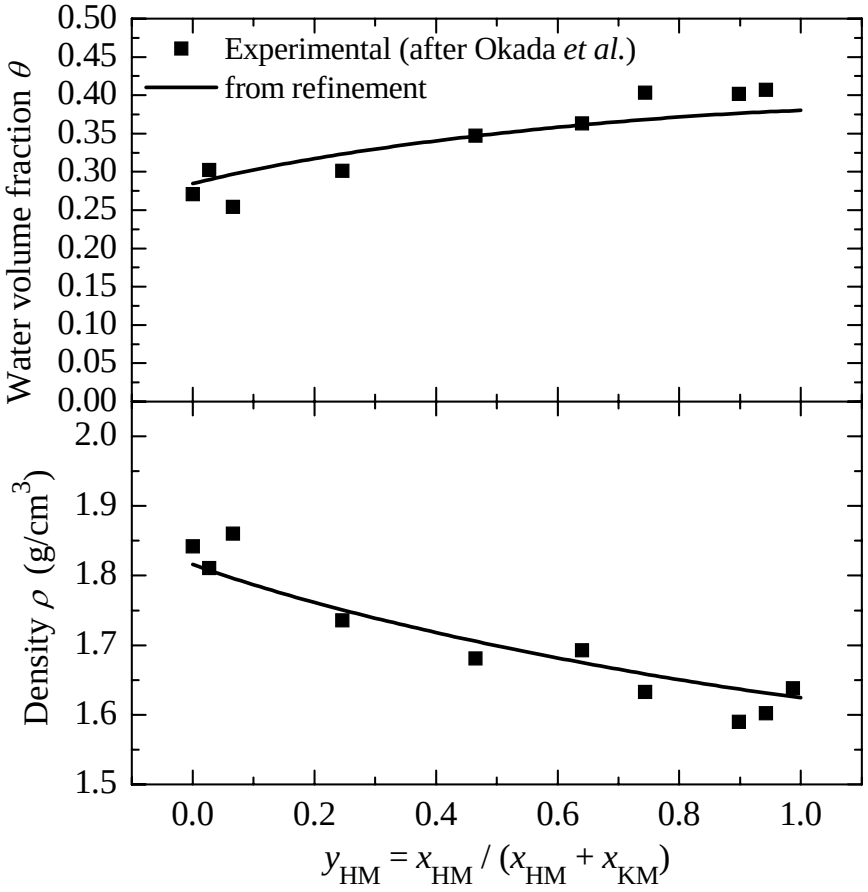

Figure 2.6: Experimental data from Okada et al.[36] and results of the fits for membrane density and water volume fraction as a function of the membrane proton fraction.

2.8.2 Binary diffusion coefficients of ion-exchange membranes with a single cation

The relationships between the three binary diffusion coefficients and the three transport properties, namely, the conductivity, κ, the electro-osmotic coefficient, ξ, and the water transport coefficient, α, were derived by Fuller for a three-species membrane (C^+, H_2O, and M^-).[33] Coefficients $L_{ij}^{0,\dagger}$ are expressed by

$$L_{C^+,C^+}^{0,\dagger} = \frac{\kappa}{F^2 {c_{C^+}}^2},\ L_{H_2O,H_2O}^{0,\dagger} = \frac{1}{{c_{H_2O}}^2}\left(\alpha + \frac{\kappa\xi^2}{F^2}\right),\ \text{and}\ L_{C^+,H_2O}^{0,\dagger} = \frac{\kappa\xi}{F^2 c_{C^+} c_{H_2O}}. \qquad (2.44)$$

The frictional coefficients $K^{\dagger}_{ij}$ are then expressed as a function of $L^{0,\dagger}_{ij}$

$$K^{\dagger}_{\mathrm{C^+,H_2O}} = \frac{L^{0,\dagger}_{\mathrm{C^+,H_2O}}}{L^{0,\dagger}_{\mathrm{H_2O,H_2O}} L^{0,\dagger}_{\mathrm{C^+,C^+}} - {L^{0,\dagger}_{\mathrm{C^+,H_2O}}}^2},\ K^{\dagger}_{\mathrm{C^+,M^-}} = \frac{L^{0,\dagger}_{\mathrm{H_2O,H_2O}} - L^{0,\dagger}_{\mathrm{C^+,H_2O}}}{L^{0,\dagger}_{\mathrm{H_2O,H_2O}} L^{0,\dagger}_{\mathrm{C^+,C^+}} - {L^{0,\dagger}_{\mathrm{C^+,H_2O}}}^2},$$
$$\text{and } K^{\dagger}_{\mathrm{M^-,H_2O}} = \frac{L^{0,\dagger}_{\mathrm{C^+,C^+}} - L^{0,\dagger}_{\mathrm{C^+,H_2O}}}{L^{0,\dagger}_{\mathrm{H_2O,H_2O}} L^{0,\dagger}_{\mathrm{C^+,C^+}} - {L^{0,\dagger}_{\mathrm{C^+,H_2O}}}^2} \tag{2.45}$$

and $\mathscr{D}^{\dagger}_{ij}$ coefficients are deduced from the frictional coefficients using equation 2.12.

List of Symbols

a_i	activity of species or component i
b	constant used in the expression of the activity coefficient of a regular solution, J/mol
c_i	volumetric concentration, mol/m^3
c_T	total volumetric concentration of species, mol/m^3
$\mathscr{D}_{ij}$	diffusion coefficient for interaction between species i and j, m^2/s
f_i	activity coefficient of species or component i
F	Faraday's constant, 96,487 C/mol
$\mathbf{i}$	current density, A/m^2
$\mathbf{J}_v$	volume flowrate across the membrane per surface area of membrane, m/s
K_{ij}	friction coefficient for interaction between species i and j, J s/m^5
l	membrane thickness, m
$l_{\mathrm{dry,H^+form}}$	membrane thickness of a dry membrane in the H^+ form, m
L^0_{ij}	inverted transport coefficient for species, m5/J s
$\mathscr{L}^0_{ij}$	transport parameter that characterizes diffusion at zero current, mol^2/J m s

$L_{p,\mathrm{H_2O}}$ water permeability coefficient, $\mathrm{m^4/J\ s}$

m_{ij} slope of $\ln(\mathscr{D}_{ij}) = f(y_{\mathrm{HM}})$

M_i molar mass of component i, g/mol

K^0_{ij} modified friction coefficient between species i and j, $\mathrm{J\ s/m^5}$

n number of electrons transferred in electrode reaction

n_c number of components

n_s number of species

$\mathbf{N}_i$ flux density of species i, $\mathrm{mol/m^2\ s}$

p pressure, Pa

p_0 reference pressure, Pa

R universal gas constant, 8.3143 J/mol K

s_i stoichiometric coefficient of species i in electrode reaction

t^0_i transference number of species i, with respect to the velocity of species 0

$t_{\mathrm{H^+}}$ transference number of protons in the membrane

T absolute temperature, K

$\bar{V}_i$ partial molar volume of component i, $\mathrm{m^3/mol}$

x distance in the membrane from the interface between the membrane and the aqueous solution, m

x_i mole fraction of species i

y_{CM} number of moles of cations $\mathrm{C^+}$ ($\mathrm{H^+}$ or $\mathrm{K^+}$) over the total number of moles of cations in the membrane

α Water transport coefficient in the membrane, equal to $\mathscr{L}^0_{\mathrm{H_2O,H_2O}}$, $\mathrm{mol^2/J\ m\ s}$

β net water flux per cation flux in the membrane

$\Delta rG^0_{T,P}$ Gibbs energy change of the ion-exchange reaction, J/mol

Φ electric potential, V

η	number of moles of membrane per surface area of membrane, mol/m^2
κ	membrane conductivity, S/m
λ	number of moles of water per mole of membrane
μ_i	(electro)chemical potential of species or component i, J/mol
$\mu_{i,n}$	chemical potential of the neutral combination of species i and n, J/mol
θ	water volume fraction in the membrane
ρ	density of the membrane, g/m^3
ξ	water electro-osmotic coefficient

superscript

0	reference state related to a pure component
m	variable referred to the membrane
sln	variable defined in the aqueous solution next to the membrane
θ	secondary reference state
†	membrane with a single cation

subscript

anode	variable defined at the membrane/anode interface
C	diffusion coefficient calculated from a membrane in the C^+ form (with C^+ = H^+ or K^+)

Chapter 3

Mathematical modeling of the kinetics of CO_2 and H_2O reduction on planar silver and gold electrodes

3.1 Introduction

Because of the greenhouse effect due to CO_2 build-up in the atmosphere, there has been much interest in developing renewable energy sources that are CO_2 neutral. Renewable energy can be chemically stored into various forms, including methanol, which is a convenient form because it is pretty straightforward to handle and store, as compared for instance with hydrogen.[49] When methanol is used as a fuel, it generates CO_2 that needs to be captured and converted back to methanol in order for the overall process to be CO_2 neutral. An intermediate step of this conversion generally involves the formation of syngas (i.e., a mixture of CO and H_2), which can interestingly be produced in a single step using direct CO_2/H_2O electrolysis at room temperature. Although electrochemical reduction of CO_2 to CO has been studied extensively, most of the studies have been focused on the cathode only and only a

few of them have aimed at designing an energy-efficient complete system.[25,50] In chapter 1, the design of such a system is discussed in detail. We compare different experimental setups involving a silver-based gas-diffusion cathode for CO_2 and H_2O reduction to CO and H_2, respectively, together with a Pt–Ir-based anode oxidizing water into oxygen. A next step of our work is to develop a mathematical model in order to understand the limitations of the electrolysis cell and improve its design further.

In this chapter, preliminary to the modeling of the complete system, we focus on the kinetics of CO_2 and H_2O reduction, which is studied using data obtained on planar silver and gold electrodes either from the literature or from a home-made electrochemical cell. Because those two electrochemical reactions are coupled with chemical acid-base reactions, a numerical approach is required. Mathematical models for CO_2 reduction in aqueous media have already been reported in the literature, but they focused on mercury[51] and copper electrodes,[52] on which the main CO_2 reduction products are formate and hydrocarbons, respectively; hence they are not directly applicable to the present study. A generic steady-state mathematical model is thus set forth and used for data analysis in order to determine kinetic parameters for the rate-determining steps (RDS) of both CO_2 and H_2O reduction. Those parameters are to be used in a mathematical model of the complete electrolysis system, presented in chapter 4. The content of this chapter is as follows: After a first experimental section, the physical picture we have used for CO_2 and H_2O reduction is discussed, and the mathematical model developed. The model is firstly used to simulate an hypothetical case where CO and H_2 evolution reactions are assumed equilibrated (or "reversible"), and finally, experimental data on flat silver and gold electrodes in either aqueous sodium perchlorate or potassium bicarbonate are analyzed using the model and discussed.

3.2 Experimental

The home-made gas-tight electrolysis cell used for the electrolysis on flat metal plates is displayed in figure 3.1. The planar working electrode, consisting of silver in the present study, was set vertically in the cathodic compartment of the cell. A platinum wire was used as the counterelectrode, and immersed in the anodic compartment of the cell. This latter was separated from the cathodic one by means of a Nafion 117 membrane, which prevents gas mixing between the two compartments. The reference electrode consisted of a saturated calomel electrode (SCE) with a salt bridge filled with the same solution as the catholyte, and ending with a Luggin capillary, the extremity of which was placed ca. 1 mm away from the working electrode. Carbon dioxide from a compressed tank (4.8 research grade, 99.998%) was purified by means of an activated carbon filter (Supelcarb HC, Sigma Aldrich). The CO_2 flowrate (referred to room temperature and absolute pressure conditions, i.e., 25 ± 1 °C and 1.013 bar, resp.) to the cathode compartment was between 3 and 30 mL/min depending on the current density used in the experiment, to keep the CO concentration in the cell effluent gas within the gas chromatography (GC) calibration range. The CO_2 flowrate was set using a mass-flow controller (MKS type M100B and 1259C/2259C piloted by a channel readout type 247C) which was initially calibrated for this particular gas. CO_2 was bubbled into the catholyte by means of a glass frit. At the cathode gas outlet, a septum allowed for gas sampling for GC analysis, and a flowmeter was used for an accurate measurement of the outlet flowrate, allowing for a proper determination of current efficiencies. The body of the cathode compartment of the cell was thermostated to 25°C. Turbulent convection within the cathode compartment was set by stirring the solution at 600–1600 rpm.

Planar silver electrodes (99.9995%, Alfa Aesar) of 1 and 1.23 cm^2 (for $KHCO_3$ and $NaClO_4$ electrolytes, respectively) were prepared as follows: They were first polished with a suspension of 1 μm alumina in water for 5 minutes and subsequently ultrasonicated for 1 minute in 1 mol/L KOH, 15 minutes in 0.5 mol/L HNO_3, then 15 minutes in distilled H_2O. The electrolyte used as both catholyte and anolyte was either 0.5 mol/L aqueous

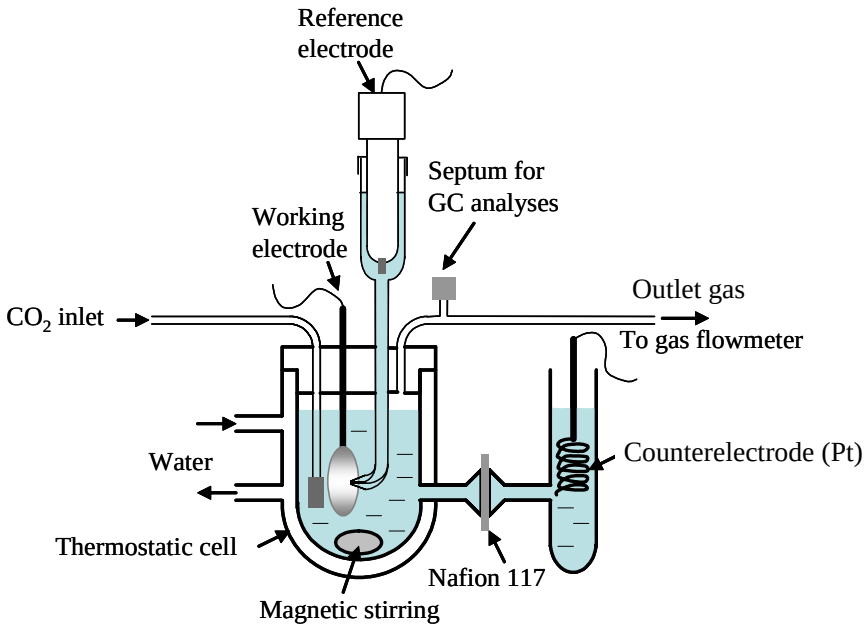

Figure 3.1: Electrochemical cell for studying CO_2 reduction on planar metal electrodes.

potassium bicarbonate (99.7–100.5%, Mallinckrodt Baker, Inc.) or 0.5 mol/L aqueous sodium perchlorate (EMD, 99%). GC analyses of the gaseous products were performed using a GC HP 5890 Series 2 equipped with a packed molecular-sieve column (13X, 60/80, 1.5 m $\times$ 3.1 mm diameter, Alltech Associates Inc.) and a thermal-conductivity detector (TCD). Galvanostatic electrolyses were conducted by means of a potentiostat (M273, Princeton Applied Research) recording both the cathode potential and the anode potential versus the reference electrode.

3.3 Physical picture and assumptions

In spite of many reports in the literature on CO_2 reduction in aqueous electrolytes on electrodes such as silver[3–5,7–9,19–21,53] and gold,[3–5,8,9,19,54–58] the kinetic mechanism of this electrochemical reaction has not been fully clarified yet. Most of the prior studies consider

mechanisms involving the adsorbed anion radical $CO_2^{\bullet -}$ as an intermediate.[4,5,9,54,56] The work by Hori et al.[9] is one of the most comprehensive, and is summarized hereafter. When $CO_2^{\bullet -}$ is formed by a monoelectron transfer on CO_2 at metal electrodes like Ag, Au, Cu, and Zn in aqueous media, it is adsorbed at the surface of the electrode. A following reaction of this adsorbed anion radical with a water molecule leads to another adsorbed radical anion $(O{=}C{-}OH)^{\bullet}$, which is further reduced to CO. On metals such as Cd, Sn, In, Pb, Tl, or Hg, the same anion radical $CO_2^{\bullet -}$ is formed, but it is not adsorbed at the electrode surface. A following reaction with a water molecule leads to a different anion radical of formula $(O{=}CH{-}O)^{\bullet}$ which is further reduced to formate $HCOO^-$. The existence of the anion radical $CO_2^{\bullet -}$ has been shown more than 30 years ago by Aylmer-Kelly et al. by using modulated specular reflectance spectroscopy during electrochemical CO_2 reduction on lead electrodes.[59] However, to our knowledge, the existence of $CO_2^{\bullet -}$ has not been clearly evidenced on metals such as Ag or Au, on which it is likely adsorbed. Beside the most commonly proposed mechanism, a few others have been proposed, e.g., based on adsorbed hydrogen as an intermediate[7] or on dihydroxycarbene formation.[21] An additional argument against a mechanism involving $CO_2^{\bullet -}$ as an intermediate originates from the fairly low overpotential[†] for CO_2 reduction on metals such as Au and Ag (CO_2 reduction occurs at a potential of ca. -1.04 V vs. SCE on Au[54,56] and ca. -1.24 V vs. SCE on Ag[21].) as compared to metals like mercury or lead for instance. The value of the standard potential of $CO_2/CO_2^{\bullet -}$ in case $CO_2^{\bullet -}$ is not adsorbed at the electrode surface was evaluated to be -2.21 V vs. SCE at a mercury drop electrode in a dimethylformamide-based electrolyte by Lamy et al.[60] If one makes the assumption that a similar value holds in aqueous electrolytes, the adsorption energy of $CO_2^{\bullet -}$ on the electrode surface must be fairly strong on metals like Au and Ag in order for the overpotential to be so low.

Following most of the reports on the CO_2 reduction mechanism in aqueous media, we

[†]Throughout this chapter, we refer to overpotentials in magnitude, i.e., it is a positive quantity regardless of whether an oxidation or a reduction reaction is considered.

suppose the existence of adsorbed $CO_2^{\bullet-}$ on the electrode surface

$$CO_2 + e^- \rightarrow CO_{2(ads)}^{\bullet-}. \tag{3.1}$$

Furthermore, we assume that the first electron transfer to CO_2 (yielding adsorbed $CO_2^{\bullet-}$) is the RDS for the electrochemical reaction. This assumption is based on an analogy with nonaqueous solvents, where the formation of $CO_2^{\bullet-}$ was identified as the RDS.[60–62] Molecular dissolved CO_2 is considered as the only active species that is reduced to form the anion radical, i.e., direct reduction of H_2CO_3, HCO_3^-, and CO_3^{2-} is discarded, in agreement with what is shown experimentally in the following and with the literature.[10,63] Because the following reactions leading to CO are assumed fast compared to the formation of $CO_2^{\bullet-}$, we neglect the formation of a secondary intermediate as proposed by Hori et al.[9] and write this as the elementary step

$$CO_{2(ads)}^{\bullet-} + H_2O + e^- \rightarrow CO_{(g)} + 2OH^-. \tag{3.2}$$

For the hydrogen evolution reaction (HER), the formation of adsorbed $H^\bullet$ at the electrode surface (the Volmer reaction) is considered as the RDS

$$H_2O + e^- \rightarrow H_{(ads)}^{\bullet} + OH^-, \tag{3.3}$$

and the following reaction is supposed to be the so-called Heyrovský reaction

$$H_{(ads)}^{\bullet} + H_2O + e^- \rightarrow H_{2(g)} + OH^-. \tag{3.4}$$

Solubilities of CO and H_2 in the aqueous electrolyte are low enough to neglect the existence of soluble forms for these species,[64] i.e., they bubble off the solution as soon as they form. Therefore, reactions 3.2 and 3.4 are assumed irreversible, but still much faster than reactions 3.1 and 3.3, respectively.

Because we deal with aqueous electrolytes, there are homogeneous acid-base reactions that need to be taken into account. Although it is well-known that some of those acid-base reactions have rather slow kinetics (especially those involving conversion of linear carbon-dioxide species to carbonate species, and vice versa, as for instance reaction 3.5 below),[51,52,65] all of them are assumed equilibrated; hence only three independent acid-base reactions are considered, namely

$$\mathrm{HCO_3^-} + \mathrm{H^+} \rightleftharpoons \mathrm{CO_2} + \mathrm{H_2O}, \tag{3.5}$$

$$\mathrm{CO_3^{2-}} + \mathrm{H^+} \rightleftharpoons \mathrm{HCO_3^-}, \tag{3.6}$$

and

$$\mathrm{OH^-} + \mathrm{H^+} \rightleftharpoons \mathrm{H_2O}. \tag{3.7}$$

Note that the $\mathrm{H_2CO_3}$ species is ignored because this is a minor species in the electrolyte in the conditions explored ($c_{\mathrm{H_2CO_3}} \leq 8.3\ 10^{-5}$ mol/L).[52,63]

For simplicity, the hydrodynamics within the cell is described with a stagnant Nernst diffusion layer with a single liquid-phase medium and no convection within this layer. Therefore, we have a steady-state boundary-value problem.

3.4 Mathematical model

Here, we provide a general framework for the case where specified homogeneous and heterogeneous reactions are taken to be equilibrated because they have large rate constants. We attempt a unified treatment and notation but spell out later how heterogeneous (or surface) reactions are treated differently from homogeneous reactions. Let us consider the reaction k written in a general form as

$$\sum_i s_{i,k} M_i^{z_i} \rightleftharpoons n_k e^-, \tag{3.8}$$

with z_i the charge number of species i and $s_{i,k}$ its stoichiometric coefficient in reaction k. The number of electrons exchanged, n_k, is zero if reaction k is not an electrochemical reaction. Whenever this reaction has a finite rate constant, a general kinetic expression applying either to homogeneous or surface reaction reads

$$\begin{aligned} R_k = \quad & k_{f,k} \left(\prod_i a_i^{s_{i,k}} \right)_{s_{i,k}>0} \exp\left(\tfrac{n_k(1-\beta_k)F}{RT}(\Phi_1 - \Phi_2) \right) \\ & - \tfrac{k_{f,k}}{K_k} \left(\prod_i a_i^{-s_{i,k}} \right)_{s_{i,k}<0} \exp\left(\tfrac{-n_k\beta_k F}{RT}(\Phi_1 - \Phi_2) \right). \end{aligned} \tag{3.9}$$

In this equation, a_i denotes c_i (concentration) for a soluble species i, p_i (partial pressure) for a gaseous species i, θ_i (fractional surface coverage) for an adsorbed species i at the surface of the electrode, and 1 for the solvent, water. Empty sites are included among the surface species and need to be included in any kinetic or equilibrium expression. F, R, and T are Faraday's constant, the ideal-gas constant, and the absolute temperature, respectively. Φ_1 is the potential of the metal of the electrode and Φ_2 is the electric potential in the liquid phase. For reaction k, R_k is the rate, $k_{f,k}$ is the forward rate constant, K_k is the equilibrium constant, and β_k is the charge transfer coefficient. For a chemical reaction, $n_k = 0$, and as a consequence exponential terms are set to unity, and β_k is meaningless. The rate constant and the equilibrium constant are in fact apparent because they embed the total surface concentration of sites at the electrode $\Gamma_{\max}$. For the case of homogeneous reactions, no fractional surface coverages are involved in the rate expression. At equilibrium, the rate of the reaction is set to zero in equation 3.9, and a general equilibrium relationship (or Nernst equation whenever $n_k \neq 0$) is obtained

$$K_k = \prod_i a_i{}^{-s_{i,k}} \exp\left(\tfrac{-n_k F}{RT}(\Phi_1 - \Phi_2) \right). \tag{3.10}$$

When dealing with equilibrated reactions, i.e., reactions having an infinite reaction rate constant, Eq. 3.9 is no longer used, and, although the rate of these equilibrated reactions is not zero, Eq. 3.10 holds even though the system is not at equilibrium.

3.4.1 Governing equations

Because fluxes of the soluble species are not directly solved for, the number of unknowns is $n_{\text{sol}} + n_{\text{ads}} + 1$, where n_{sol} is the number of solute species in the Nernst layer and n_{ads} is the number of adsorbed species at the electrode surface (and includes empty sites as well). The additional unknown is the potential Φ_2 in the liquid phase. One can write n_{sol} material balances, which read, at steady state

$$\nabla \cdot \mathbf{N}_i = \sum_{k=1}^{n_h} s_{i,k} R_k, \tag{3.11}$$

where $\mathbf{N}_i$ is the flux density of species i and n_h is the number of homogeneous reactions. The flux density $\mathbf{N}_i$ is expressed using dilute solution theory and reads

$$\mathbf{N}_i = -z_i \frac{D_i}{RT} F c_i \nabla \Phi_2 - D_i \nabla c_i, \tag{3.12}$$

where D_i is the diffusion coefficient of soluble species i. Note that no convection term is considered, as stated above. If there are only reactions with a finite rate constant, the n_{sol} material balances are directly considered as governing equations, after the reaction rates have been substituted for their kinetic expression (Eq. 3.9). Another governing equation is electroneutrality, which holds throughout the Nernst layer

$$\sum_{i=1}^{n_{\text{sol}}} c_i z_i = 0. \tag{3.13}$$

Now if some homogeneous reactions are considered equilibrated, some of the material balances are replaced by the equilibrium relationships (Eq. 3.10) of the n_{h_e} independent equilibrated reactions. In the remaining $n_{\text{sol}} - n_{h_e}$ material balances to be used as governing equations, the reaction rates R_k of the equilibrated reactions are eliminated by the following procedure. The material balance of a species i involved in an equilibrated reaction k (i.e., $s_{i,k} \neq 0$) is used to eliminate the reaction rate R_k of that reaction from all the other material

balances. We proceed in a like manner to eliminate all the rates of equilibrated reactions that remain in the material balances. Note that more than one equilibrated reaction may be eliminated at a given step if all the equilibrated reactions considered are not independent. Therefore, this procedure is applied n_{h_e} times. From this general procedure, an algorithm based on this method was written for treating any set of reactions where certain reactions are equilibrated. This is exemplified in the appendix with the system under investigation in this work.

3.4.2 Boundary conditions

At the electrode surface ($x = 0$), one can write n_{sol} equations relating the normal component of the flux of a soluble species i to the reaction rates of surface reactions that involve this species

$$N_i = -\sum_{k=n_h+1}^{n_h+n_s} s_{i,k} R_k. \tag{3.14}$$

In a similar fashion, one can write $n_{\text{ads}} - 1$ material balances for adsorbed species at the surface of the electrode. The material balance of an adsorbed species i is expressed using equation 3.14 where the flux N_i is zero. Finally, there is a material balance on fractional surface coverages, which reads

$$\sum_{i=1}^{n_{\text{ads}}} \theta_i = 1. \tag{3.15}$$

In the absence of any equilibrated reactions (homogeneous or heterogenous), $n_{\text{ads}} + n_{\text{sol}} - 1$ flux conditions (Eq. 3.14) are used. The surface reaction rates R_k in equation 3.14 can be replaced by their kinetic expressions (Eq. 3.9). If some equilibrated homogeneous reactions are considered, some of the flux conditions have to be replaced by the equilibrium relationships (Eq. 3.10) of the n_{h_e} independent equilibrated homogeneous reactions. On a physical basis, this is equivalent to saying that the reaction-layer thickness for an equilibrated

homogeneous reaction tends toward zero, and thus this reaction proceeds at the boundary as well. The remaining flux conditions apply on the $n_{\text{sol}} - n_{h_e}$ independent fluxes that were defined in the previous subsection. Furthermore, if equilibrated surface reactions are considered, some of these modified flux conditions have to be replaced by the equilibrium relationships (Eq. 3.10) of the n_{s_e} independent equilibrated surface reactions. The remaining $n_{\text{sol}} - n_{h_e} - n_{s_e}$ flux conditions will be derived using a similar method as that used for deriving the material balances. (Use the procedure outlined below Eq. 3.13, as detailed in the appendix.)

At the boundary between the Nernst layer and the bulk solution ($x = \delta$), the composition of the electrolyte is set to that of the bulk. The concentration of some of the species is set directly (e.g., CO_2 concentration is set by means of a Henry relationship) while equilibrium relationships (Eq. 3.10) for the homogeneous reactions (both equilibrated reactions and those with a finite rate constant) are used together with electroneutrality to derive the others. Additionally, Φ_2 is arbitrarily set to zero at this boundary.

The formulation of a proper set of governing equations when dealing with equilibrated reactions has already been reported in the literature,[66–72] but to our knowledge no general method was detailed in order to derive a proper set of equations in a systematic way.

3.4.3 Numerical solution

The bandmap of the mathematical model is provided in figure 3.2. A general computer program was written, based on the governing equations and boundary conditions detailed above. It is general in the sense that any species can be considered, and involved in any homogeneous or heterogeneous reaction that can either have a finite rate constant or be considered equilibrated. The system of equations was cast into finite differences and solved

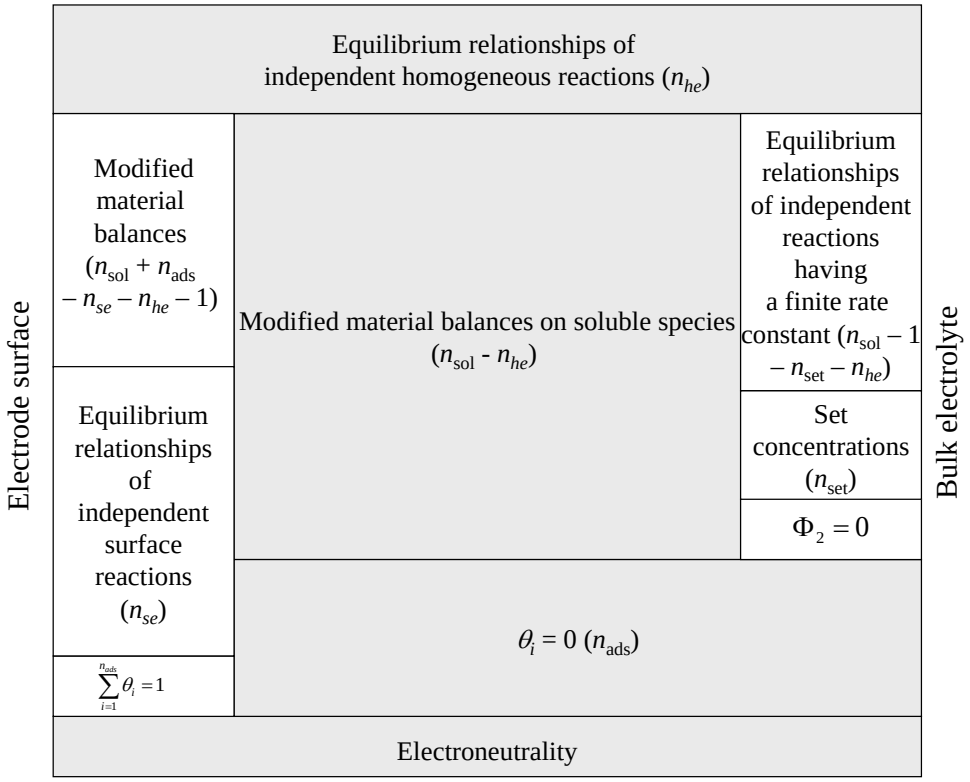

Figure 3.2: Bandmap of the mathematical model of the electrochemical cell. The number of equilibrated reactions must be less than the number of independent reactions, i.e., $n_{h_e} \leq n_{\text{sol}} - 1$ and $n_{h_e} + n_{s_e} \leq n_{\text{sol}} + n_{\text{ads}} - 2$.

numerically by using Newman's BAND(j) subroutine.[35] 100 mesh intervals were used across the Nernst layer. The set of governing equations is solved by setting the value of $\Phi_1|_{x=0} - \Phi_2|_{x=0}$. Once a converged solution is obtained, the current density is calculated, along with the working electrode potential V (referred to a reference electrode) using the following equation

$$V = (\Phi_1|_{x=0} - \Phi_2|_{x=0}) + (\Phi_2|_{x=0} - \Phi_2|_{x=x_{\text{RE}}}) + (\Phi_2 - \Phi_1)_{\text{RE}}. \tag{3.16}$$

The term $(\Phi_2 - \Phi_1)_{\text{RE}}$ is dependent upon the kind of reference electrode chosen as well as on the way the potential is defined, as developed by Newman and Thomas-Alyea.[35] The term $(\Phi_2|_{x=0} - \Phi_2|_{x=x_{\text{RE}}})$ is the liquid-phase potential difference between the electrode surface and the reference electrode and is due to both diffusion and migration limitations in the Nernst

layer ($0 < x < \delta$), and solely to migration limitations outside the Nernst layer ($\delta < x < x_{\mathrm{RE}}$).

3.5 Results and discussion

3.5.1 Equilibrated electrochemical reactions

Preliminary to getting into the analysis of experimental data for CO_2 reduction on silver and gold, the hypothetical case for which all reactions involved are reversible, including CO_2 and H_2O reduction, was looked at in two different aqueous electrolytes, namely 0.5 mol/L $KHCO_3$ and 0.5 mol/L $NaClO_4$, both saturated with CO_2. Of course, this hypothetical case study does not apply to the actual situation on gold and silver electrodes (which are not reversible electrodes for CO or H_2 evolution reactions), and underlines the importance of surface-reaction kinetics on the product distribution. CO and H_2 evolution reactions were considered separately to avoid the effect of one electrochemical reaction on the other. (The case where these reactions are considered together is discussed in the following.) For each simulation, the partial pressure for CO or H_2, used in the Nernst relationship (Eq. 3.10), was set to 1 bar, respectively. The other input parameters used for simulations are provided in table 3.1. The overall electrochemical reactions for CO_2 reduction to CO and H_2O reduction to H_2 (provided in table 3.1 together with their standard potential) are considered instead of reactions (3.1 + 3.2) and (3.3 + 3.4), respectively. The standard potentials for those last four reactions depend on the adsorption energies of $CO_2^{\bullet -}{}_{(\mathrm{ads})}$ and $H^{\bullet}{}_{(\mathrm{ads})}$ on the electrode surface and are unknown.

Simulated current–potential characteristics at steady-state are presented in figure 3.3. For both electrolytes, HER occurs at a more positive potential (147 mV) compared to the CO evolution reaction (CER). This means that H_2 evolution is thermodynamically favored over CO evolution (as reflected in the standard potentials). Both CO and H_2 evolution are positively shifted by 201 mV when aqueous $NaClO_4$ is used as electrolyte instead of $KHCO_3$.

Table 3.1: List of input model parameters. Equilibrium constants are taken at ionic strength = 0.5 mol/L and therefore are apparent constants. a: assumed parameters; s: set parameters

Parameter		Value	Ref.
Temperature (°C)		25	s
CO_2 pressure (bar)		1.013	s
Diffusion coefficient (cm^2/s)	OH^-	$5.26\ 10^{-5}$	35
	H^+	$9.312\ 10^{-5}$	35
	CO_3^{2-}	$0.955\ 10^{-5}$	73
	HCO_3^-	$1.105\ 10^{-5}$	35
	CO_2	$1.97\ 10^{-5}$	74
	K^+	$1.957\ 10^{-5}$	35
	Na^+	$1.334\ 10^{-5}$	35
	ClO_4^-	$1.792\ 10^{-5}$	35
Equilibrium constant in			
(L/mol)	$CO_3^{2-} + H^+ \rightleftharpoons HCO_3^-$	$10^{9.73}$	75
(L/mol)	$H^+ + HCO_3^- \rightleftharpoons CO_2 + H_2O$.	$10^{6.05}$	75
$(mol/L)^2$	$H_2O \rightleftharpoons OH^- + H^+$.	$10^{-13.74}$	75
(mol/L bar)	$CO_{2(g)} \rightleftharpoons CO_2$	$10^{-1.491}$	75
Standard potential	$2H^+ + 2e^- \rightleftharpoons H_{2(g)}$	0	76
(V vs. HE)	$CO_2 + 2H^+ + 2e^- \rightleftharpoons CO_{(g)} + H_2O_{(l)}$	-0.103	76
Distance between WE and RE (cm)		0.1	a
Potential of SCE (V vs. HE)		0.244	77

This is because the pH of the aqueous $NaClO_4$ electrolyte is lower than that of $KHCO_3$, i.e., 3.91 compared to 7.27. However, as expected, the difference between equilibrium potentials for CO_2 and H_2O reduction does not depend upon pH.

The current–potential characteristics are composed of several waves because CO_2 and H_2O reduction reactions involve several acid-base species depending on the overpotential. This is exemplified for CO evolution in 0.5 mol/L $KHCO_3$ in figure 3.4, where the calculated concentrations of the various soluble species at the electrode surface and the pH are represented as a function of the electrode potential. Three waves are clearly identified from the

derivative of the current–potential curve. The first one (at low overpotentials) corresponds to CO_2 reduction to CO, with simultaneously formed HCO_3^-. At more negative potentials, HCO_3^- is reduced to CO, and CO_3^{2-} is formed, the latter being reduced at more negative electrode potential to CO, with OH^- formed simultaneously (third wave). The detail of these electrochemical reactions is provided in the caption of figure 3.3. (Similarly, the detail of the electrochemical reactions when HER only is considered is provided in the caption too.) Because all the reactions (including CER) are assumed equilibrated, choosing $CO_2 + H_2O + 2e^- \rightleftharpoons CO_{(g)} + 2OH^-$ as the electrochemical reaction in the model is strictly equivalent to considering reaction a, b, or c (see caption of figure 3.3) as the electrochemical reaction. The same holds true for HER.

Those simulations do not provide any information on the reactions kinetics. However, they clearly emphasize that for a hypothetical electrode on which the kinetics of both CER and HER are fast, one does not expect CO to be produced from an aqueous medium. They also provide insights on how CO evolution on a hypothetical electrode reversible for CER and on which HER is completely suppressed would depend on the electrolyte; a much larger CO current density is expected in $KHCO_3$ as compared to $NaClO_4$ under similar hydrodynamic conditions (at potentials $<$ -0.9 V vs. SCE). This is because CO_2 is produced through bicarbonate decomposition in a reaction layer adjacent to the electrode.

Finally, if a simulation taking both CER and HER to be equilibrated is performed (with $p_{H_2} = 1$ bar for instance and p_{CO} set by CER and HER Nernst equations for a specified electrode potential), CO evolution is negligible, and the total current agrees with that calculated for the case where HER only was considered.

3.5.2 Experimental results

Now that we have looked carefully at the electrochemical behavior for reversible CO and H_2 evolution reactions, we focus on experimental results on silver and gold flat electrodes.

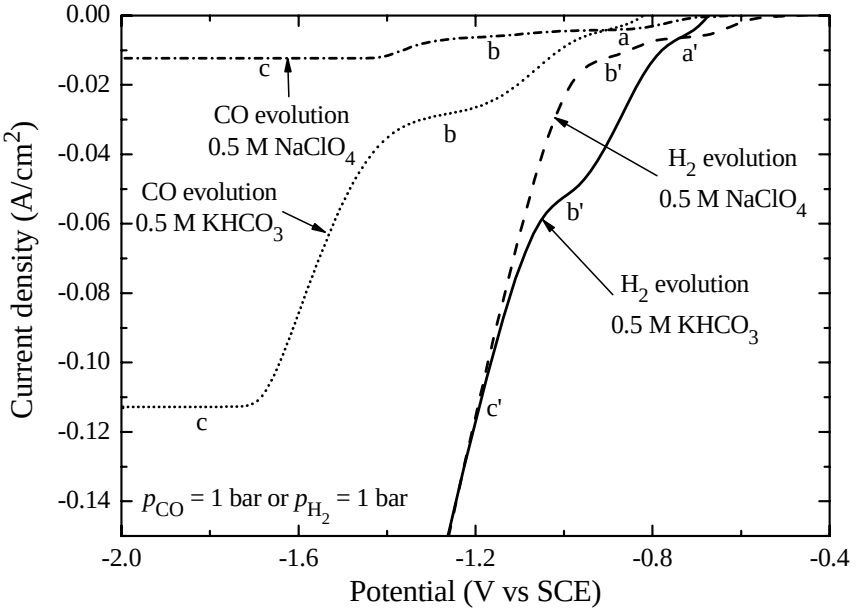

Figure 3.3: Simulated steady-state current density as a function of cathode potential for HER (CER) when it is assumed equilibrated and CER (HER) is discarded. ($p_{H_2} = 1$ bar when HER only; $p_{CO} = 1$ bar when CER only; thickness of the Nernst layer = 0.01 cm). a: $3CO_2 + H_2O + 2e^- \rightleftharpoons CO_{(g)} + 2HCO_3^-$, b: $4HCO_3^- + 2e^- \rightleftharpoons CO_{(g)} + 2H_2O + 3CO_3^{2-}$, c: $CO_3^{2-} + 2H_2O + 2e^- \rightleftharpoons CO_{(g)} + 4OH^-$, a': $2CO_2 + 2H_2O + 2e^- \rightleftharpoons H_{2(g)} + 2HCO_3^-$, b': $2HCO_3^- + 2e^- \rightleftharpoons H_{2(g)} + 2CO_3^{2-}$, c': $2H_2O + 2e^- \rightleftharpoons H_{2(g)} + 2OH^-$. Reactions a, b, and c, and a', b', and c', are written based on the predominate species, as functions of potential (see figure 3.4).

A comprehensive experimental study was reported by Hori et al. for CO_2 reduction on a flat gold electrode in $KHCO_3$,[54] hence we use these results for the present analysis. In spite of the numerous reports dealing with CO_2 reduction on silver electrodes (see for instance table 1.2 where some electrolysis data in $KHCO_3$ electrolyte are summarized), we could not find experimental data showing partial current densities of CO_2 reduction products as a function of the electrode potential in the literature, hence an experimental study was carried out to this end. Figure 3.5 presents the partial current densities for H_2 and CO evolution reactions on a silver electrode in 0.5 mol/L $KHCO_3$ and 0.5 mol/L $NaClO_4$. In contrast to the case with the equilibrated simulations, CO evolution is observed. No CO_2 reduction product other than CO, neither soluble (e.g., formate) nor gaseous (e.g., methane)

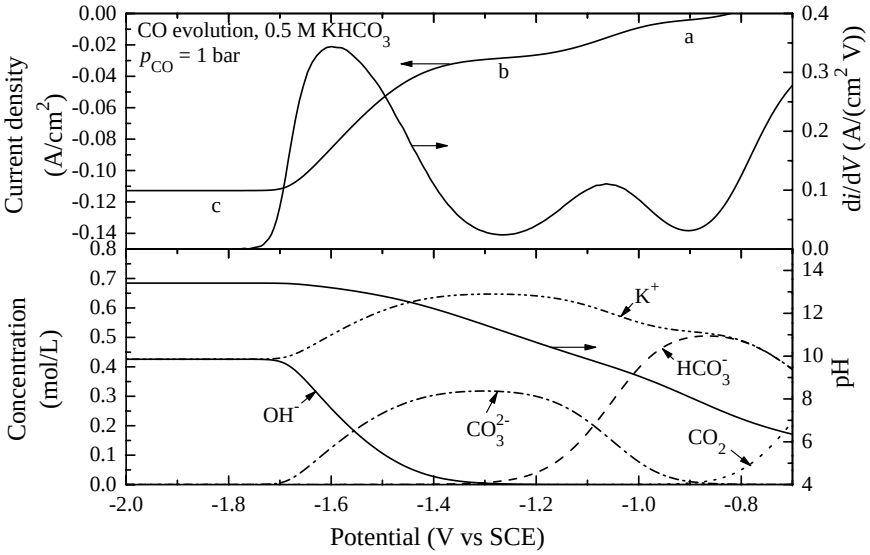

Figure 3.4: Simulated steady-state current density and concentrations of soluble species at the electrode as a function of cathode potential for equilibrated CER, with HER being discarded. (p_{CO} = 1 bar; thickness of the Nernst layer = 0.01 cm). Reactions a, b, and c, are as defined in the caption of figure 3.3.

was found in substantial amount; hence only CO is considered in the following. This is consistent with the sum of CO and H_2 partial current densities, which is close to the current density applied experimentally during the electrolysis, as seen on figure 3.5. Data obtained at 15 min electrolysis were selected because of a trade off between the time required for the experimental system to reach a pseudo-steady state and the loss of CO current efficiency that slowly occurs upon electrolysis, especially in the potassium bicarbonate electrolyte. Figure 3.6 represents the current efficiencies of CO and H_2 during a 2 hour-electrolysis at -7.5 mA/cm^2 in 0.5 mol/L $KHCO_3$, selected here as an example. After an initial increase during about 10 minutes, CO current efficiency is stable for about 10 min and subsequently decays. This last decay is ascribed to a poisoning effect, as already described in the literature.[20–24, 78] Partial current densities for CO evolution are pretty similar for both electrolytes, but not for hydrogen evolution, where the overpotential is higher in the perchlorate electrolyte (figure 3.5). This explains why the maximum of CO current efficiency, located around -1.7 V vs. SCE regardless of the electrolyte, is much higher in the perchlorate (96%) as compared to

that in the bicarbonate (68%). At lower electrode potentials, hydrogen evolution becomes predominant over CO evolution, resulting in a decay of CO efficiency. In the perchlorate electrolyte, there is a plateau for hydrogen evolution (Inset of figure 3.5), located at ca. -0.25 mA/cm^2 for potentials ranging from ca. -1.05 to -1.7 V vs. SCE. A similar plateau was reported by Kostecki et al. and was attributed to the diffusion-limited reduction of protons.[21,63] This is probably why such a plateau is not detected in $KHCO_3$ electrolyte, where the proton concentration is much smaller. Because of this plateau, the current efficiency for hydrogen evolution (in perchlorate) is almost 100% at low overpotentials ($V > -1.2$ V vs. SCE), where no appreciable CO evolution occurs. This current efficiency for hydrogen then goes through a minimum and then rises again as the electrode potential is further decreased.

Simulations of CO and H_2 evolution in both electrolytes were conducted. With regard to HER, the effect of the electrolyte mentioned above could be the signature of a different RDS. However, for the sake of simplicity, the same RDS was also picked for HER in the two electrolytes (reaction 3.3). To account for the irreversibility of both H_2 and CO evolution reactions, Tafel-like expressions (equation 3.9 without the anodic term) were considered for the RDSs, as well as for the following reactions (for which substantially high rate constants were arbitrarily used). Tafel-like expressions were used for the following reactions instead of assuming them equilibrated because we have no information about their standard potentials. As long as the rate constants of the following reactions are set to substantially high values, the simulation is not dependent on those values, except the coverage fractions of the electrode surface by the adsorbed species $CO_2^{\bullet -}$ and $H^\bullet$ that tend artificially toward zero as higher corresponding rate-constant values are chosen (i.e., the electrode surface is almost bare). Rate constants and charge-transfer coefficients obtained from adjustments of the experimental data are provided in table 3.2, together with the adjusted thickness of the Nernst layer, and the resulting simulations are overlaid to the experimental data in figure 3.5. Note that the fitting done here was by hand, and only enough iterations were completed to achieve qualitative accuracy. The value of the charge-transfer coefficient of 0.38 derived from data in the perchlorate electrolyte for CO evolution is pretty close to that (0.33) reported

by Kostecki et al. on a silver electrode in 0.1 M $NaClO_4$.[21]

Table 3.2: Rate constants (suitable for use with a quasi-electrostatic potential with H^+ as reference species), charge-transfer coefficients, calculated electrode potentials at -10 mA/cm^2, and thickness of the Nernst layer adjusted from experimental data on silver and gold planar electrodes at room temperature.

	Ag		Ag		Au	
	$KHCO_3$ 0.5 M		$NaClO_4$ 0.5 M		$KHCO_3$ 0.5 M	
	CO	H_2	CO	H_2	CO	H_2
Rate constant (cm/s for CER and mol/cm^2 s for HER)	5.8 10^{-9}	8.3 10^{-13}	8.0 10^{-12}	3.0 10^{-19}	5.8 10^{-9}	3.6 10^{-13}
Charge-transfer coefficient	0.25	0.20	0.38	0.44	0.35	0.23
Potential at -10 mA/cm^2 (V vs. SCE)	-1.69	-1.82	-1.69	-1.91	-1.32	-1.71
Thickness of the Nernst layer (μm)	18		32		80	

The simulations are in pretty good agreement with the experimental data, although, for H_2 evolution on a silver electrode in the perchlorate electrolyte, the current plateau at -0.25 mA/cm^2 detailed above is not accounted for. We have considered using a finite rate constant for reaction 3.5 as in refs. 51, 52, 65, but the results were not quantitatively satisfying unless several elementary steps are considered for $H^\bullet$ formation. For the sake of simplicity, we are therefore reporting only results with all the homogeneous reactions assumed to be equilibrated, even though the plateau at small currents in perchlorate is not reproduced. The limiting current density of the plateau, assumed to be due to proton reduction to hydrogen, was used to get a rough estimate of the thickness of the diffusion

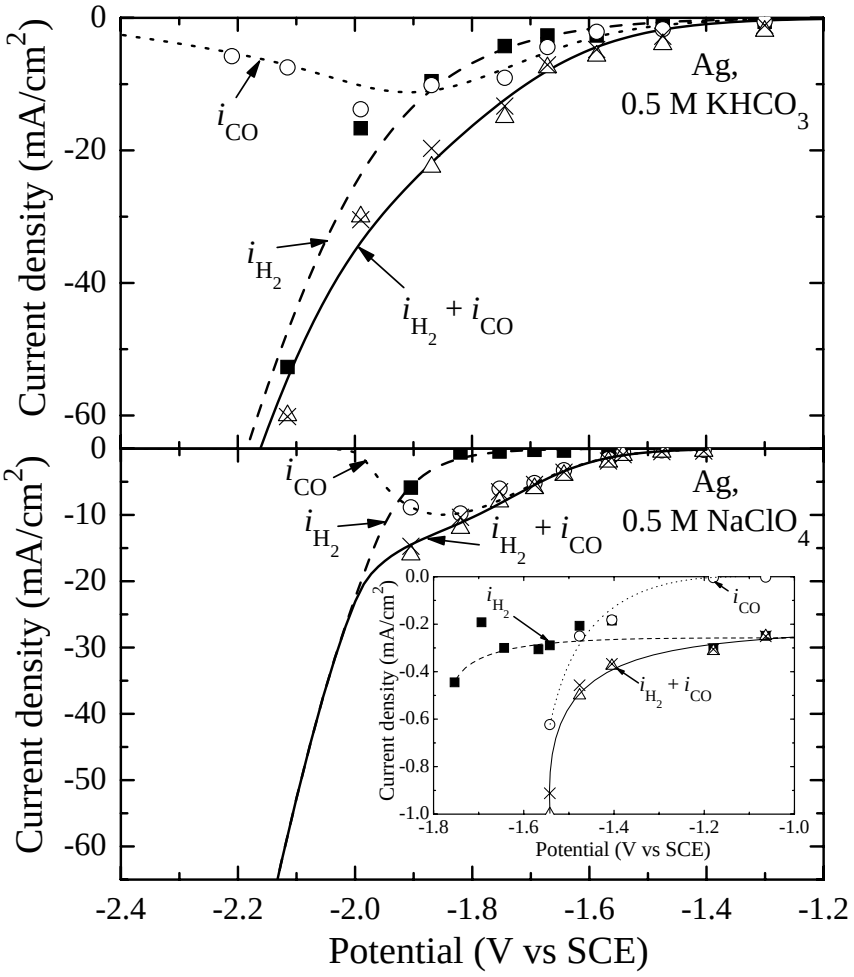

Figure 3.5: Experimental partial current densities for CO (○) and H_2 (■) evolution on a silver planar electrode as a function of cathode potential at 15 min electrolysis, sum of CO and H_2 partial current densities (△), total current density (×), and simulated curves (lines). Inset: Zoom on the current plateau for H_2 evolution at low overpotential. (Lines in the inset are not from simulation and have been added for eye guidance only.)

layer, by means of the following equation

$$\delta = \frac{F D_{\mathrm{H^+}} c^0_{\mathrm{H^+}}}{i_{\mathrm{H_2,lim}}}, \tag{3.17}$$

with $c^0_{\mathrm{H^+}}$ the proton concentration in the bulk (derived from the theoretical pH of the electrolyte) and $i_{\mathrm{H_2,lim}}$ the limiting current density. A thickness of ca. 44 μm is found, which

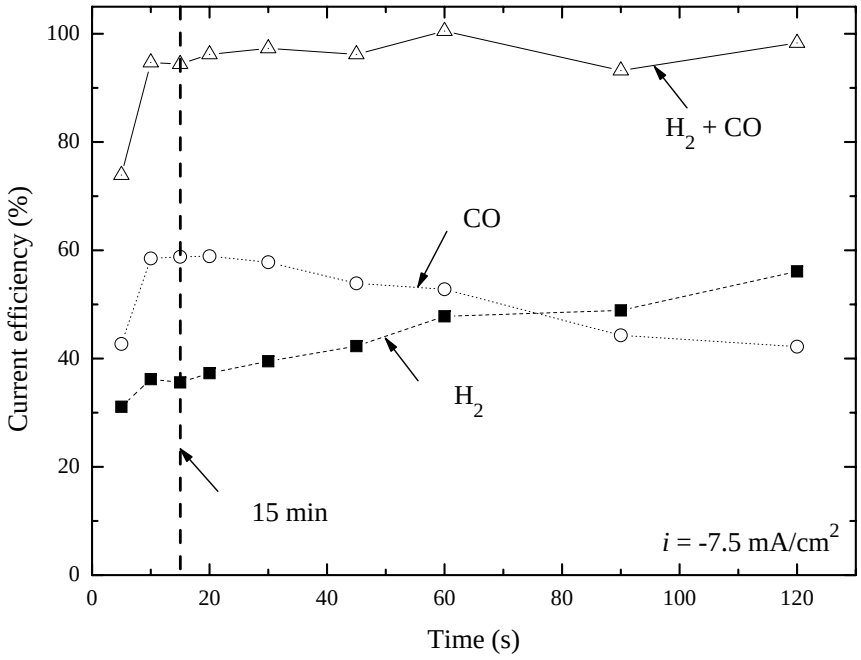

Figure 3.6: CO (○) and H_2 (■) current efficiencies and sum of CO and H_2 current efficiencies (△) as a function of run time for an electrolysis performed on a Ag electrode in 0.5 mol/L $KHCO_3$.

is of the same order than the value of 32 μm that was adjusted using the model at a lower potential than that of the plateau. Note that Eq. 3.17 is valid only if no acid-base reactions are coupled with proton reduction.

The same approach was also carried out on gold planar electrodes in 0.5 mol/L $KHCO_3$, but with experimental data from ref. 54, which are reproduced in figure 3.7. Similarly to silver electrodes, unlike the case where HER and CER are equilibrated, CO evolution is observed. Both CO and H_2 evolution occur at a lower overpotential on gold as compared to silver. CO current efficiency is pretty high (ca. 90%) at low overpotential, and decays at higher overpotentials, where hydrogen evolution becomes substantial. Just like we did for silver, CO was considered as the only CO_2 reduction product, although small amounts of formate ions were found in the electrolyte after electrolysis.[54] Simulations of the partial current densities of CO and H_2 as a function of electrode potential were performed, using

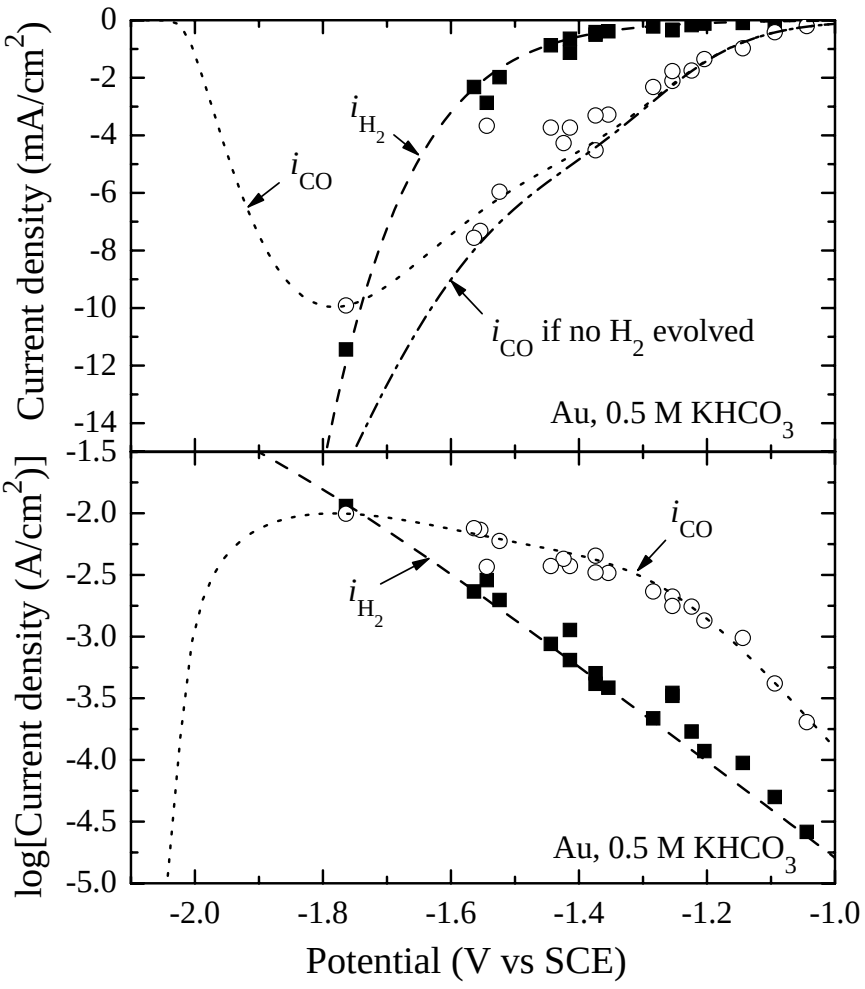

Figure 3.7: Experimental partial current densities for CO (○) and H_2 (■) evolution on a gold planar electrode as a function of cathode potential reproduced from Ref. 54, and simulated curves (lines).

the same RDSs as for silver electrodes, and are overlaid to the experimental data on figure 3.7. Although the experimental data are reported at 18°C, the parameter values of table 3.1 were used in the model. Just like for silver, we have considered using a finite rate constant for reaction 3.5, but a poorer agreement with the experimental data was found in this case, regardless of the thickness of the diffusion layer we chose. We are therefore reporting only results with all the homogeneous reactions assumed to be equilibrated. The Tafel plot given in figure 3.7 shows that hydrogen evolution exhibits a Tafel behavior over the entire potential

range investigated, and this behavior is well captured by the simulation. This might confirm that H_2 comes from H_2O reduction. The kinetic parameters for CO and H_2 evolution, as well as the thickness of the Nernst layer adjusted by hand from the experimental data, are provided in table 3.2. At this point, it is interesting to compare the parameters for gold with those obtained for silver. The values of the charge transfer coefficient for both reactions on Au and Ag in potassium bicarbonate are fairly close to each other, which supports the hypothesis of similar RDSs on the two metal electrodes. In order to compare the reaction kinetics, the electrode potentials at a current density of -10 mA/cm^2 were calculated based on the kinetic parameters of each reaction. CER and HER clearly occur at more positive potentials (ca. 370 and 110 mV, respectively) on gold as compared to silver. Finally, the large differences in the Nernst layer thicknesses suggest different hydrodynamics in the experimental setups, likely due to different stirring rates.

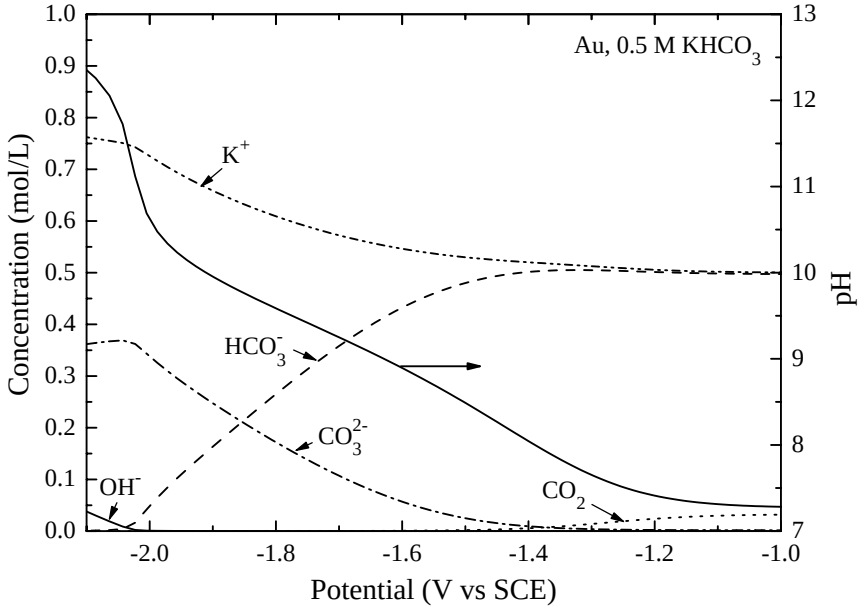

Figure 3.8: Simulated concentrations of soluble species at the gold planar electrode as a function of cathode potential with input parameters adjusted from experimental data provided in Ref. 54.

Simulated concentrations of soluble species next to the gold electrode are displayed as

a function of the electrode potential in figure 3.8, together with the pH. It shows that the electrolyte next to the electrode surface becomes more basic when the electrode potential is decreased. Qualitatively, a similar behavior as for the equilibrated case is observed (compare with figure 3.4). However, because two parallel electrochemical reductions occur simultaneously (i.e., CER and HER), the increase of pH is more pronounced at a same potential value. As an illustration to this statement, we simulated the current density of CO evolution on a gold electrode if no hydrogen evolution occurs. This simulation, shown in figure 3.7, reveals a higher current density for CO evolution in the absence of hydrogen evolution, especially at low potential values. This is due to a lower pH increase next to the electrode as compared to the case where HER proceeds simultaneously. At more negative potentials, the current density for CO evolution goes on increasing until it reaches a limiting current density of ca. -141 mA/cm^2, due to the complete depletion of CO_2 and carbonate species at the electrode surface (not shown here). Of course, we recall that this simulation encompasses the assumption that all homogeneous acid-base reactions are equilibrated, which may not be realistic anymore at high values of current density; in practice, it is expected that the rate-limited acid-base reactions forming CO_2 from carbonate species near the electrode surface yield a much lower limiting current density for CO evolution.

Finally, the influence of CO_2 partial pressure on the current density for CER was examined, using experimental data taken from ref. 54. Experimental data show that for a specified electrode potential the partial current density of CER is linear with CO_2 partial pressure, which qualitatively suggests that CER is first order with respect to the concentration of dissolved CO_2. However, it is noteworthy on figure 3.9 that a linear fit of the data points does not go through zero, especially for the curve at lower electrode potential. The simulation using the parameters previously adjusted (table 3.2) does a pretty good job in capturing the quasi-linear behavior in the CO_2 partial pressure range that was studied experimentally. Furthermore, it clearly shows a nonlinearity at low partial pressures, so that CER current density becomes zero when CO_2 partial pressure is zero, as expected. The CER current density is in fact proportional to the CO_2 concentration at the electrode, which is

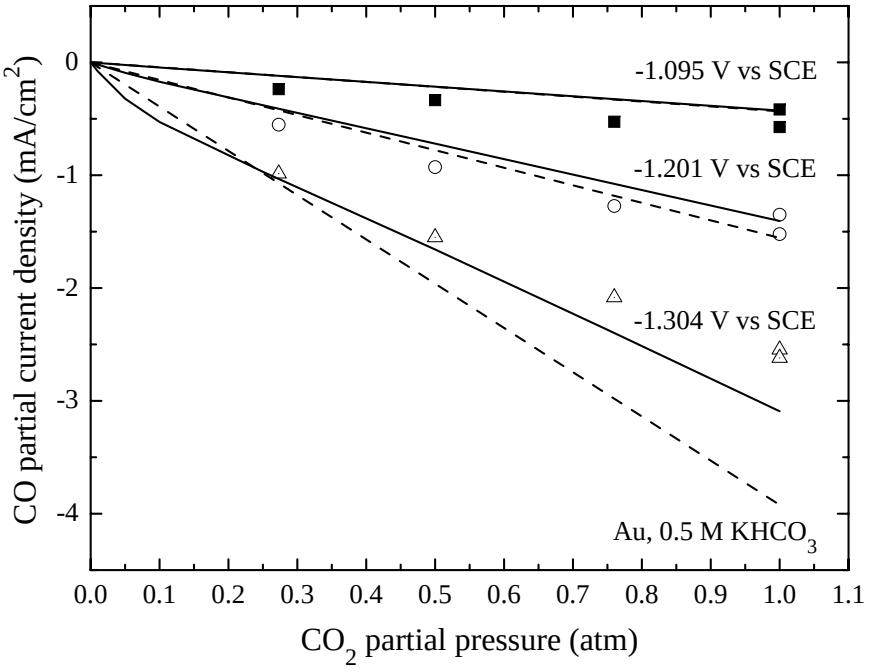

Figure 3.9: Experimental CO partial current densities on a gold planar electrode as a function of the CO_2 partial pressure of the gas in contact with the electrolyte, reproduced from Ref. 54 (symbols), simulated CO partial current densities using the model (solid lines), and calculated using Eq. 3.18 (dashed lines).

therefore nonlinear as well at low CO_2 partial pressure. This is because of the homogeneous acid-base reactions coupled with the CER. In the hypothesis of no coupled reactions, an analytic expression for the CER current density at steady state can be derived[35]

$$i_{\mathrm{CER}} = -\frac{2Fk_{\mathrm{CER}}\, c_{\mathrm{CO_2}}|_{x=\delta} \exp\left[-\frac{\beta_{\mathrm{CER}}F}{RT}\left(V-(\Phi_2-\Phi_1)_{\mathrm{RE}}\right)\right]}{1+\frac{2k_{\mathrm{CER}}\delta}{D_{\mathrm{CO_2}}}\exp\left[-\frac{\beta_{\mathrm{CER}}F}{RT}\left(V-(\Phi_2-\Phi_1)_{\mathrm{RE}}\right)\right]}, \tag{3.18}$$

where k_{CER} and β_{CER} are the cathodic rate constant and charge transfer coefficient for CER, respectively. Note that for simplicity, the potential drop in the electrolyte between the working and reference electrodes was neglected in equation 3.18. The current densities calculated using this equation are also provided in figure 3.9. For the highest potential (-1.095 V vs. SCE), the simulations from the model and equation 3.18 are very close to each other, meaning that CER is not much affected by the acid-base reactions (i.e., the pH is

nearly uniform across the diffusion layer). This is clearly not the case at lower potentials.

3.6 Conclusion

Data for CO_2 (and H_2O) reduction to CO (and H_2) on flat gold and silver electrodes in aqueous electrolytes were investigated using a mathematical model. This model, although applied to this particular case study, is generic, and can be used to analyze any electrochemical steady-state problem with a Nernst layer of defined thickness. Several parallel electrochemical reactions, possibly coupled with homogeneous chemical reactions, can readily be accounted for, and these reactions can either have a finite rate constant or be assumed equilibrated. As a preliminary step, simulations were performed where HER and CER are taken equilibrated and revealed that no CO is expected if HER and CER are reversible, highlighting that the CO/H_2 selectivity mainly depends on electrode kinetics. For both gold and silver electrodes, the rate-determining steps for CO_2 and H_2O reduction reactions were supposed to be the formation of $CO_2^{\bullet -}$ and $H^{\bullet}$ radicals adsorbed at the electrode surface, respectively. Based on this assumption, rate constants and charge transfer coefficients for CO_2 and H_2O reduction were adjusted from the experimental data. The values of the charge transfer coefficients for CER and HER on Au and Ag in potassium bicarbonate are fairly close to each other, which supports the hypothesis of similar RDSs on the two metal electrodes. It is found that CO_2 reduction to CO is positively shifted by ca. 370 mV on gold as compared to silver, while HER is positively shifted by only ca. 110 mV. This explains why higher CO current efficiencies are obtained on gold (ca. 90% for gold as compared to only ca. 68% on silver in potassium bicarbonate). The CER current fade at low electrode potentials is related to the HER current increase, which yields a high pH increase at the electrode surface leading to a decrease of the local dissolved CO_2 concentration. Finally, an analysis of data for various CO_2 partial pressures in equilibrium with the electrolyte was performed, in which the effect of acid-base reactions coupled with the CER was accounted for. All these results are used for analyzing data obtained with the complete electrolysis cell

in chapter 4.

3.7 Appendix

Let us illustrate here how the algorithm for deriving modified material balances works, based on the example of CO_2 and H_2O reduction at either a silver or gold electrode in 0.5 mol/L $KHCO_3$. We consider homogeneous reactions 3.5, 3.6, and 3.7 to be equilibrated, while surface reactions 3.1, 3.2, 3.3, 3.4 are assumed to follow Tafel-like kinetics. The original set of material balances reads

$$\begin{cases} \nabla \cdot \mathbf{N}_{CO_2} = R_5 \\ \nabla \cdot \mathbf{N}_{HCO_3^-} = -R_5 + R_6 \\ \nabla \cdot \mathbf{N}_{CO_3^{2-}} = -R_6 \\ \nabla \cdot \mathbf{N}_{H^+} = -R_5 - R_6 - R_7 \\ \nabla \cdot \mathbf{N}_{OH^-} = -R_7 \\ \nabla \cdot \mathbf{N}_{K^+} = 0 \end{cases} . \tag{3.19}$$

The material balance of CO_2 is used to eliminate R_5, and the equilibrium relationship of reaction 5 is substituted as a governing equation. The set of material balances becomes

$$\begin{cases} \nabla \cdot \mathbf{N}_{HCO_3^-} = -\nabla \cdot \mathbf{N}_{CO_2} + R_6 \\ \nabla \cdot \mathbf{N}_{CO_3^{2-}} = -R_6 \\ \nabla \cdot \mathbf{N}_{H^+} = -\nabla \cdot \mathbf{N}_{CO_2} - R_6 - R_7 \\ \nabla \cdot \mathbf{N}_{OH^-} = -R_7 \\ \nabla \cdot \mathbf{N}_{K^+} = 0 \end{cases} . \tag{3.20}$$

A second step is to eliminate R_6 using the material balance of HCO_3^-. The equilibrium relationship of reaction 6 is then used as a governing equation, and the set of material

balances becomes

$$\begin{cases} \nabla \cdot \mathbf{N}_{CO_3^{2-}} + \nabla \cdot \mathbf{N}_{HCO_3^-} + \nabla \cdot \mathbf{N}_{CO_2} = 0 \\ \nabla \cdot \mathbf{N}_{H^+} = -2\nabla \cdot \mathbf{N}_{CO_2} - \nabla \cdot \mathbf{N}_{HCO_3^-} - R_7 \\ \nabla \cdot \mathbf{N}_{OH^-} = -R_7 \\ \nabla \cdot \mathbf{N}_{K^+} = 0 \end{cases} . \tag{3.21}$$

As a final step, the material balance on H^+ is used to eliminate R_7, and the equilibrium relationship of reaction 7 is used as a governing equation. We end up with a set of 3 material balances, which, after rearrangement, reads

$$\begin{cases} \nabla \cdot \mathbf{N}_{CO_3^{2-}} + \nabla \cdot \mathbf{N}_{HCO_3^-} + \nabla \cdot \mathbf{N}_{CO_2} = 0 \\ \nabla \cdot \mathbf{N}_{H^+} = 2\nabla \cdot \mathbf{N}_{CO_3^{2-}} + \nabla \cdot \mathbf{N}_{HCO_3^-} + \nabla \cdot \mathbf{N}_{OH^-} \\ \nabla \cdot \mathbf{N}_{K^+} = 0 \end{cases} . \tag{3.22}$$

The first one looks like a carbon balance, and the second one looks like a charge balance. This shows that there are only three independent fluxes because of the equilibrated reactions. Flux boundary conditions at the electrode are expressed as a function of these three independent fluxes. Two material balances are considered for the adsorbed species ($CO_2^{\bullet -}$ and $H^\bullet$)

$$\begin{cases} N_{CO_2} + N_{HCO_3^-} + N_{CO_3^{2-}} = -R_1 \\ N_{H^+} - 2N_{CO_3^{2-}} - N_{HCO_3^-} - N_{OH^-} = -2R_2 - R_3 - R_4 \\ N_{K^+} = 0 \\ 0 = R_1 - R_2 \\ 0 = R_3 - R_4 \end{cases} . \tag{3.23}$$

In this example, there are no equilibrated surface reactions. If there were any, the same procedure as that applied for reducing the number of material balances would be applied.

List of Symbols

c_i Concentration of species i ($\mathrm{mol/m^3}$)

$c^0_{\mathrm{H^+}}$ Bulk concentration of protons ($\mathrm{mol/m^3}$)

D_i Diffusion coefficient of species i ($\mathrm{m^2/s}$)

F Faraday's constant (96,487 C/mol)

i_{CER} Current density for CO evolution reaction ($\mathrm{A/m^2}$)

$i_{\mathrm{H_2,lim}}$ Limiting current density for H_2 evolution reaction ($\mathrm{A/m^2}$)

k_{CER} Rate constant for CO evolution reaction (m/s)

$k_{f,k}$ Forward rate constant of reaction k (units depend on reaction; see table 3.2)

K_k Equilibrium constant of reaction k (units depend on reaction; see table 3.1)

M_i Symbol for the chemical formula of species i

n_{ads} Number of adsorbed species on the electrode surface (including empty sites)

$\mathbf{N}_i$ Flux density of species i ($\mathrm{mol/m^2\ s}$)

n_k Number of electrons exchanged in electrochemical reaction k

n_h Number of homogeneous reactions

n_{h_e} Number of independent equilibrated homogeneous reactions

n_s Number of surface reactions

n_{s_e} Number of independent equilibrated surface reactions

n_{sol} Number of soluble species

p_i Partial pressure of species i (bar)

R Ideal-gas constant (8.314 J/mol K)

R_k Rate of reaction k ($\mathrm{mol/m^3\ s}$ for homogeneous reactions and $\mathrm{mol/m^2\ s}$ for surface reactions)

$s_{i,k}$	Stoichiometric coefficient of species i in reaction k
T	Temperature (K)
V	Electrode potential vs. a specified reference electrode (V)
x	Distance from electrode surface (m)
x_{RE}	Distance between the working electrode surface and the reference electrode (m)
z_i	Charge of species i
β_{CER}	Charge transfer coefficient of CO evolution reaction
β_k	Charge transfer coefficient of electrochemical reaction k
δ	Thickness of the Nernst layer (m)
Γ_{max}	total surface concentration of sites at the electrode ($\mathrm{mol/m^2}$)
Φ_1	Electric potential of the metal of the electrode (V)
Φ_2	Electric potential of the liquid phase (V)
θ_i	fractional surface coverage of adsorbed species (or empty site) i

Chapter 4

Mathematical modeling of an electrolysis cell making syngas ($CO + H_2$) from CO_2 and H_2O reduction at room temperature

4.1 Introduction

In chapter 1, several cell designs for making syngas from CO_2 and H_2O at room temperature have been studied. The best design we came up with involves the use of an aqueous buffer layer (BL) of potassium bicarbonate between the gas-diffusion cathode and the cation-exchange membrane, which is displayed in figure 4.1.

If we make the assumption that acid-base reactions are equilibrated, the overall reactions for CO and H_2 evolution at the cathode are written as

$$3CO_2 + H_2O + 2e^- \rightarrow CO + 2HCO_3^-, \tag{4.1}$$

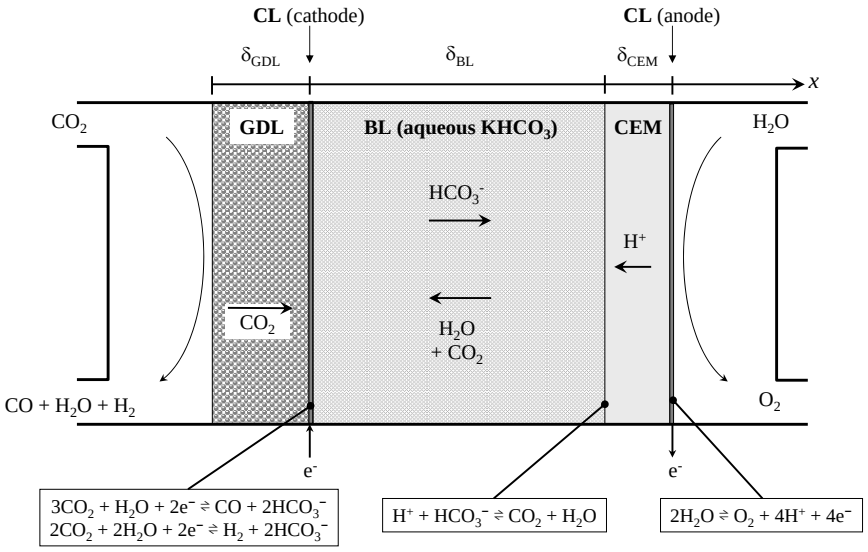

Figure 4.1: Schematics of the electrolysis cell based on a gas-diffusion cathode for syngas production from reduction of CO_2 and H_2O.

and

$$2CO_2 + 2H_2O + 2e^- \rightarrow H_2 + 2HCO_3^-. \tag{4.2}$$

Oxygen evolution at the anode is written as

$$2H_2O \rightarrow O_2 + 4H^+ + 4e^-, \tag{4.3}$$

and generates protons that are transported through the cation-exchange membrane toward the cathode. At the boundary between the BL and the cation-exchange membrane, the protons react with the bicarbonate ions coming from the cathode according to

$$H^+ + HCO_3^- \rightleftharpoons CO_2 + H_2O. \tag{4.4}$$

This design was shown to be selective for CO_2 reduction to CO, with a current efficiency of ca. 85% when silver is used as the cathode catalyst, as recalled in figure 4.2. We also stressed that strong acidic conditions are responsible for the high selectivity of the fuel-cell-

like setup toward hydrogen evolution, in good agreement with previous reports from the literature where designs similar to a proton-exchange-membrane fuel cell (PEMFC) were studied with various metal catalysts at the cathode.[15–17] This conclusion is emphasized in figure 4.2, which shows that only H_2 is evolved when a solution of hydrochloric acid is used instead of potassium bicarbonate in the BL.

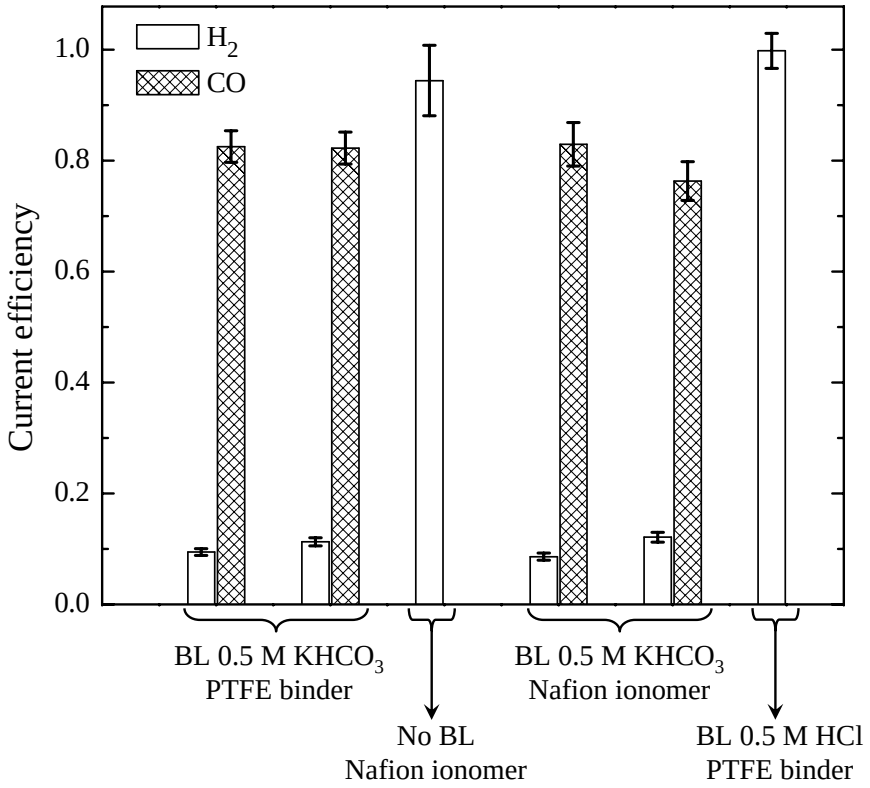

Figure 4.2: Current efficiencies of H_2 and CO at 15 min electrolysis (-20 mA/cm^2) with Ag-based GDEs using different conditions of buffer layer and binders in the catalyst layer. Duplicates are shown for two of the systems. BL: buffer layer.

In this chapter, we follow up on studying the BL-type cell with silver-based gas-diffusion cathodes, by looking at the influence of several cell parameters, i.e., the current density, the salt concentration in the BL, the CO_2 partial pressure, and the electrolysis duration. Cathodes based on gold are also studied and compared to the results obtained with silver. A mathematical model of the cell is presented and used to get more insight into the cell be-

havior and the limitations of this design. This model builds upon another one developed in chapter 3. It is a generic steady-state model of a Nernst layer of defined thickness adjacent to an electrode where several parallel electrochemical reactions, possibly coupled with homogeneous chemical reactions, can readily be accounted for, and these reactions can either have a finite rate constant or be assumed equilibrated. This model was used for studying the kinetics of CO_2 reduction to CO (CER) and H_2O reduction to H_2 (HER) on flat gold and silver electrodes in an aqueous electrolyte.

The outline of the chapter is the following: After a short experimental section, the mathematical model of the complete electrolysis cell (BL-type cell) is developed in a second section. As a preamble, a general framework for treating equilibrated reactions and equilibrated interfacial mass transfer between phases is set forth, and comes as a extension of what was presented in chapter 3. A third section presents various experimental results obtained with the BL-type cell, and these results are analyzed using the model and discussed. Some kinetic parameters for CER and HER that were adjusted from data on flat metal electrodes in chapter 3, are used as input parameters herein. Finally, the behavior of a cell design using a porous anion-exchange membrane (AEM) layer instead of the present buffer layer is simulated, so as to get a feel on the maximum performance such a design could achieve.

4.2 Experimental

The BL-type cell was extensively described in chapter 1 and hence the readers are invited to refer to the experimental section of this chapter for details on the experimental setup as well as on how to prepare the membrane electrode assemblies (MEAs).

4.3 Mathematical model

4.3.1 Main assumptions used in the model

The model is for isothermal operation (25 °C).

The electrolysis cell is composed of several layers, including a cathode gas-diffusion layer (GDL), a cathode catalyst layer (CL), a pH BL, a cation-exchange membrane (CEM), and an anode CL. For the sake of simplicity, both cathode and anode CLs are assumed to have a zero thickness. This is a fairly reasonable assumption since CLs are prepared either by direct painting or by decal transfer, from a mixture with no added carbon. (See experimental section of chapter 1) for more details.) Therefore, three layers are considered, namely the cathode GDL, the BL, and the CEM, as schematized in figure 4.1.

Because of reaction 4.4 at the boundary between the BL and the membrane, CO_2 is formed. Except perhaps at low current density,[†] the CO_2 reaches its maximum of solubility and bubbles off the solution as a gas. Thus, the BL is likely composed of a solid (inert glass-fiber mat), a liquid (aqueous potassium bicarbonate solution), and a gas phase (mixture of CO_2, H_2O, CO, H_2, and Ar whenever experiments under various CO_2 partial pressures are performed). The volume fraction of the solid component is estimated to be 7% from the thickness of the BL ($\delta_{BL} = 800$ μm), the density of silica (ca. 2.2 g/cm^3), and the specific weight of the mat used (Whatman GF/D, 12.1 mg/cm^2). However, the volume fractions of liquid and gas phases are not straightforward to determine, and furthermore are prone to vary with operating conditions such as the current density. Unless otherwise stated, the gas-phase volume fraction is set to a very low value (i.e., 1%) in the following, which is likely representative of low-current-density operation. A sensitivity analysis of the relative gas/liquid volume fractions in the BL is performed in the following. A uniform presure is assumed for the gas phase across the cell.

[†]Throughout this chapter, we refer to current densities and overpotentials in magnitude, i.e., we refer to them as positive quantities although they are negative for a cathodic reaction.

Most of the assumptions used and detailed in chapter 3 are still valid herein: The rate-determining steps for CO_2 reduction to CO and H_2O reduction to H_2 are assumed to be the formation of $CO^{\bullet-}_{2(ads)}$ and $H^{\bullet}_{(ads)}$ radicals, respectively (reactions 3.1 and 3.3), and Tafel-like expressions are used as kinetic equations. Acid-base homogeneous reactions in the liquid phase of the BL are assumed equilibrated, i.e., they have infinite rate constants. The concentration of H_2CO_3 is so low in the liquid phase that it is neglected, as are those for CO and H_2 because of their low solubilities in aqueous electrolytes. Because CO_2 and H_2O mass transfer at the gas/liquid interface is very fast,[79] it is assumed that CO_2 and H_2O are equilibrated between the phases. No homogeneous reaction is considered within the gas phase; even though the water-gas shift reaction is thermodynamically feasible in the experimental conditions we used, the reaction is so slow that it can be neglected. Finally, water mass transfer and the ion-exchange reaction between H^+ and K^+ at the BL/membrane boundary (and water mass transfer at the membrane/anode CL boundary) are assumed equilibrated.

Even though there is a net water (or electrolyte) flux from the anode to the cathode because of electro-osmotic effects in the membrane, only a solid and a gas phase are considered in the cathode GDL, for simplicity. Possible flooding of the GDL is simply accounted for by a decrease of the gas volume fraction in the GDL, as discussed later on. The solid phase is basically a mixture of carbon and polytetrafluoroethylene (PTFE) and conducts electrons from the current collector ribs toward the cathode CL where the reduction of CO_2 and H_2O occurs.

Finally, no gas composition variations along the gas channel are considered. This assumption is reasonably valid given the large gas flow rate (20 mL/min), the small geometric area of the MEAs (1 cm^2), and the relatively low current density values, as compared for example with those used for proton-exchange-membrane fuel cells, which are usually about an order of magnitude higher.

4.3.2 Equilibrated reactions and equilibrated interfacial mass transfer in a multiphase medium

Because the electrochemical system studied here is rather complex, some of the assumptions are that some homogeneous reactions, heterogeneous reactions, and mass transfer of some species at the interface between two phases (mass transfer is denoted as "reaction" as well in the following, for simplicity) are equilibrated. Therefore, as a preamble, the general framework required for handling equilibrated reactions in a multiphase system is developed. The set of material balances for a medium composed of n_p phases is provided. Boundary conditions suitable at a boundary where n_p phases are present are also detailed.

Material balances

In a medium composed of n_p phases, with each of these phases composed of n_{s_p} species, $n_p n_{s_p}$ material balances can be written. A general form of the material balance of a species i in phase p at steady state reads

$$\nabla \cdot \mathbf{N}_{i,p} = \sum_{k=1}^{n_r} s_{i,k} \mathcal{R}_k, \tag{4.5}$$

where $\mathbf{N}_{i,p}$ is the flux density of species i in phase p and n_r is the total number of reactions (including interfacial mass transfer) considered. For reaction k defined by the general equation 3.8, $s_{i,k}$ is the stoichiometric coefficient of species i, and $\mathcal{R}_k$ is related to the rate of reaction k, R_k. One has $\mathcal{R}_k = a_{p-q} R_k$ for heterogeneous reactions between phases p and q, with a_{p-q} the area of interface between phases p and q per unit volume, and $\mathcal{R}_k = \epsilon_p R_k$ for homogeneous reactions within phase p, with ϵ_p the volume fraction of phase p. For reactions having a finite rate constant, the general kinetic expression 3.9 can directly substitute for R_k.

If some of the reactions (either homogeneous or heterogeneous at the interface between two phases) are considered equilibrated, some of the material balances are replaced by n_{r_e} equilibrium relationships of the independent equilibrated reactions. The $n_p n_{s_p} - n_{r_e}$ remaining material balances to be used are obtained using a similar methodology as that explained in chapter 3 to eliminate the reaction rates of the equilibrated reactions.

Transport equations

In chapter 3, dilute solution theory was used to describe transport of soluble species in the liquid phase, and Nernst-Planck equations (Eq. 3.12) were used to substitute for the fluxes in the material balances. This means that the fluxes were not retained as unknowns and were not explicitly determined. When using multicomponent diffusion equations, such a substitution is not readily possible, and fluxes are retained as explicit unknowns. In either case, the set of transport equations to be solved must be modified whenever some reactions are assumed equilibrated. This is done in the following for both dilute and concentrated solutions.

When using dilute solution theory, the flux density $\mathbf{N}_{i,p}$ of a species i in phase p reads

$$\mathbf{N}_{i,p} = -z_i \frac{\epsilon_p^{1.5} D_{i,p}}{RT} F c_{i,p} \nabla \Phi_2 - \epsilon_p^{1.5} D_{i,p} \nabla c_{i,p} + c_{i,p} \mathbf{v}_p, \tag{4.6}$$

where z_i is the charge number of species i, $D_{i,p}$ and $c_{i,p}$ stand for the diffusion coefficient and the concentration of species i in phase p, respectively, Φ_2 is the electric potential in phase p, and $\mathbf{v}_p$ is the superficial fluid velocity within the phase. F, R, and T are Faraday's constant, the ideal-gas constant, and the temperature, respectively. This flux expression was derived assuming the Bruggeman correction for the effective diffusion coefficients, i.e., $D_{i,p}^{\text{eff}} = \epsilon_p^{0.5} D_{i,p}$. As far as a gas phase (assumed ideal) is concerned, $c_{i,p}$ can be replaced by $p_{i,p}/RT$, with $p_{i,p}$ the partial pressure of gaseous species i in phase p.

When using concentrated solution theory, multicomponent diffusion equations are considered, and read

$$c_{i,p}\nabla\mu_{i,p} = RT\sum_{j\neq i}\frac{c_{i,p}\mathbf{N}_{j,p} - c_{j,p}\mathbf{N}_{i,p}}{c_{T,p}\epsilon_p^{1.5}\mathscr{D}_{ij,p}}, \tag{4.7}$$

where $c_{T,p}$ stands for the sum of concentrations of species in phase p and $\mathscr{D}_{ij,p}$ is the binary diffusion coefficient between species i and j in phase p. Like for the dilute solution theory, the Bruggeman correction was assumed ($\mathscr{D}_{ij,p}^{\text{eff}} = \epsilon_p^{0.5}\mathscr{D}_{ij,p}$). The gradient of electrochemical potential of species i at uniform pressure and temperature is expressed as

$$\nabla\mu_{i,p} = z_i F\nabla\Phi_2 + RT\frac{\nabla x_{i,p}}{x_{i,p}} + RT\nabla(\ln\Gamma_i - \frac{z_i}{z_n}\ln\Gamma_n), \tag{4.8}$$

where $x_{i,p}$ is the mole fraction of species i in phase p, that is, $x_{i,p} = c_{i,p}/c_{T,p}$, and Γ_i is the activity coefficient of species i. The electric potential Φ_2 is defined using the quasi-electrostatic potential with a specified reference species n. When p is a gas phase, assumed ideal, $c_{i,p}\nabla\mu_{i,p}$ simplifies to $\nabla p_{i,p}$ in Eq. 4.7. Because of the Gibbs-Duhem relationship, only $n_{s_p} - 1$ multicomponent diffusion equations are independent. Instead, the n_{s_p}th equation is

$$\sum_i x_{i,p} = 1. \tag{4.9}$$

For an electrolytic solution, the electroneutrality equation,

$$\sum_i z_i c_{i,p} = 0, \tag{4.10}$$

is also used. This implies that electric double layers can be treated as part of an interface.

When an equilibrated reaction k is taken into account, the equilibrium relationship (Eq. 3.10) can be expressed in a more general form as a function of the electrochemical potentials $\mu_{i,p}$ of species i in phase p.

$$\sum_i s_{i,k}\mu_{i,p} = 0. \tag{4.11}$$

Differentiation of Eq. 4.11 suggests an algebraic relationship among the driving forces $\mathbf{d}_{i,p} = c_{i,p}\nabla\mu_{i,p}$ of the species involved in an equilibrated reaction

$$\sum_i s_{i,k}\frac{\mathbf{d}_{i,p}}{c_{i,p}} = 0. \tag{4.12}$$

As a consequence, n_{r_e} transport equations (used as governing equations) have to be replaced by algebraic equations of the form of Eq. 4.12, in which the driving forces $\mathbf{d}_{i,p}$ are substituted for

$$\mathbf{d}_{i,p} = \left(c_{i,p}\mathbf{v}_p - \mathbf{N}_{i,p}\right)\frac{RT}{\epsilon_p^{1.5}D_{i,p}}, \tag{4.13}$$

whenever dilute solution theory is used to describe transport in phase p, or as

$$\mathbf{d}_{i,p} = RT\sum_{j\neq i}\frac{c_{i,p}\mathbf{N}_{j,p} - c_{j,p}\mathbf{N}_{i,p}}{c_{T,p}\epsilon_p^{1.5}\mathscr{D}_{ij,p}}, \tag{4.14}$$

whenever concentrated solution theory is used. Because Eq. 4.12 is algebraic, it remains valid at the boundaries of the domain. The transport equations that are removed from the set of governing equations and replaced by algebraic equations 4.12 must refer to species that are involved in an equilibrated reaction in order for the set of governing equations to be consistent.

Flux continuity boundary equations

Like for the material balances, we wish to derive proper flux relationships in the presence of equilibrated reactions at a boundary where several phases coexist. A general flux continuity equation at steady state for a boundary located at position x is written as

$$N_{i,p}|_{x^+} - N_{i,p}|_{x^-} = -\sum_{k=1}^{n_r^b} s_{i,k}\mathcal{R}_k^b, \tag{4.15}$$

where $N_{i,p}|_{x^-}$ and $N_{i,p}|_{x^+}$ denote the fluxes of species i in phase p at x^- and x^+, respectively, and the other variables and parameters have the same definition as in Eq. 4.5 but the superscript b is added for "boundary." One has $\mathcal{R}_k^b = a_{p-q}^b R_k^b$ for heterogeneous reactions between phases p and q, with a_{p-q}^b the area of interface between the phases p and q per cross sectional area of the boundary. As in Eq. 4.5, for reactions having a finite rate constant, R_k^b is substituted by the general kinetic expression 3.9 in the flux continuity equation (Eq. 4.15).

When some reactions at a boundary are considered equilibrated, some of the flux continuity equations have to be replaced by the equilibrium relationships (Eq. 3.10) of the $n_{r_e}^b$ independent equilibrated reactions. This applies to all kinds of equilibrated reactions, including homogeneous reactions, as discussed in chapter 3. Again, the same procedure is used to eliminate the rates of the equilibrated reactions in the remaining $n_p n_{s_p} - n_{r_e}^b$ flux continuity equations to be considered as boundary conditions.

4.3.3 Governing equations for the electrolysis cell

Buffer layer

Let us apply the general methodology developed above to the buffer layer, for which the liquid and the gas phases are treated using dilute and concentrated solution theories, respectively. In the liquid phase (aqueous potassium bicarbonate), there are 6 solutes ($H_{(l)}^+$, $OH_{(l)}^-$, $K_{(l)}^+$, $CO_{2(l)}$, $HCO_{3(l)}^-$, and $CO_{3(l)}^{2-}$) and 3 equilibrated acid-base reactions (reactions 3.5,3.6, and 3.7) among those species. Unlike the solvent concentration ($c_{H_2O,l}$), the solvent flux is considered as an unknown because it is used to approximate the superficial fluid velocity of the liquid phase, according to

$$\mathbf{v}_l = \overline{V}_{H_2O,l} \mathbf{N}_{H_2O,l}, \tag{4.16}$$

where $\overline{V}_{H_2O,l}$ is the partial molar volume of water in the liquid phase, which is taken equal to that of pure water, for convenience. In the gas phase, there are 4 species ($CO_{2(g)}$, $H_{2(g)}$, $CO_{(g)}$, and $H_2O_{(g)}$) plus $Ar_{(g)}$ whenever $CO_{2(g)}$ partial pressure in the cathode gas channel is varied. The binary diffusion coefficient $\mathscr{D}_{ij,g}$, used in the Stefan-Maxwell equations (Eq. 4.7) are calculated using equation 4.54 provided in Appendix 4.6.1. No homogeneous reaction in the gas phase is considered, as discussed previously. CO_2 and H_2O mass transfer at the interface between gas and liquid phases is assumed equilibrated.

For the two phases altogether, this gives a total of 24 variables to be solved (i.e., concentrations for the 6 soluble species, partial pressures for the 5 gaseous species, fluxes for the 11 soluble and gaseous species, the liquid-water flux, and the potential Φ_2). Now, let us detail the governing equations: 5 equations are the equilibrium relationships (Eq. 3.10) applied to the three equilibrated acid-base reactions and gas-liquid interfacial mass transfer for CO_2 and H_2O. There are 4 regular material balances (Eq. 4.5) for $H_{2(g)}$, $CO_{(g)}$, $Ar_{(g)}$, and $K^+_{(l)}$, which simply read

$$\nabla \cdot \mathbf{N}_{i,p} = 0, \tag{4.17}$$

because those species are not involved in any reaction within the BL. The remaining 2 material balances are obtained using the methodology detailed above and read

$$\nabla \cdot \mathbf{N}_{H^+,l} - \nabla \cdot \mathbf{N}_{OH^-,l} - \nabla \cdot \mathbf{N}_{HCO_3^-,l} - 2\nabla \cdot \mathbf{N}_{CO_3^{2-},l} = 0, \tag{4.18}$$

and

$$\nabla \cdot \mathbf{N}_{CO_2,l} + \nabla \cdot \mathbf{N}_{HCO_3^-,l} + \nabla \cdot \mathbf{N}_{CO_3^{2-},l} + \nabla \cdot \mathbf{N}_{CO_2,g} = 0. \tag{4.19}$$

Note that Eq. 4.18 corresponds to a current balance ($\sum_i z_i \nabla \cdot \mathbf{N}_{i,p} = 0$) while Eq. 4.19 is a carbon balance in the overall layer. 5 equations are the driving-force relationships (Eq. 4.12) applied to the 5 equilibrated reactions. Note that $\mathbf{d}_{H_2O,l} = 0$ because no gradient of chemical potential of liquid water is expected (dilute solution theory is used for the liquid phase). The 5 transport equations to be considered as governing equations are such that they apply

to species that are independent of each other (i.e., there is no relation between these species such as an equilibrated reaction or Gibbs-Duhem equation). Therefore, 2 Stefan-Maxwell equations necessarily apply to either $CO_{(g)}$, $H_{2(g)}$, or $Ar_{(g)}$ (Eq. 4.7) and a Nernst-Planck equation necessarily applies to $K^+_{(l)}$ (Eq. 4.6). There are several possibilities for the choice of the remaining 2 transport equations (e.g., $CO_{2(l)}$ and $H^+_{(l)}$). Finally, the remaining 3 equations are Eq. 4.9 applied to the gas phase, electroneutrality (Eq. 4.10), and a material balance equation for liquid water (used for the convective part of the Nernst-Planck equations only, see Eq. 4.16)

$$\nabla \cdot \mathbf{N}_{H_2O,l} + \nabla \cdot \mathbf{N}_{H^+,l} - \nabla \cdot \mathbf{N}_{CO_3^{2-},l} + \nabla \cdot \mathbf{N}_{H_2O,g} = 0. \tag{4.20}$$

Gas-diffusion layer

In the GDL, the set of governing equations is much simpler because of the assumption that there is no liquid phase. In the gas phase, composed of the same 5 gaseous species as in the BL, there are 5 material balances (Eq. 4.17), 4 Stefan-Maxwell equations (Eq. 4.7), and Eq. 4.9 to be considered. Furthermore, the electronic transport in the solid phase is accounted for by means of Ohm's law

$$\mathbf{i} = -\sigma_1 \epsilon_s^{1.5} \nabla \Phi_1, \tag{4.21}$$

where $\mathbf{i}$ is the total current density, σ_1 is the electronic conductivity of the solid phase, ϵ_s is the volume fraction of the solid phase in the GDL, and Φ_1 is the potential of the solid phase.

Cation-exchange membrane

Finally, the governing equations in the membrane phase are presented. Like for the gas phase, multicomponent-diffusion equations are used. A peculiarity of this electrolysis cell is that although the cation-exchange membrane is fully in the potassium form at zero current, it contains both protons and potassium upon operation. The governing equations for a

membrane containing two cations were described extensively in chapter 2 and the transport properties were determined from experimental data reported in the literature. Basically, the membrane is composed of 4 species, i.e., $H^+_{(m)}$, $K^+_{(m)}$, $H_2O_{(m)}$, and $M^-_{(m)}$; therefore 3 multicomponent diffusion equations (out of 4) are used (Eq. 4.7), e.g., for $H^+_{(m)}$, $K^+_{(m)}$, and $H_2O_{(m)}$, where ϵ_m is set to unity and where the flux of $M^-_{(m)}$ is set to zero as expected for a steady state. The gradients of electrochemical potential are substituted by

$$\nabla\mu_{H^+,m} = RT\frac{\nabla x_{H^+,m}}{x_{H^+,m}} + F\nabla\Phi_2, \tag{4.22}$$

$$\nabla\mu_{K^+,m} = RT\frac{\nabla x_{K^+,m}}{x_{K^+,m}} + b\left(\nabla\left(y^2_{HM}\right) - \nabla\left(y^2_{KM}\right)\right) + F\nabla\Phi_2, \tag{4.23}$$

and

$$\nabla\mu_{H_2O,m} = RT\frac{\nabla x_{H_2O,m}}{x_{H_2O,m}}, \tag{4.24}$$

where $y_{HM} = x_{H^+,m}/(x_{H^+,m} + x_{K^+,m})$ and $y_{KM} = 1 - y_{HM}$, and b is a constant term due to nonideality. Eq. 4.22 and 4.23 differ from those in chapter 2 because of a different potential definition: in this chapter, Φ_2 is the quasi-electrostatic potential with $H^+_{(m)}$ as reference species, whereas Φ_2 was defined as the potential referred to a hydrogen electrode in chapter 2. This is to be consistent with the potential definition in the BL. Other governing equations encompass 3 material balances for $H^+_{(m)}$, $K^+_{(m)}$, and $H_2O_{(m)}$ (Eq. 4.17), the electroneutrality (Eq. 4.10), and Eq. 4.9.

To account for membrane swelling, two equations are added to the set of governing equations to be solved in the membrane. Since the concentration of membrane can vary across the system but the thickness is constant, one solves for the thickness by using the equations

$$\frac{\partial\delta_{CEM}}{\partial x} = 0, \tag{4.25}$$

and

$$\frac{\partial\eta_{M^-}}{\partial x} = c_{M^-,m}, \tag{4.26}$$

where η_{M^-} is the integral number of moles of membrane M^- per cross sectional area.

The total number of moles of potassium per cross sectional area is known, but we do not know how K^+ is distributed in the BL and the membrane. Therefore, we need to add one more governing equation in both layers

$$\frac{\partial \eta_{K^+}}{\partial x} = \epsilon_p c_{K^+,p}, \tag{4.27}$$

where η_{K^+} is the integral number of moles of K^+ per cross sectional area. For the membrane, $\epsilon_m = 1$.

4.3.4 Boundary conditions

Cathode gas channel

At the cathode gas channel, partial pressures for gaseous species are set. Because the total pressure is set, only 4 partial pressures out of 5 are set.

Cathode catalyst layer

At the cathode CL (boundary between cathode GDL and BL), if no equilibrated reactions are considered, one needs 5 and 4 continuity equations for fluxes and partial pressures of gaseous species, respectively, 6 flux conditions for soluble species in the liquid phase of the BL, and 3 equations for the 2 species adsorbed at the surface of the catalyst particles ($H^{\bullet}_{(ads)}$, $CO^{\bullet -}_{2(ads)}$) and the empty sites. For $CO_{(g)}$, $H_{2(g)}$, and $Ar_{(g)}$, these flux continuity equations

simply read

$$N_{\mathrm{CO},g}|_{x=\delta_{\mathrm{GDL}}^{+}} - N_{\mathrm{CO},g}|_{x=\delta_{\mathrm{GDL}}^{-}} = \mathcal{R}_{\mathrm{CER},2}, \tag{4.28}$$

$$N_{\mathrm{H_2},g}|_{x=\delta_{\mathrm{GDL}}^{+}} - N_{\mathrm{H_2},g}|_{x=\delta_{\mathrm{GDL}}^{-}} = \mathcal{R}_{\mathrm{HER},2}, \tag{4.29}$$

and

$$N_{\mathrm{Ar},g}|_{x=\delta_{\mathrm{GDL}}^{+}} - N_{\mathrm{Ar},g}|_{x=\delta_{\mathrm{GDL}}^{-}} = 0, \tag{4.30}$$

respectively. $\mathcal{R}_{\mathrm{CER},2}$ and $\mathcal{R}_{\mathrm{HER},2}$ stand for the rates of the elementary steps for $\mathrm{CO_{(g)}}$ and $\mathrm{H_{2(g)}}$ evolution, respectively (Reactions 3.2 and 3.4). For $\mathrm{K^{+}_{(l)}}$ cations, the flux at $(\delta_{\mathrm{GDL}})^{+}$ is set to zero

$$N_{\mathrm{K^{+}},l}|_{x=\delta_{\mathrm{GDL}}^{+}} = 0. \tag{4.31}$$

Material balances for adsorbed species ($\mathrm{CO^{\bullet -}_{2(ads)}}$ and $\mathrm{H^{\bullet}_{(ads)}}$) are also derived from Eq. 4.15, where fluxes in $\delta_{\mathrm{GDL}}^{+}$ and $\delta_{\mathrm{GDL}}^{-}$ are set to zero, and read

$$\mathcal{R}_{\mathrm{CER},1} = \mathcal{R}_{\mathrm{CER},2}, \tag{4.32}$$

and

$$\mathcal{R}_{\mathrm{HER},1} = \mathcal{R}_{\mathrm{HER},2}, \tag{4.33}$$

with $\mathcal{R}_{\mathrm{CER},1}$ and $\mathcal{R}_{\mathrm{HER},1}$ the rates of the elementary steps for $\mathrm{CO^{\bullet -}_{2(ads)}}$ and $\mathrm{H^{\bullet}_{(ads)}}$ formation, respectively (Reactions 3.1 and 3.3). The last equation for adsorbed species is simply a balance on site fractions

$$\theta_{\mathrm{CO_2^{\bullet -}}} + \theta_{\mathrm{H^{\bullet}}} + \theta_{\square} = 1, \tag{4.34}$$

with θ_i the site fraction of adsorbed species i and $\theta_{\square}$ the fraction of empty sites. Because there are 5 equilibrated reactions, 5 flux conditions for either gaseous or soluble species are taken out and replaced by 5 equilibrium relationships. There are 2 resulting flux conditions

that are expressed as

$$N_{\mathrm{OH}^-,l}\big|_{x=\delta^+_{\mathrm{GDL}}} - N_{\mathrm{H}^+,l}\big|_{x=\delta^+_{\mathrm{GDL}}} + 2\, N_{\mathrm{CO}_3^{2-},l}\Big|_{x=\delta^+_{\mathrm{GDL}}} + N_{\mathrm{HCO}_3^-,l}\Big|_{x=\delta^+_{\mathrm{GDL}}} - 2(\mathcal{R}_{\mathrm{CER},1} + \mathcal{R}_{\mathrm{HER},1}) = 0, \tag{4.35}$$

and

$$N_{\mathrm{CO}_2,l}\big|_{x=\delta^+_{\mathrm{GDL}}} + N_{\mathrm{CO}_3^{2-},l}\Big|_{x=\delta^+_{\mathrm{GDL}}} + N_{\mathrm{HCO}_3^-,l}\Big|_{x=\delta^+_{\mathrm{GDL}}} + N_{\mathrm{CO}_2,g}\big|_{x=\delta^+_{\mathrm{GDL}}} - N_{\mathrm{CO}_2,g}\big|_{x=\delta^-_{\mathrm{GDL}}} + \mathcal{R}_{\mathrm{CER},1} = 0. \tag{4.36}$$

Finally, a last condition is the current conservation equation

$$i = -2F(\mathcal{R}_{\mathrm{CER},1} + \mathcal{R}_{\mathrm{HER},1}). \tag{4.37}$$

Buffer layer/membrane boundary

At the BL/membrane boundary, there is the juxtaposition of three phases: a gas phase and a liquid phase containing 5 and 6 species in the BL, respectively, and a membrane phase containing 4 species. Therefore, 15 conditions are needed, consisting in both flux conditions and equilibrium relationships of equilibrated reactions, plus a condition for liquid-water flux (because it is used in the convection term of Eq. 4.6). Beside the same 5 reactions assumed equilibrated in the BL, additional interfacial mass transfer of protons and potassium cations between the liquid and the membrane phases, as well as interfacial mass transfer of water between the liquid/gas phase and the membrane phase, are considered. It is reasonable to assume all are equilibrated. Although there are 3 independent interfacial mass-transfer relationships involving membrane species, only two equilibrium relationships hold because H^+ and K^+ mass transfer is not independent by virtue of current continuity. As detailed in chapter 2, the following 2 equilibrium relationships read

$$K_{\mathrm{IER}} = \frac{f_{\mathrm{HM}} y_{\mathrm{HM}} c_{\mathrm{K}^+,l}}{f_{\mathrm{KM}} y_{\mathrm{KM}} c_{\mathrm{H}^+,l}}, \tag{4.38}$$

and

$$\lambda = \frac{x_{\mathrm{H_2O},m}}{x_{\mathrm{M^-},m}} = -3.9578 y_{\mathrm{HM}}^4 + 8.5846 y_{\mathrm{HM}}^3 - 10.087 y_{\mathrm{HM}}^2 + 13.526 y_{\mathrm{HM}} + 13.227, \tag{4.39}$$

where K_{IER} is the equilibrium constant of the ion-exchange reaction

$$\mathrm{H^+_{(l)}} + \mathrm{K^+_{(m)}} \rightleftharpoons \mathrm{H^+_{(m)}} + \mathrm{K^+_{(l)}}, \tag{4.40}$$

and f_i is the activity coefficient of component i in the membrane that is assumed to behave as a regular mixture of HM and KM, and is expressed as

$$f_{\mathrm{KM}} = f_{\mathrm{K^+}} f_{\mathrm{M^-}} = \exp(\tfrac{b}{RT} y_{\mathrm{HM}}^2) \quad \text{and} \quad f_{\mathrm{HM}} = f_{\mathrm{H^+}} f_{\mathrm{M^-}} = \exp(\tfrac{b}{RT} y_{\mathrm{KM}}^2). \tag{4.41}$$

In Eq. 4.38, activity coefficients for $\mathrm{H^+_{(l)}}$ and $\mathrm{K^+_{(l)}}$ are set to unity, in agreement with the dilute solution approximation. Eq. 4.39 is an empirical polynomial relationship between the water content in the membrane λ and the fraction of protons y_{HM}, which was deduced from experimental data, as explained in chapter 2. Because of a total of 8 equilibrated reactions, 7 flux conditions are required (plus that on liquid-water flux). Fluxes for $\mathrm{CO_{(g)}}$, $\mathrm{H_{2(g)}}$, and $\mathrm{Ar_{(g)}}$ are simply set to zero

$$N_{i,g}|_{x=(\delta_{\mathrm{GDL}}+\delta_{\mathrm{BL}})^-} = 0. \tag{4.42}$$

As mentioned above, the flux of $\mathrm{M^-_{(m)}}$ is zero throughout the entire membrane. The other flux conditions, obtained by eliminating the rates of equilibrated reactions/equilibrated interfacial mass transfer using the methodology detailed in chapter 3, read

$$\begin{aligned} N_{\mathrm{OH^-},l}\big|_{x=(\delta_{\mathrm{GDL}}+\delta_{\mathrm{BL}})^-} - N_{\mathrm{H^+},l}|_{x=(\delta_{\mathrm{GDL}}+\delta_{\mathrm{BL}})^-} + 2\, N_{\mathrm{CO_3^{2-}},l}\Big|_{x=(\delta_{\mathrm{GDL}}+\delta_{\mathrm{BL}})^-} \\ + N_{\mathrm{HCO_3^-},l}\Big|_{x=(\delta_{\mathrm{GDL}}+\delta_{\mathrm{BL}})^-} + N_{\mathrm{H^+},m}|_{x=(\delta_{\mathrm{GDL}}+\delta_{\mathrm{BL}})^+} = 0, \end{aligned} \tag{4.43}$$

$$N_{\mathrm{K^+},l}|_{x=(\delta_{\mathrm{GDL}}+\delta_{\mathrm{BL}})^-} - N_{\mathrm{K^+},m}|_{x=(\delta_{\mathrm{GDL}}+\delta_{\mathrm{BL}})^+} = 0, \tag{4.44}$$

$$N_{\mathrm{CO_2},l}\big|_{x=(\delta_{\mathrm{GDL}}+\delta_{\mathrm{BL}})^-}+N_{\mathrm{CO_3^{2-}},l}\Big|_{x=(\delta_{\mathrm{GDL}}+\delta_{\mathrm{BL}})^-}+N_{\mathrm{HCO_3^-},l}\Big|_{x=(\delta_{\mathrm{GDL}}+\delta_{\mathrm{BL}})^-}+N_{\mathrm{CO_2},g}\big|_{x=(\delta_{\mathrm{GDL}}+\delta_{\mathrm{BL}})^-}=0, \tag{4.45}$$

and

$$\begin{aligned} &N_{\mathrm{H_2O},l}\big|_{x=(\delta_{\mathrm{GDL}}+\delta_{\mathrm{BL}})^-}+N_{\mathrm{H^+},l}\big|_{x=(\delta_{\mathrm{GDL}}+\delta_{\mathrm{BL}})^-}-N_{\mathrm{H^+},m}\big|_{x=(\delta_{\mathrm{GDL}}+\delta_{\mathrm{BL}})^+} \\ &-N_{\mathrm{CO_3^{2-}},l}\Big|_{x=(\delta_{\mathrm{GDL}}+\delta_{\mathrm{BL}})^-}+N_{\mathrm{H_2O},g}\big|_{x=(\delta_{\mathrm{GDL}}+\delta_{\mathrm{BL}})^-}-N_{\mathrm{H_2O},m}\big|_{x=(\delta_{\mathrm{GDL}}+\delta_{\mathrm{BL}})^+}=0. \end{aligned} \tag{4.46}$$

This last flux condition is because one solves for the liquid-water flux (i.e., the fluid velocity, through Eq. 4.16) in the buffer layer. The integral number of moles of membrane M^- per cross sectional area, η_{M^-}, is set to zero. Finally, there is a relationship between the potential in the liquid phase and that in the membrane, which is deduced from $\mu_{\mathrm{H^+,l}}=\mu_{\mathrm{H^+,m}}$, and reads

$$[RT\ln c_{\mathrm{H^+,l}}+F\Phi_2]|_{x=(\delta_{\mathrm{GDL}}+\delta_{\mathrm{BL}})^-}=[RT\ln x_{\mathrm{H^+,m}}+F\Phi_2]|_{x=(\delta_{\mathrm{GDL}}+\delta_{\mathrm{BL}})^+}. \tag{4.47}$$

Membrane/anode CL boundary

At the membrane/anode CL boundary, concentrations of membrane species are set. Because the membrane is in contact with liquid water, just like at the BL/membrane boundary, Eq. 4.39 holds as long as the interfacial water mass transfer between membrane and liquid water is equilibrated. As explained above, the concentration of potassium cations is not set directly: the total amount of K^+ ions is set instead

$$\eta_{\mathrm{K^+}}|_{x=\delta_{\mathrm{GDL}}+\delta_{\mathrm{BL}}+\delta_{\mathrm{CEM}}}=\epsilon_{l,\mathrm{BL}}\delta_{\mathrm{BL}}c^0_{\mathrm{KHCO_3}}+\delta^0_{\mathrm{CEM}}c^0_{\mathrm{KM}}, \tag{4.48}$$

with $c^0_{\mathrm{KHCO_3}}$ and c^0_{KM} the initial concentrations of potassium cations in the liquid phase of the buffer layer and the membrane, respectively, and δ^0_{CEM} the initial membrane thickness. Concentrations for the other two membrane species ($H^+_{(m)}$ and $M^-_{(m)}$) are deduced from electroneutrality and Eq. 4.9. The electric potential of the membrane is set to zero (arbitrary), and the integral number of moles of membrane M^- per cross sectional area, used because of

the variable thickness of the membrane, is set to

$$\eta_{\mathrm{M}^-}|_{x=\delta_{\mathrm{GDL}}+\delta_{\mathrm{BL}}+\delta_{\mathrm{CEM}}} = \delta^0_{\mathrm{CEM}} c^0_{\mathrm{KM}}. \tag{4.49}$$

Finally, a rate-determining step (RDS) involving two electrons is considered for the oxygen evolution reaction (OER, reaction 4.3) and a Tafel-like expression is used to solve for the solid-phase potential of the anode (Eq. 3.9, with the activity of water taken to unity, $n_{\mathrm{OER}} = 2$ and the cathodic term being neglected). The rate, R_{OER}, is simply related to the current density i by Faraday's law $i = 2F\mathcal{R}_{\mathrm{OER}}$.

4.3.5 Additional model features

Total cell potential and cathode potential vs. a reference electrode

The total cell potential is simply the difference between anode and cathode potential at the gas channels

$$V = \Phi_1|_{x=\delta_{\mathrm{GDL}}+\delta_{\mathrm{BL}}+\delta_{\mathrm{CEM}}} - \Phi_1|_{x=0}\,. \tag{4.50}$$

As in chapter 3, we are interested in the cathode potential vs. a reference electrode (V_c) that was connected to the cell setup by means of a salt bridge as detailed in the experimental section of chapter 1. A similar equation as Eq. 3.16 is used for that purpose.

Convection in the BL

Because of gas evolution at the boundary between the BL and the CEM, there are likely some convection effects (mixing) in the BL. This is artificially taken into account by considering a region of the BL where concentrations of soluble species and partial pressures of gaseous species are uniform, and which lies between two Nernst layers of thickness δ_{DL}, as

proposed in ref. 35. The more the convection effects are pronounced, the larger the central region of uniform concentrations and partial pressures is.

Electrolyte flushing out

As mentioned above, upon cell operation, there is a net water flux from the anode toward the cathode. As a consequence, the electrolyte within the BL is progressively flushed out of the cell through the cathode side, yielding a decrease in conductivity of the BL, and possible flooding of the GDL. A thick BL (800 μm) was chosen for this study in order to slow down the conductivity decrease in the BL. A pseudo-transient mode was added to the model in order to account for electrolyte dilution within the BL. To this end, the flux of salt flushed from the BL was approximated by

$$N_{\mathrm{KHCO_3}}|_{x=\delta_{\mathrm{GDL}}} = N_{\mathrm{H_2O},l}|_{x=\delta_{\mathrm{GDL}}}\, \bar{V}_{\mathrm{H_2O},l}\, c_{\mathrm{K^+}}|_{x=\delta_{\mathrm{GDL}}}\,, \tag{4.51}$$

with the flux of liquid water determined from an overall water balance on the cell, which reads

$$N_{\mathrm{H_2O},l}|_{x=\delta_{\mathrm{GDL}}} = N_{\mathrm{H_2O},m}|_{x=\delta_{\mathrm{GDL}}+\delta_{\mathrm{BL}}} - N_{\mathrm{H_2O},g}|_{x=\delta_{\mathrm{GDL}}} + \frac{i\eta_{\mathrm{CO}}}{2F}. \tag{4.52}$$

The last term is a source term due to water produced by the CO_2 reduction reaction, where η_{CO} is the CO current efficiency. For each time step Δt, the total number of moles of K^+ per cross-sectional area is corrected using the following equation

$$\eta_{K^+}|^{t+\Delta t}_{x=\delta_{\mathrm{GDL}}+\delta_{\mathrm{BL}}+\delta_{\mathrm{CEM}}} = \eta_{K^+}|^{t}_{x=\delta_{\mathrm{GDL}}+\delta_{\mathrm{BL}}+\delta_{\mathrm{CEM}}} + N_{\mathrm{KHCO_3}}\Big|_{x=\delta_{\mathrm{GDL}}} \Delta t. \tag{4.53}$$

4.3.6 Model parameters

The input parameters used for the model are provided in tables 3.1, 3.2, 4.1, and 4.2. In table 3.1, the input parameters of interest are the diffusion coefficients of the soluble species and the thermodynamic data. The rate constants and the charge transfer coefficients for the RDSs of CO and H_2 evolution reactions (CER and HER, respectively) in $KHCO_3$ electrolyte are taken from table 3.2, and correspond to the values that were refined from experimental data on flat silver and gold electrode (see chapter 3). Table 4.1 provides some physical parameters for phases and interfaces between phases, as well as operating conditions (partial pressures of the gaseous species and total pressure at the cathode gas channel, and $KHCO_3$ initial concentration in the buffer layer) that were set in our experiments unless otherwise stated in the following. Physical parameters were either taken from the literature or were fitted to our data. Geometric parameters are gathered in table 4.2. Some were taken from the literature, like for the commercial GDL or the CEM, while others were measured, estimated, assumed, or fitted to experimental data.

Table 4.1: Values of various parameters, operating conditions, or physical properties for the phases and interfaces at 25 °C, used in the model (unless otherwise stated). a: assumed; e: estimated; f: parameter fitted to experimental data; s: set.

Gas phase						
		CO_2	H_2	CO	H_2O	Ar
Molar mass (g/mol)	M_i	44.01	2.02	28.01	18.02	39.95
Lennard-Jones characteristic length[80] (nm)	σ_i	0.3941	0.2827	0.3690	0.2641	0.3542
Lennard-Jones energy/k_B[80] (K)	ε_i/k_B	195.2	59.7	91.7	809.1	93.3
Partial pressure at cathode gas channel[s] (bar)	$p_{i,g}$	0.98138	0.00010	0.00010	0.03142	0.00000
Total pressure[s] (bar)	p_T	1.013				
Liquid phase						
Water partial molar volume[81] (cm^3/mol)	$\overline{V}_{H_2O,l}$	18.02				

Initial $KHCO_3$ concentration[s] (mol/L)	$c^0_{KHCO_3}$	0.5		
Membrane				
		HM	KM	H_2O
Partial molar volume (chapter 2) (cm^3/mol)	$\overline{V}_{i,m}$	566.00	542.00	16.30
Initial KM concentration (chapter 2) (mol/L)	c^0_{KM}	1.320		
Activity coefficient parameter[36] (J/mol)	b	-151		
Solid phase in GDL				
Bulk electronic conductivity[81] (S/cm)	σ_1	7		
Gas/liquid interface				
Water vapor pressure[81] (bar)	p_0^{vap}	0.03142		
Cathode catalyst/liquid interface				
Rate constants for CER (cm/s)	$k_{f,CER,1}$	Same as in table 3.2		
Rate constants for HER (mol/cm^2 s)	$k_{f,HER,1}$	Same as in table 3.2 for figure 4.3 2×10^{-13} for other simulations		
Charge transfer coefficients for CER and HER		Same as in table 3.2		
Anode catalyst/membrane interface				
Apparent OER rate constant[f] (mol/cm^2 s)	$k_{f,OER}a^b_{s_a-m}$	1.5 10^{-31}		
OER charge transfer coefficient[a]	β_{OER}	0.50		
Liquid/membrane interface				
Ion-exchange equilibrium constant[36]	K_{IER}	0.27		

4.3.7 Numerical implementation

The approach taken for the numerical implementation of the sandwich model is as follows. The governing equations were cast into finite differences using the approach detailed in Appendix C of Newman and Thomas-Alyea.[35] For the gas phase, backward and forward differences were used for diffusion equations and material balances, respectively, while this

Table 4.2: Values for geometric parameters of the various layers of the sandwich, used in the model (unless otherwise stated). a: assumed; e: estimated (see appendix 4.6.3); f: parameter fitted to experimental data; m: measured.

Diffusion medium		
Volume fraction of solid phase[45]	$\epsilon_{s,\mathrm{GDL}}$	0.4
Volume fraction of gas phase[45]	$\epsilon_{g,\mathrm{GDL}}$	0.6
Thickness[82] (μm)	δ_{GDL}	265
Cathode catalyst layer		
Active surface area per cross-sectional area of cell[f]	$a^b_{s_c-l}$	13 (Ag) 6 (Au)
Buffer layer		
Volume fraction of liquid phase[a]	$\epsilon_{l,\mathrm{BL}}$	0.92
Volume fraction of gas phase[a]	$\epsilon_{g,\mathrm{BL}}$	0.01
Total thickness[m] (μm)	δ_{BL}	800
Thickness of Nernst diffusion layers[a] (μm)	δ_{DL}	10
Cation-exchange membrane		
Initial membrane thickness (chapter 2) (μm)	δ_{CEM}	176.3
Miscellaneous		
Distance between catalyst layer and reference electrode[e] (μm)	$\delta_{\mathrm{CL-RE}}$	475

was the opposite for the liquid and membrane phases. The coupled differential equations in the spatial domain are solved with a banded solver, BAND(j), as described in Appendix C of Newman and Thomas-Alyea.[35] The discretization was done with 25 mesh points in each layer. Error was proportional to h^2, with h the mesh size. Note that unlike in chapter 3, the fluxes of species in the liquid phase have been considered as unknowns. Since the material balances are coupled, fluxes should be defined in a similar manner for all phases. Substituting flux expressions of soluble species (Eq. 4.6) directly into the material balances as we have done in chapter 3 would require the use of a control-volume formulation to ensure an error proportional to h^2. This is because there are internal boundaries in the sandwich, and because BAND(j) is tridiagonal.[83] However, with a control-volume approach, fluxes of soluble species are defined at half-mesh points, while those for membrane and gas phase species are defined at mesh points (see section C.6 of ref. 35). Therefore, this situation is not satisfactory in the context of interfacial mass transfer between phases, especially equilibrated

phases, which explains why fluxes of species in the liquid phase were solved for explicitly.

4.4 Results and discussion

4.4.1 Experiments and modeling of the current density – potential curves

Figure 4.3 presents the experimental partial current densities of CO and H_2 (and the total current densities) obtained at 15 min galvanostatic electrolysis with the BL-type cell, using three different catalysts at the cathode, namely unsupported Ag (average particle size 1 μm,Alfa Aesar), unsupported Au (average particle size 1 μm, Alfa Aesar), and supported Au on Vulcan carbon XC-72 (40 wt.% Au, E-TEK Inc.). The results for Ag are reproduced from figure 1.6. For each current density investigated, a new cell (containing a new catalyst layer) was assembled, to avoid any cell history effect. The onset of CER occurs at a potential ca. 200 mV more positive on Au as compared to Ag, regardless of the kind of Au catalyst that was used. This is lower than what was found for Au and Ag flat electrodes (see chapter 3). This may be due to a different active surface area per cell cross-section area for Ag and Au catalyst powders, as discussed in the following. The CO efficiency goes through a maximum of ca. 76% and 97% at potentials of -1.23 and -1.35 V vs. SCE for unsupported and supported Au catalysts, respectively. For unsupported Ag catalyst, a maximum current efficiency for CO of ca. 83% is reached at about -1.47 V vs. SCE. Although not visible on figure 4.3, regardless of the catalyst, the sum of CO and H_2 efficiencies departs from unity at low current densities (ca. 80% at -5 mA/cm^2 for all catalysts). Because formate was found to be in very limited amount within the electrolyte of the buffer layer (as shown in chapter 1 for Ag), it cannot account for the missing efficiency, thus ascribed to either other unidentified by-products or experimental errors.

Just like we did for Ag-based electrodes in chapter 1, it is interesting to compare the

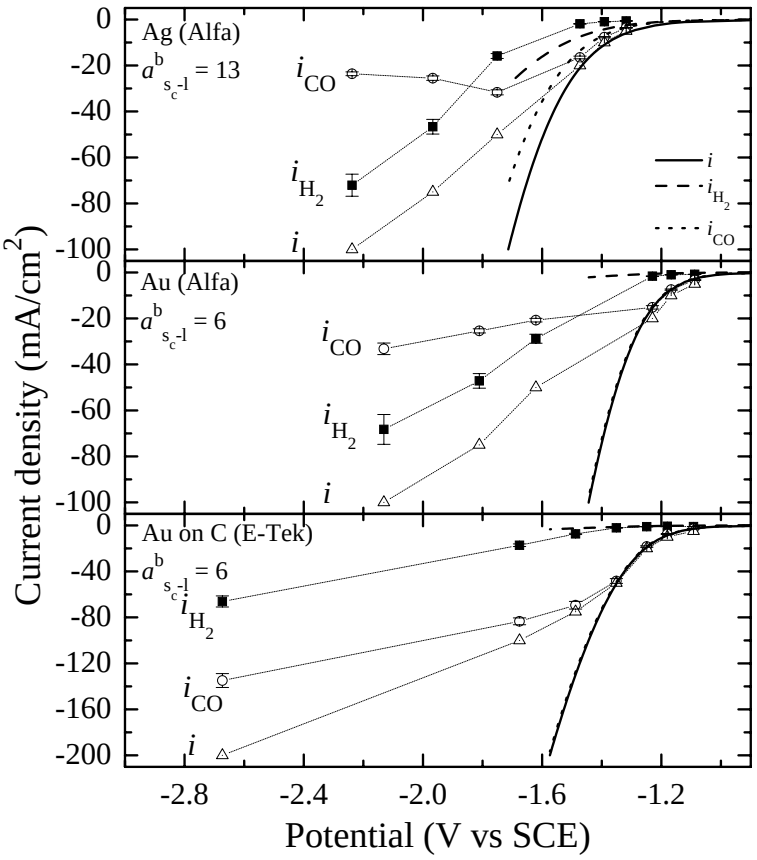

Figure 4.3: Experimental partial current density for CO and H_2 evolution as a function of cathode potential at 15 min electrolysis with the buffer-layer-based cell operating with different GDEs (symbols), and simulated curves using the model (lines). Lighter lines going through the symbols have also been added for clarity.

experimental results obtained on Au-based electrodes with what is reported in the literature. Table 4.3 gathers some of the results reported for CO_2 reduction on Au-based electrodes in aqueous $KHCO_3$ electrolyte. First of all, these results look fairly disparate. CO current efficiencies obtained on unsupported Au-based cathode in this work are slightly lower than most of those reported, while they are slightly higher for supported Au-based cathodes. The current densities, however, are ca. 5 to 10 times higher than those reported, which clearly emphasizes the advantage of using gas-diffusion electrodes (GDEs) over regular flat electrodes. To our knowledge, this is the first report of such a high current density for CO

evolution (i.e., -135 mA/cm^2 on supported Au catalyst). Data from figure 4.3 also show that the use of a supported Au catalyst (on carbon) is not much an issue when using Au as compared to Ag (at least for short electrolysis run times), for which the catalyst selectivity for CO was very poor either when a supported catalyst was used or when there was a high amount of carbon in the catalyst layer (see chapter 1).

Table 4.3: Literature survey of the typical current efficiencies of CO, $HCOO^-$, and H_2 obtained during electrolyses on Au electrodes in aqueous $KHCO_3$ electrolyte saturated with pure $CO_{2(g)}$ at room temperature and pressure. For convenience, potentials are expressed versus SCE.

Electrode	Electrolyte	Current efficiencies	ref.
Au-loaded GDE	0.2 M $KHCO_3$	40 to 50% CO between -1.34 and -2.74 V and ca. 10% $HCOO^-$ efficiency between -1 and -3.24 V; current densities not provided; H_2 efficiency not determined experimentally.	19
Au plate	0.5 M $KHCO_3$	81.2 to 93% CO, 0.4 to 1% $HCOO^-$, and 6.7 to 23.2% H_2 at -1.38 V and -5 mA/cm^2.	3,54
Au plate	0.1 M $KHCO_3$	87.1% CO, 0.7% $HCOO^-$, and 10.2% H_2 at -1.38 V and -5 mA/cm^2.	9
Au plate	0.1 M $KHCO_3$	81.5% CO, no $HCOO^-$, and 23% H_2 at -1.29 V and -3.8 mA/cm^2; 15.8% CO, 6% $HCOO^-$, and 86% H_2 at -1.64 V and -41.3 mA/cm^2.	8
Au plate	1 M $KHCO_3$	ca. 43 to 62% CO and ca. 40 to 70% H_2 at -1.34 V and ca. 16 to 18% CO and ca. 95 to 105% H_2 at -1.74 V, depending on the surface treatment and the position of the electrode; current densities not provided.	55
Au deposited on a CEM	1 M $KHCO_3$	ca. 65% CO and ca. 70% H_2 at -1.34 V and ca. 35% CO and ca. 60% H_2 at -1.74 V; current densities not provided.	55
Porous Au film	0.5 M $KHCO_3$	ca. 85% CO at -1.38 V and ca. -6 mA/cm^2; almost no H_2 was detected (at -2 V); $HCOO^-$ efficiency not determined experimentally.	58
Sputtered Au electrode	0.1 M $KHCO_3$	ca. 85 to 93% CO between -1.20 and -1.24 V and ca. -1 to -7 mA/cm^2.	57

Simulations of the steady-state partial current densities as functions of cathode poten-

tial were performed using the mathematical model of the overall cell, where the values for the kinetic parameters for CER and HER derived from experiments on flat metal electrodes in $KHCO_3$ electrolyte were taken from table 3.2. Simulations are overlaid to the experimental data of figure 4.3. A single parameter $a^b_{s_c-l}$, namely the active surface area of the catalyst layer per cross-sectional area of cell, was adjusted, and the values are displayed on the figure. A value of about 13 is found for Ag while that for Au is only about 6 (for both supported and unsupported catalysts). Considering spherical particles of 1 μm diameter, a catalyst loading of 10 mg/cm^2 yields values of $a^b_{s_c-l}$ of 57 and 31 for Ag and Au, respectively, which is five times higher than the values refined from the experimental electrochemical data. Therefore, the effective particle diameter we can derive from the experimental data is ca. 5 μm for both Ag and Au. As for the supported Au catalyst, one would expect a much higher active surface area than for the unsupported one, since it is generally made with submicrometer particles or nanoparticles.

The simulations agree pretty well with the data at low current density, except for hydrogen evolution on Ag, for which the simulation overpredicts the partial current density. Consequently, this rate constant was readjusted to a value about 4 times lower ($k_{f,\mathrm{HER},1} = 2\times10^{-13}$ mol/cm^2 s) to match the data. This value will be used for all the simulations in the following. We do not have any clear explanation for this discrepancy. At high current density, however, the simulations largely underpredict the overpotential for CER and HER on both catalysts, and overpredict the current efficiency of CO. The experimental data are affected by a strong ohmic contribution, which shows up only at substantial values of current density, as demonstrated in figure 4.4 where the cathode resistance not accounted for in the model is displayed. This resistance increases almost linearly with the current density with a slope that is poorly dependent on the type of catalyst. An extrapolation of this quasi-linear behavior at zero current density is fairly consistent with the values derived from impedance spectroscopy before electrolysis (see Appendix 4.6.2), except for the cells based on Au-supported catalyst. (We do not have any explanation for this discrepancy.) In the following, the model will be used to provide some possible reasons for this current-density-dependent resistance as well

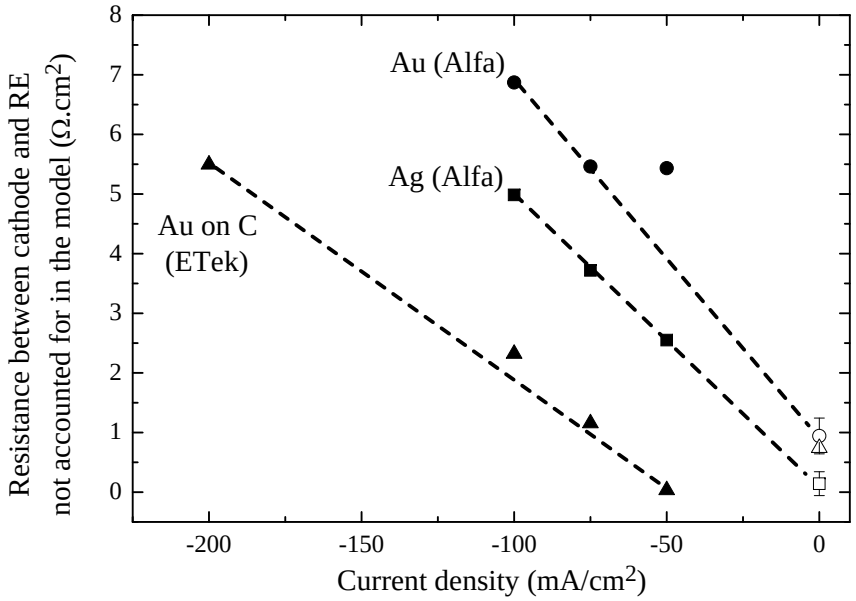

Figure 4.4: Cathode resistance not accounted for in the model. For current densities higher than 50 mA/cm^2 in magnitude, it corresponds to the difference between the experimental and simulated cathode potentials (given in figure 4.3) over the current density (filled symbols). At zero current, it corresponds to the difference between the resistance determined by impedance spectroscopy before electrolysis and the resistance predicted by the model (see Appendix 4.6.2) (open symbols). Straight lines have been added for eye guidance only.

as for the loss of CO selectivity at high current density, but before getting into that, the influence of CO_2 partial pressure and $KHCO_3$ concentration in the buffer layer at low current density is examined for Ag-based GDEs.

4.4.2 Effect of CO_2 partial pressure

In figure 4.5, partial current densities of CO and H_2 (as well as total current density) and corresponding current efficiencies at 15 min potentiostatic electrolyses using Ag-based GDEs are presented for various CO_2 partial pressures in the cathode gas channel. Ar was mixed with CO_2 in order to set the CO_2 partial pressure. In those experiments, the calculated concentration of HCO_3^- anions in the liquid phase of the buffer layer varies only slightly (ca. 0.48 mol/L at zero current density for the lower CO_2 pressure). CO current density exhibits

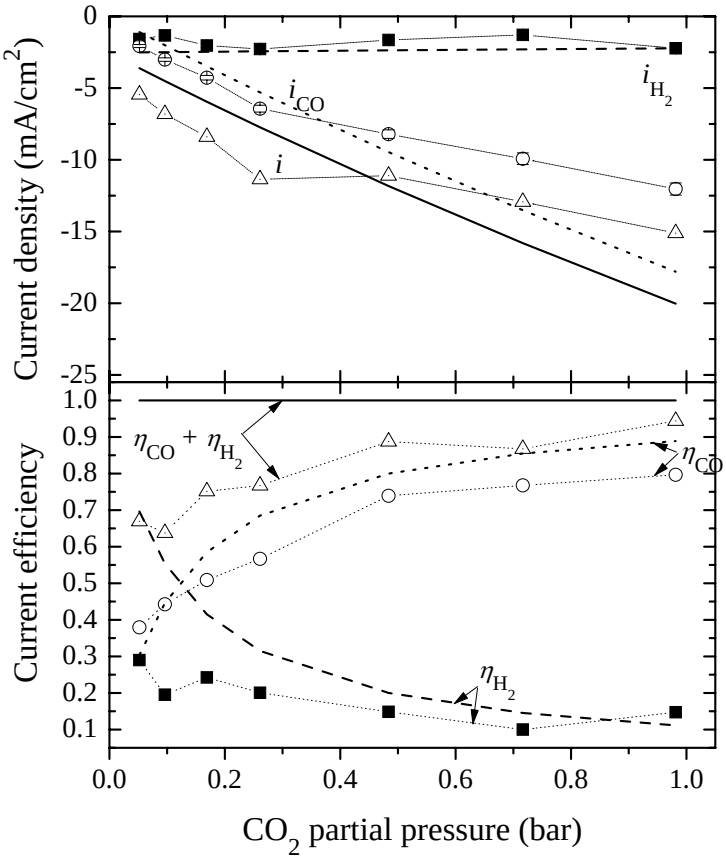

Figure 4.5: Experimental partial current density (top) and current efficiency (bottom) of CO and H_2 obtained with the buffer-layer-based cell with a Ag-based GDE at -1.5 V vs. SCE and 15 min electrolysis as a function of the CO_2 partial pressure of the feed gas (symbols) and corresponding results of the model (lines). Lighter lines going through the symbols have also been added for clarity.

a quasi-linear dependence on p_{CO_2} (in good agreement with the idea that only CO_2 species can be reduced), but with different slopes whether p_{CO_2} is lower or larger than ca. 0.25 bar. H_2 current density is almost invariant with p_{CO_2}. Like for data in figure 4.3, the sum of CO and H_2 current densities is lower than the total current density, especially at low current densities.

Simulations using the mathematical model of the cell are overlaid to the experimental data. The simulation of H_2 current density is in good agreement with the experimental one.

(The invariance of H_2 current density with CO_2 partial pressure is well captured.) Simulated CO current density matches the data pretty well for $p_{CO_2} \leq 0.25$ bar, but does not account for the slope change at higher p_{CO_2}, which is likely due to a CO_2 mass-transfer limitation, not accounted for in the simulation with the actual set of input parameters. A similar trend is observed in figure 3.9 (at the most negative potential). This mass-transfer limitation could be due to a flooding of the GDL, as discussed in the following.

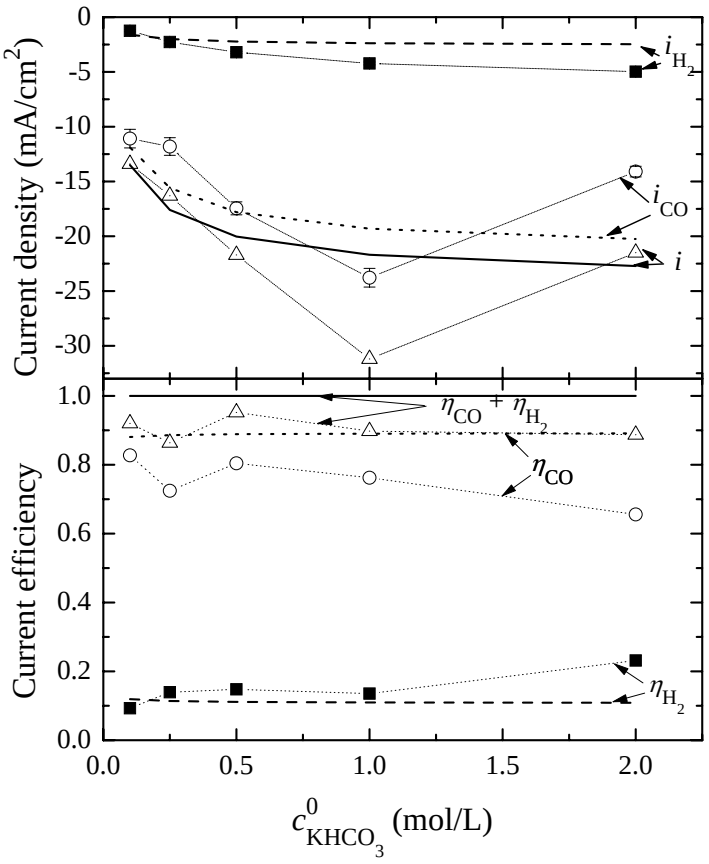

Figure 4.6: Experimental partial current density (top) and current efficiency (bottom) for CO and H_2 obtained with the buffer-layer-based cell with a Ag-based GDE at -1.5 V vs. SCE and 15 min electrolysis as a function of the initial bicarbonate concentration in the buffer layer and corresponding results of the model (lines). Lighter lines going through the symbols have also been added for clarity.

4.4.3 Effect of salt concentration in the buffer layer

In figure 4.6, the influence of $KHCO_3$ concentration in the buffer layer is examined. As the salt concentration is increased from 0.1 to 1 mol/L, the current density increases. However, no significant changes in current efficiencies are observed. Because potentiostatic electrolyses were used (where the cathode potential was set vs. a reference electrode), this increase in current density is likely correlated with the decrease in potential drop between the cathode and the reference electrode. A decrease of the total current density is observed when $c^0_{KHCO_3}$ increases from 1 to 2 mol/L. This current decrease is mostly due to a decrease in CO current density (H_2 current keeps on increasing). It seems too large to be solely accounted for by a salting out effect of CO_2 at high salt concentration.

Simulations performed at different salt concentrations in the buffer layer exhibit an increase of the current densities as a function of $c^0_{KHCO_3}$, mainly at low salt concentration, which is due to the decrease of the potential drop between the cathode and the reference electrode as pointed out above. On the contrary with the experimental data, the current density does not decrease between $c^0_{KHCO_3} = 1$ and 2 mol/L. Besides, the model shows essentially no effect of $c^0_{KHCO_3}$ on the current efficiencies, in pretty good agreement with the experimental data.

The experimental and simulation results on the influence of p_{CO_2} and $c^0_{KHCO_3}$ tend to confirm that dissolved CO_2 is the species which is reduced, and not HCO_3^- anions. This is in good agreement with the choice of reaction 3.1 as RDS for the CER.

4.4.4 Concentration profiles and convection in the buffer layer

Because a rather thick buffer layer was used (800 μm), a limiting current density is expected to limit the practical cell performance. However, as mentioned earlier, CO_2 is formed at the boundary between the BL and the CEM through reaction 4.4, and thus convection effects within the BL (treated as a multiphase system composed of a solid, a gas, and a liquid

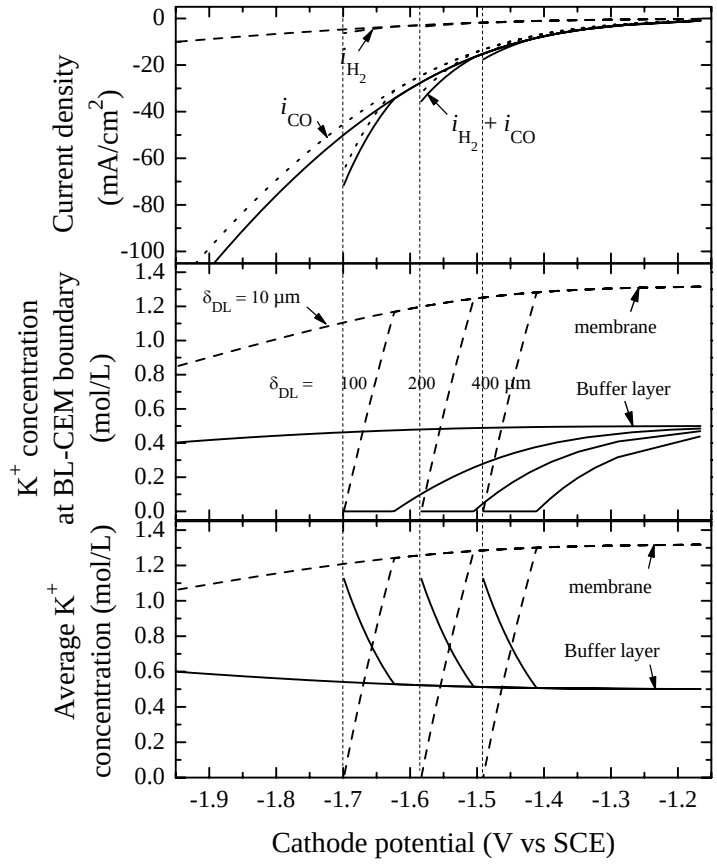

Figure 4.7: Top: Simulation of the effect of the convection within the buffer layer on the partial current density of H_2 and CO by using a Nernst layer of different thicknesses δ_{DL} at both sides of the buffer layer. Middle: K^+ concentrations in the liquid electrolyte of the buffer layer and in the membrane at the boundary between the buffer layer and the membrane. Bottom: Average K^+ concentrations in the liquid electrolyte of the buffer layer and in the membrane. Simulations were run for the parameters adjusted for a silver-based GDE, with $\epsilon_{l,\mathrm{BL}} = \epsilon_{g,\mathrm{BL}} = 0.465$. Values of δ_{DL} are labeled in the middle plot, but not repeated in the top and bottom plots. The vertical dashed lines correspond to the most negative potentials at which a convergence was obtained for the corresponding value of δ_{DL}.

phase) are likely. In order to account (in a simple way) for convection, we considered that the concentrations of all the species (both gaseous and soluble) are uniform throughout the BL except at the boundaries with the cathode CL and the CEM, where Nernst diffusion layers of thickness δ_{DL} were considered. The higher the convection in the BL is, the thinner the two Nernst layers are.

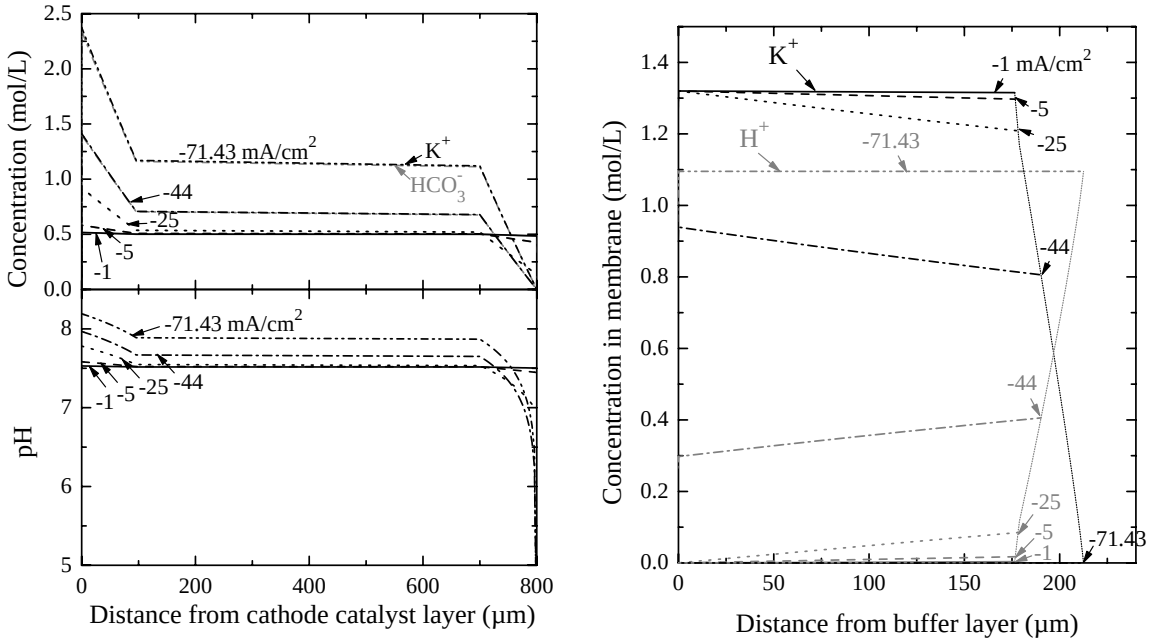

Figure 4.8: Simulation of concentration profiles of soluble species and pH profile in the buffer layer (left) and concentration profiles in the membrane (right) for the electrolysis cell operating under various current densities. Same parameters as in figure 4.7 (silver-based GDE), with $\delta_{\mathrm{DL}} = 100\mu$m.

The influence of δ_{DL} on the limiting current density was examined using the model (figure 4.7). Although a volume fraction of 0.01 was assumed for the gas phase in the base case, here simulations were performed assuming both volume fractions for gas and liquid phases to be equal to 0.465. (This is to avoid convergence issues.) As expected, when the thickness of the Nernst layers is reduced, a higher limiting current density is reached. For the thickness we have chosen as the base case (10 μm), no limiting current density is reached up to -100 mA/cm^2. Interestingly, whatever the thickness of the Nernst layers, the K^+ concentration in the liquid phase at the BL/CEM boundary decreases in two steps as the current density increases. The first one is simply caused by the concentration gradient build-up within the diffusion layers of the BL. (See the plot of concentration profiles in the BL, figure 4.8, for which $\delta_{\mathrm{DL}} = 100\mu$m.) Meanwhile, a concentration gradient of potassium also builds up within the membrane, although the mole fraction of K^+ in the membrane at the

BL/CEM boundary does not vary much (figures 4.7 and 4.8). When the K^+ concentration in the liquid phase at the BL/CEM boundary becomes substantially low, the second step begins; the mole fraction of K^+ in the membrane at the same boundary starts decreasing, and K^+ ions are driven from the membrane to the BL. The membrane is therefore converted to a proton form, and swells consequently (figure 4.8) because of an associated water uptake. The large increase in potassium concentration in the liquid phase is accompanied by a slight pH increase, which is minor compared to the large pH decrease experienced by the membrane. The limiting current density is reached when the membrane is almost fully exhausted in potassium ions. Associated partial-pressure profiles for the gaseous species are reported in figure 4.9 and show a progressive decrease of p_{CO_2} at the catalyst layer as the current density increases, together with an increase of p_{CO}, CO being the major product predicted by the model. Although not visible on the figure, p_{H_2} increases as well. There are in fact small and opposite partial-pressure gradients for CO_2 and CO in the BL (although much lower than those in the GDL) since CO_2 is consumed at the cathode CL and formed at the BL/CEM boundary, while CO is produced at the cathode CL.

To conclude, those simulations tend to confirm that there are likely some convection effects (mixing) within the BL, especially since the limiting current density simulated for the case without convection is substantially lower than the current densities at which we could operate the cell experimentally. Finally, the value of δ_{DL} does not affect the partial current densities of CO and H_2 much below the limiting current density. This is why we took an arbitrarily low value of 10 μm for δ_{DL}, at which it is ensured that no limiting current density is reached in the range of interest.

4.4.5 Flooding of the GDL and liquid-phase exhaustion from the BL

As we have seen in figure 4.3, the model does not predict the experimental results except at low current densities. The strong ohmic contribution that shows up at substantial values of

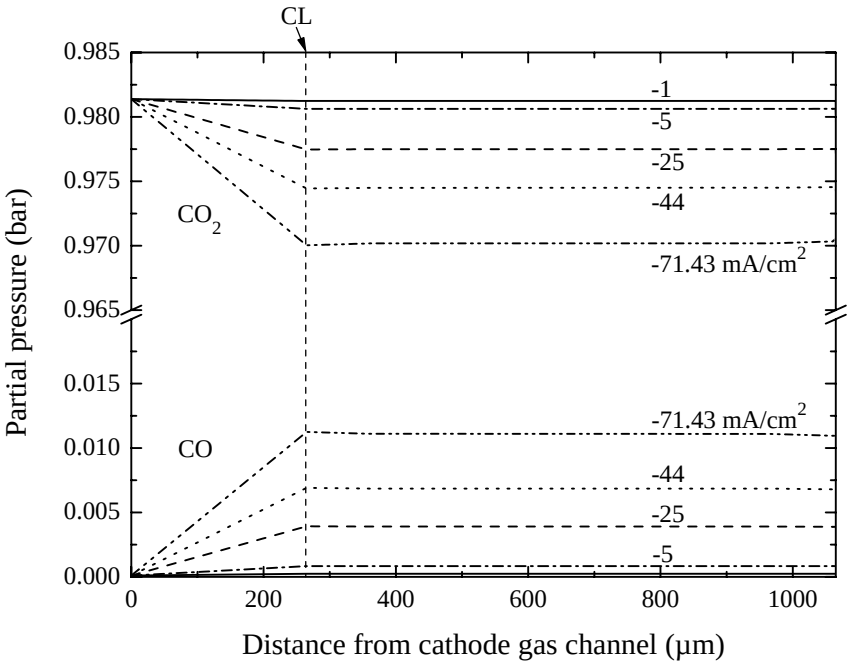

Figure 4.9: Simulation of partial-pressure profiles of gaseous species across the gas-diffusion layer and the buffer layer for the electrolysis cell operating under various current densities. Same parameters as in figure 4.7 (silver-based GDE), with $\delta_{\mathrm{DL}} = 100\mu$m.

current density might be caused by an excessive decrease of the liquid-phase volume fraction in the BL. Indeed, since gaseous CO_2 is formed at the BL/CEM boundary, the volume fractions of the gas and liquid phases in the BL can vary with the current density (and they might also vary with the position across the BL). Because we do not know how they vary exactly with the current density and position, simulations were run for different values of the volume fractions of the two phases, assumed independent of the current density and uniform throughout the BL (figure 4.10). As expected, an increase of the gas volume fraction in the BL increases the potential drop between the cathode catalyst layer and the reference electrode, which is larger at higher current density. For the highest gas volume fraction (90%), there is a kink in the $i - V_c$ curves, which corresponds to the point where the K^+ concentration in the liquid phase at the BL/CEM boundary reaches almost zero. For higher current densities, K^+ ions are driven from the membrane toward the liquid phase in the BL. At low liquid-phase volume fraction, precipitation of $KHCO_3$ is prone to occur (preferentially

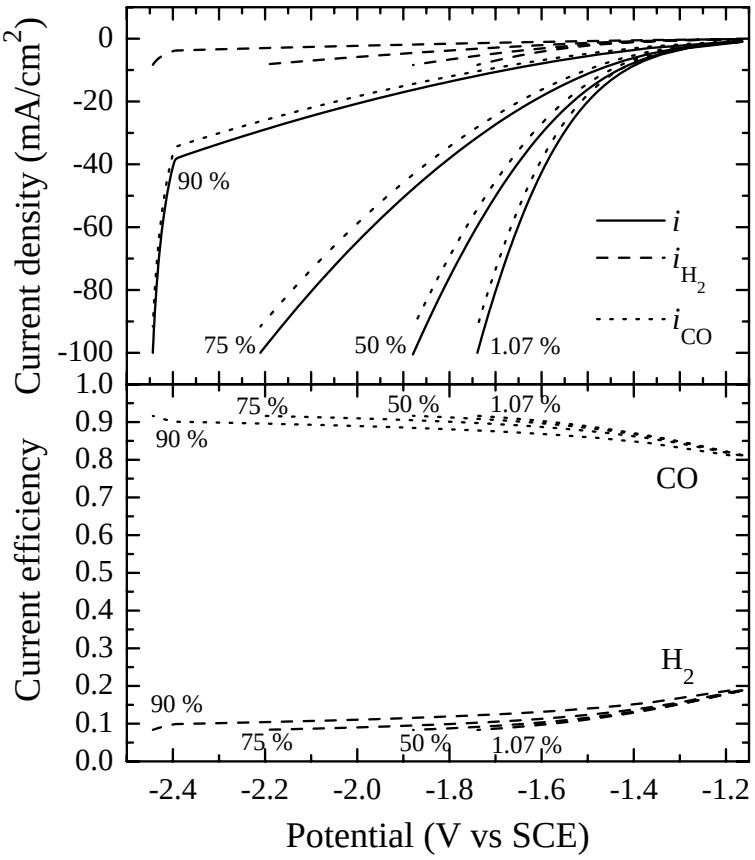

Figure 4.10: Simulation of the effect of increasing the gas volume fraction in the buffer layer on the partial current density of H_2 and CO and their corresponding current efficiency. Labels stand for the percentage of gas-phase volume fraction in the buffer layer relative to gas and liquid phases. Simulations were run for the parameters adjusted for a silver-based GDE.

close to the cathode CL); for instance the model predicts a concentration of K^+ ions as high as 4.08 mol/L at the cathode CL at -100 mA/cm^2 for the BL with 90% gas phase, while the solubility limit of $KHCO_3$ is ca. 3.62 mol/L at room temperature. Finally, it is worth noting that the current efficiencies for CO and H_2 are not much affected by the gas-volume-fraction increase in the BL, unlike what is observed experimentally (figure 4.3).

Another cell limitation that may explain the mismatch between the model predictions and the experimental data of figure 4.3 is a consequence of the above effect. Indeed, if the

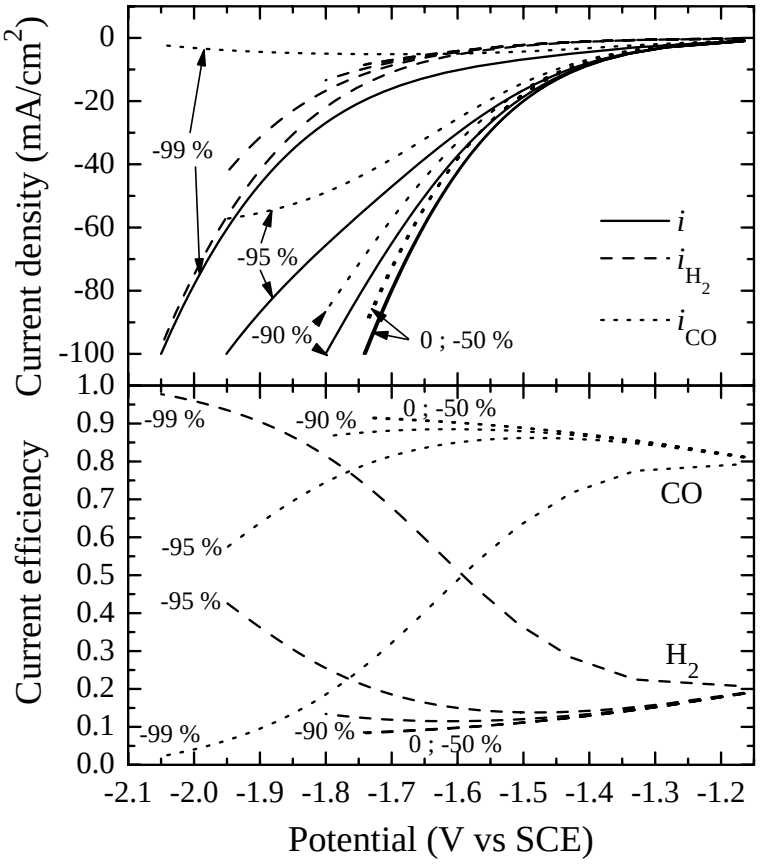

Figure 4.11: Simulation of the effect of decreasing the gas volume fraction in the diffusion medium on partial current density of H_2 and CO and their corresponding current efficiency. Labels stand for the percentage of decrease of the gas volume fraction compared to the base case. Simulations were run for the parameters adjusted for a silver-based GDE.

liquid-phase volume fraction decreases in the BL, it is flushed toward the GDL, and may lead to its flooding. Since we have not considered a liquid phase in the GDL, we simply account for this effect by decreasing the gas volume fraction in that layer (figure 4.11). This creates a larger mass-transport limitation for CO_2 to reach the cathode CL, and hence a decrease of the CO current density (and of the CO current efficiency), as compared to the base case, is observed. The H_2 current density is not significantly affected. Decreasing the gas volume fraction by up to 50% shows almost no effect. The flooding effects become substantial only for high extents of flooding (low gas volume fraction in the GDL). For the GDL flooded at

99%, the $i - V_c$ curve almost collapses with that for hydrogen evolution.

For the model to capture the experimental $i - V_c$ curves of figure 4.3, a combination of the two effects discussed above is probably required. However, because of the numerous assumptions, the adjusted volume fractions that would result from an attempt to fit the data would probably not be very meaningful; hence this is not reported.

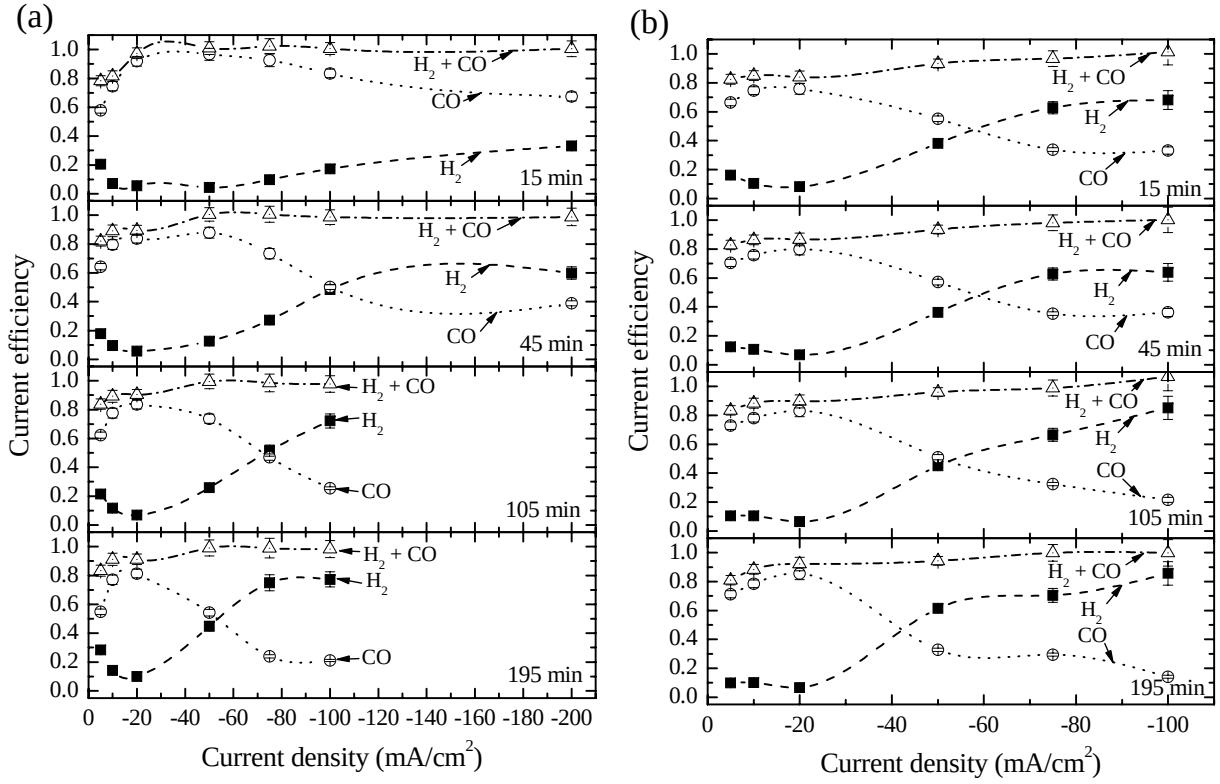

Figure 4.12: Experimental current efficiency of CO and H_2 as a function of the current density for different run times obtained with two different Au-based GDEs. (a) Au supported on Vulcan XC-72 (E-TEK) (b) Unsupported Au (Alfa).

4.4.6 Cell operation over time

The loss of CO_2-reduction-products selectivity with electrolysis time has been extensively reported in the literature, especially for planar metal electrodes.[20, 22, 23, 78] We have shown in chapter 1 that Ag-based GDEs also exhibit a loss of CO selectivity with operation time.

Additionally, we have shown that the presence of substantial amounts of carbon in the GDE was very detrimental to the initial CO selectivity as well as to the CO selectivity retention upon electrolysis. Figure 4.12 presents similar experimental data for the supported and unsupported Au-based GDEs. A general comment is that CO selectively is much better retained on unsupported Au-based GDEs than it is on unsupported Ag-based GDEs. For unsupported Au-based GDEs, a very little decrease in CO current efficiency is observed upon almost 200 min electrolysis. The decrease is faster for supported Au-based GDEs. However, contrary to Ag-based GDEs, it is not obvious that this is due to the presence of carbon; additional electrolyses performed with Au-GDEs made from unsupported Au (Alfa) mixed with various amounts of acetylene-black carbon reveal no significant effect of the carbon on the CO selectivity (both initially and upon electrolysis). Perhaps there is either an influence of the gold particles themselves [between unsupported Au (Alfa) and supported Au (E-TEK)] or of the kind of carbon that is used (the supported Au catalyst is made with Vulcan carbon).

Several possible causes can be pointed out to explain the loss of CO selectivity over time, such as catalyst poisoning and accumulation of unidentified CO_2-reduction products in the BL. Furthermore, because water is dragged across the membrane from anode to cathode, a dilution of the liquid phase in the BL is expected upon cell operation. In order to figure out whether such a dilution may contribute to a decrease of CO current efficiency over time, this effect was introduced in the model (pseudo-transient operation), and simulations of cell operation under various current densities are reported in figure 4.13. The cathode potential decreases continuously until a time after which it remains almost constant. This transition time occurs sooner when the cell operates under high current density. The potential decrease results from an increase of the potential drop between the cathode CL and the reference electrode, caused by a conductivity decrease of the liquid phase (dilution of the BL electrolyte). After a nearly zero K^+ concentration in the liquid phase is reached at the BL/CEM boundary, K^+ is driven out of the membrane. However, it does not accumulate in the BL, as seen on the middle plot of figure 4.13; it is driven out of the cell as a result of the net water flux from anode to cathode. When all the K^+ is exhausted from the membrane

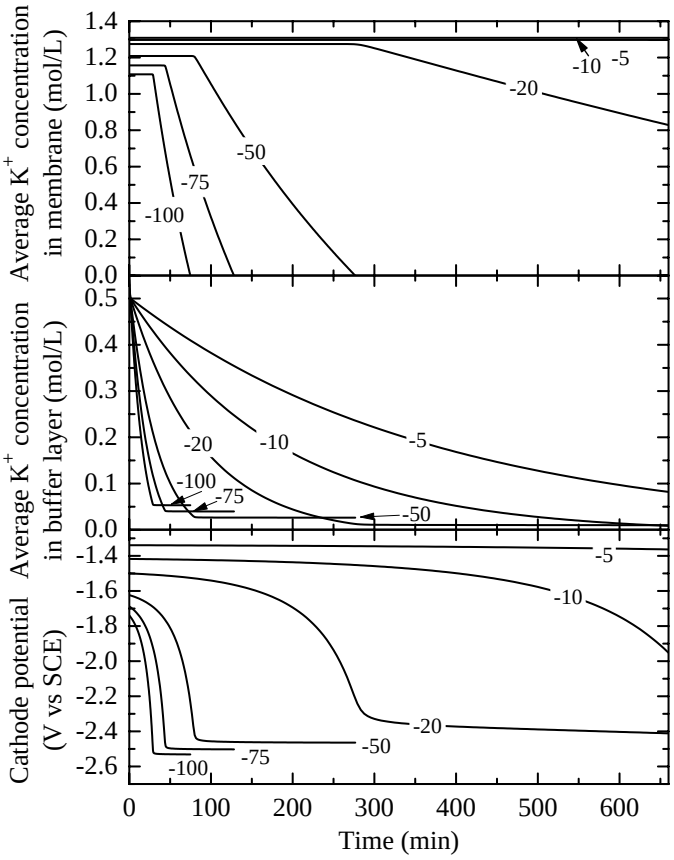

Figure 4.13: Pseudo-transient simulation of the electrolysis cell operating under various current densities (in mA/cm^2), showing the variation of the average potassium concentration in the membrane (top), in the buffer layer (middle), and the cathode potential (bottom) as a function of run time. Simulations were run for the parameters adjusted for a silver-based GDE.

(i.e., the membrane is fully converted to a proton form), the cell can no longer operate at the targeted current density because no K^+ ions are supplied to the BL anymore. Experimentally longer operation times than predicted are found for a specified current density. For instance, unlike model predictions, the cells using Au-based catalysts still operate after 195 min at -100 mA/cm^2 (see figure 4.12). This is perhaps because the K^+ concentration at the cathode CL was used to calculate the flux of $KHCO_3$ driven out of the BL in the model (Eq. 4.51), which maximizes the flux. Also, the source term in the expression of the liquid-water flux at the cathode CL (Eq. 4.52), coming from the CER, is overestimated because higher

CO efficiencies than those experimentally observed are predicted by the model, especially at long operation times where experimental CO efficiency decays. The predicted CO current efficiency does not vary much over time of operation, and therefore it is not shown in figure 4.13. This shows that this dilution effect does not affect the CO current efficiency over time, which is in agreement with the experimental results for various initial concentrations of potassium bicarbonate (see figure 4.6).

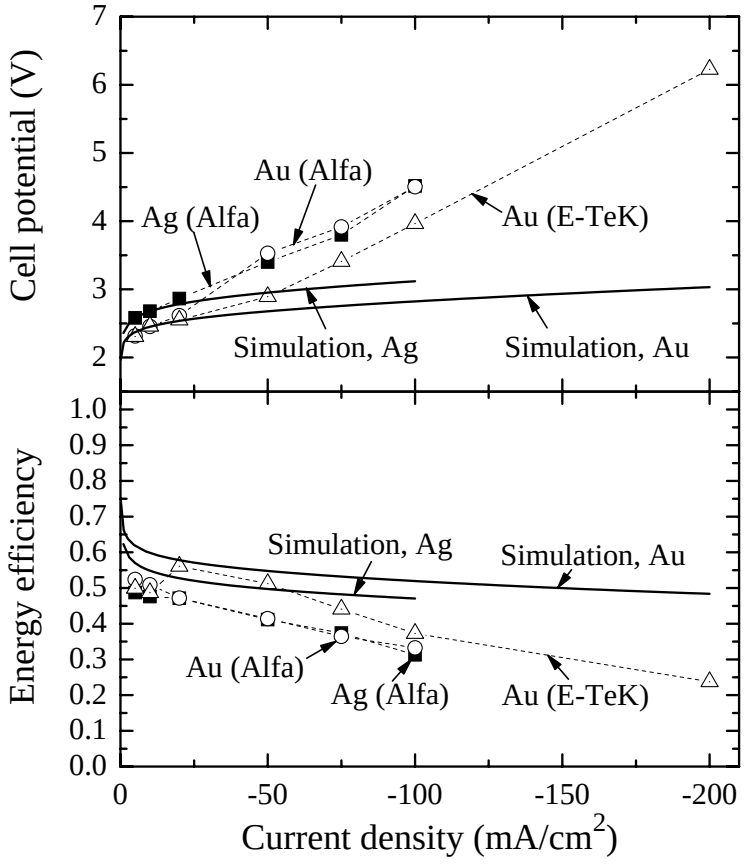

Figure 4.14: Experimental cell potential and energy efficiency of the electrolysis cell as a function of current density at 15 min electrolysis with various types of GDEs (symbols), and simulated curves using the model for Au and Ag-based GDEs (lines). Lighter lines going through the symbols have also been added for clarity.

4.4.7 Overall cell performance and energy efficiency

The total cell potential as a function of current density is provided in figure 4.14 for the three types of catalysts studied, together with the cell energy efficiency, calculated using Eq. 1.17. The cell potential and energy efficiency for Ag-based cells are reproduced from the same reference. At low current density ($\leq$ 20 mA/cm^2 in magnitude), the cell potential of the two kinds of Au-based cells is very similar, and ca. 250 mV lower than that of the Ag-based cell, and this is well captured by the model. [The apparent rate constant for the OER at the anode ($k_{f,\mathrm{OER}} a_{s_a-m}^{b}$) was fitted to the experimental data while setting the charge transfer coefficient (β_{OER}) to a value of 0.5 (see table 4.1).] This is not true any more at higher current densities ($>$ 20 mA/cm^2 in magnitude), where the cell potential for unsupported Au-based cells increases more than that of supported Au-based cells and comes closer to that of Ag-based cells. Unfortunately, fairly large deviations were observed from one cell to an identical cell at high current density, and it would be interesting to repeat the same experiments several times in a systematic way to put error bars on the curves. These error bars are likely fairly large at high current density, and therefore it is hard to draw conclusions from this different behavior between the two Au-based cells. However, it is clear that the cell potential predicted by the model is lower than the experimental one, for all types of cell. The possible reasons for this discrepancy have been discussed above. At low current density, the energy efficiencies for the three types of cell are pretty close to each other, and around 50%. The model overpredicts this value, mainly because the sum of the current efficiencies for H_2 and CO is less than 100% at low current density, as mentioned previously. At high current density, the energy efficiencies are overpredicted by the model because the actual cell potentials are higher than those expected from the model.

4.4.8 Performance of a cell using a porous AEM as BL

Finally, it is interesting to use the model to predict what the overall cell performance would be for an improved cell design. This is of interest to evaluate whether more experimental

Table 4.4: Values of some parameters and operating conditions used in the model for the electrolysis cell based on the use of a porous anion-exchange membrane between the cathode catalyst layer and the cation-exchange membrane (CEM). The other parameters are the same as in tables 4.1 and 4.2, unless otherwise stated. s: set; a: assumed.

Porous AEM layer		
Volume fraction of membrane phase[s]	$\epsilon_{m,\mathrm{AEM}}$	0.60
Volume fraction of gas phase[s]	$\epsilon_{g,\mathrm{AEM}}$	0.40
Total thickness[s] (μm)	δ_{AEM}	20
Concentration of cationic sites[a] (mol/L)	$c^0_{\mathrm{M}^+}$	1.32
CEM layer		
Initial membrane thickness (in proton form)[s] (μm)	δ_{CEM}	60.7
Inlet gas pressure		
Total pressure[s] (bar)	p_T	3
CO_2 partial pressure at cathode gas channel[s] (bar)	$p_{\mathrm{CO_2},g}$	2.96838

work is worthwhile to improve the actual cell design further. In an improved design, the BL would be replaced by a thin layer of a porous anion-exchange membrane, so that there would be no limiting current, as well as no dilution effect upon operation because of the net flux of water from anode to cathode. This anion-exchange membrane essentially prevents protons from reaching the cathode catalyst layer. It needs to be porous to allow CO_2 gas formed at the AEM/CEM boundary to be evacuated. (Otherwise, a delamination of the AEM and the CEM would result.) The pores could also serve for liquid-water transport. A consequence of the use of an AEM is that the CEM would essentially be in the proton form. For simplicity, to simulate such a porous AEM, a uniform concentration of cationic sites, taken arbitrarily equal to M^- concentration in the CEM (i.e., 1.32 mol/L when the CEM is in the K^+-form), was considered. The same transport properties as those used for the liquid phase in the BL are assumed for the anionic and neutral species. Along the same line, all the equilibrium constants for the acid-base reactions and the interfacial mass transfer of CO_2 and H_2O, as well as rate constants for the CER and HER reactions are unchanged as compared to the base case. Because we are not anymore concerned with the dilution effect, a thin AEM can be used (20 μm). The porosity of the AEM is considered to be 40%, and the pores are

assumed to be filled with gas only. The CEM thickness is reduced; Nafion 112 is considered instead of Nafion 117. Finally, the total gas pressure is increased to 3 bars, to increase CO_2 solubility. The operating conditions and model parameters for such a cell are summarized in table 4.4.

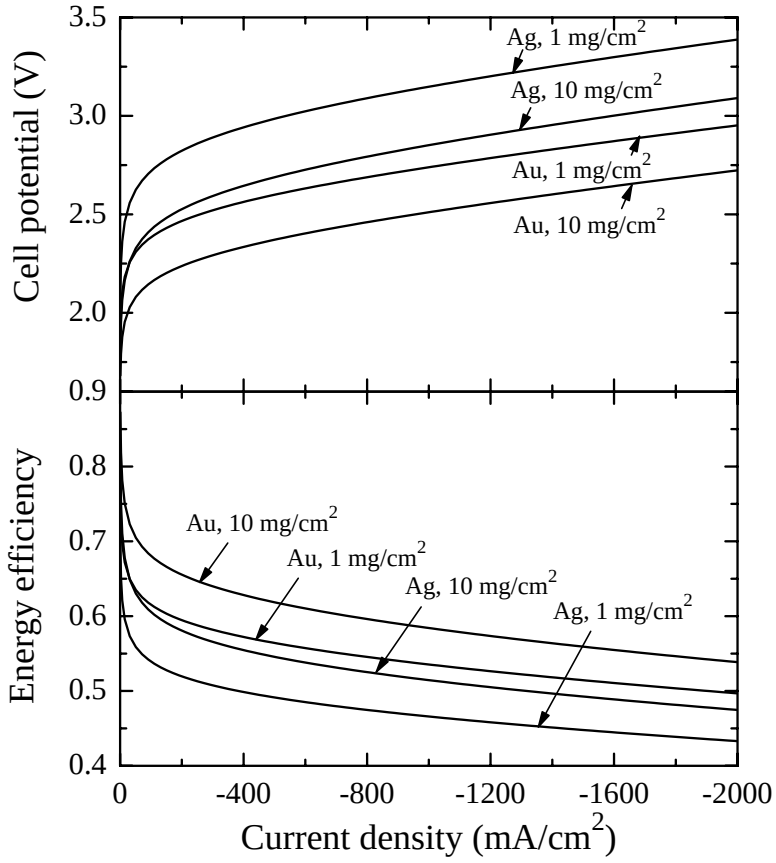

Figure 4.15: Simulated cell potential and energy efficiency for an electrolysis cell using a porous anion-exchange membrane as buffer layer.

Figure 4.15 presents simulated cell potentials and energy efficiencies for Au-based and Ag-based cells (using a porous AEM as BL) as a function of the current density, and for two different catalyst loadings at the cathode. The loading of 10 mg/cm^2 is similar to what we have used experimentally, and therefore the same active surface areas per cell cross-section area ($a^b_{s_c-l}$ and $a^b_{s_a-m}$ for cathode and anode, respectively) as those fitted to the experimental curves were used. Another case study, where the loadings were 10 times lower,

and which may be more representative of a real system, was also examined. To this end, values of active surface areas per cell cross-section area for anode and cathode were divided by 10. Simulations show that an order of magnitude decrease in catalyst loadings results in ca. 5% loss in energy efficiency. A Au-based cathode with a loading of 1 mg/cm^2 still retained 50% energy efficiency at -2 A/cm^2, which is pretty satisfactory. Of course, some of the assumptions we have made are pretty coarse, e.g., for the description of transport phenomena in the porous AEM and the absence of any residual resistance in the cell, but on the other hand, the values of active surface areas per cell cross-section area that we found for our system are pretty low and could probably be increased significantly, through the use of catalyst powders with a higher specific surface area or through an improved manufacturing of the MEAs.

4.5 Conclusion

The cell design for CO_2 reduction to CO (with simultaneous H_2O reduction to H_2) that we proposed in chapter 1 with a silver catalyst at the cathode is tested here with two different gold catalysts for which the overpotential for CO evolution is lower. In order to understand this atypical design, based on a pH-buffer layer between the cathode catalyst layer and the cation-exchange membrane, a mathematical model of the cell is set forth. Because some of the reactions (and interfacial mass transfer) have fast kinetics, a general framework for treating them as equilibrated in the model is presented, and successfully applied to the cell. This framework shows how to derive proper modified material balances (and boundary conditions) using those that were eliminated from the set of equations and replaced by the equilibrium relationships of the independent equilibrated reactions. It also shows that some of the transport equations (Nernst-Planck equations or Stefan-Maxwell equations) have to be removed and replaced by a number of modified transport (algebraic) equations which equals the number of independent equilibrated reactions. Using the model, a complete analysis of the cell operation is performed in order to understand the experimental data better.

At low current density, the model predicts the experimental data pretty well, using the rate constant values obtained on flat Ag and Au electrodes, and reported in chapter 3. It allows for adjusting the active surface area per cross-sectional area of cell, found equal to 13 and 6 for silver and gold catalysts, respectively. The influence of CO_2 partial pressure in the cathode gas channel and of the salt concentration in the buffer layer was studied both experimentally and with the model, and it confirms that the rate-determining step for CO evolution reaction likely involves CO_2 species as the reactant, and not HCO_3^-, in harmony with the literature, and with chapter 3 (study on flat electrodes). The model reveals that there are very likely some convection effects in the buffer layer (because of gaseous CO_2 evolution at the buffer layer/membrane boundary) in order to account for the high current densities at which the cell can operate. The disagreement between the base-case model and the experimental results at high current density is explained by two effects: A high resistance develop in the buffer layer because of a high gas volume fraction arising from CO_2 evolution at the boundary between the buffer layer and the membrane. This may contribute to the large ohmic contribution in the experimental $i - V_c$ curves. Another effect is the flooding of the gas-diffusion layer that may account for the loss of CO current efficiency at high current density. The transient behavior of the cell is also examined, both experimentally and using the model. Experiments show a loss of CO efficiency over time, which is more severe on the supported Au catalyst than on the unsupported one. Also, because there is a net water flux from anode to cathode that progressively dilutes the electrolyte in the buffer layer, an increase of the cell resistance upon operation is expected. This last effect is analyzed using the model, and it explains why the experimental run time of the cells operating at high current density was limited to a few hours. However, this effect does not seem to have an impact on the loss of CO efficiency experimentally observed, suggesting additional side effects, like catalyst poisoning or accumulation of unidentified CO_2-reduction products in the BL. The overall cell behavior is also examined. The base-case model overestimates the energy efficiency of the cell, especially at high current density. Interestingly, the model is used to predict the performance of a cell design that would rely on a porous anion-exchange

membrane layer instead of the present buffer layer. Simulations reveal that the cell can operate at high current density with an acceptable polarization.

4.6 Appendices

4.6.1 Binary diffusion coefficients of gaseous species

The binary diffusion coefficient $\mathscr{D}_{ij,g}$ (in cm^2/s) between gaseous species i and j is calculated according to[80]

$$\mathscr{D}_{ij,g} = \mathscr{D}_{ji,g} = 1.834\ 10^{-5} T^{1.5} \frac{\left(\frac{M_i+M_j}{M_i M_j}\right)^{0.5}}{p_{T,g}\sigma_{ij}^2 \Omega_D}, \tag{4.54}$$

with T the absolute temperature in K, p_T the total pressure of the gas in bar, and M_i the molar mass of species i in g/mol. One has $\sigma_{ij} = (\sigma_i + \sigma_j)/2$, with σ_i the Lennard-Jones characteristic length of gaseous species i in nm. Ω_D is expressed as

$$\Omega_D = \frac{A}{T^{*B}} + \frac{C}{\exp(DT^*)} + \frac{E}{\exp(FT^*)} + \frac{G}{\exp(HT^*)}, \tag{4.55}$$

with $A = 1.06036$, $B = 0.15610$, $C = 0.19300$, $D = 0.47635$, $E = 1.03587$, $F = 1.52996$, $G = 1.76474$, $H = 3.89411$, and $T^* = k_B T/\sqrt{\varepsilon_i \varepsilon_j}$, where k_B is the Boltzmann constant (1.38065×10^{-23} J/K) and ε_i is the Lennard-Jones energy of gaseous species i in J.

4.6.2 Cell resistances under zero direct current

The table 4.5 presents the experimental resistances measured by impedance spectroscopy (at high frequency) for the buffer-layer-based cells with different cathodes, before electrolysis.

The uncertainties on resistance are pretty high, which underlines the poor reproducibility from one cell assembly to another. Given the large uncertainties, $R_{\mathrm{A-RE}}$ and $R_{\mathrm{C-RE}}$ sum up to $R_{\mathrm{C-A}}$, as one expects. The main resistance contribution to the overall cell resistance is

Table 4.5: Resistances measured before electrolysis by impedance spectroscopy (at high frequency) between the cathode and the reference electrode (RE), the anode and the RE, and the cathode and the anode, with the current always flowing between the cathode and the anode. Values are referred to the cross-sectional area. The uncertainties are evaluated based on Student statistics on a series of 6 to 10 resistance measurements on similar cells. *: Only two measurements, hence no uncertainty is provided.

	$R_{\mathrm{WE-CE}}$ (Ω cm^2)	$R_{\mathrm{WE-RE}}$ (Ω cm^2)	$R_{\mathrm{CE-RE}}$ (Ω cm^2)
Cathode based on unsupported Ag (Alfa)	6.4±0.9	1.1±0.2	5.3±1.1
Cathode based on unsupported Au (Alfa)	9.8±2.4	1.9±0.3	8.9±2.4
Cathode based on supported Au (E-TEK)	6.4±0.3	1.7*	6.3±0.4

between the anode (A) and the reference electrode (RE), whereas that between the cathode (C) and the RE is significantly smaller. It seems that the total cell resistances are significantly larger for the cells based on unsupported Au (Alfa) as compared to those based either on unsupported Ag (Alfa) or on supported Au (E-TEK).

From the model parameters, the total cell resistance is ca. 2 Ω.cm^2 (1.58 Ω.cm^2 for the BL + 0.39 Ω.cm^2 for the CEM + 0.02 Ω.cm^2 for the DM, based on parameters from tables 4.1 and 4.2), with that between the cathode and the RE amounting to ca. 0.96 Ω.cm^2 and that between the anode and the RE amounting to ca. 1.03 Ω.cm^2. Those values are lower than those found experimentally, especially for $R_{\mathrm{A-RE}}$. The resistance of the current collectors or contact resistances may contribute to these additional resistive contributions at zero current. Furthermore, we have observed that the cell resistance may go up substantially when direct current is passed, as displayed in figure 4.4. Possible reasons for this dependence on current were also discussed in the text.

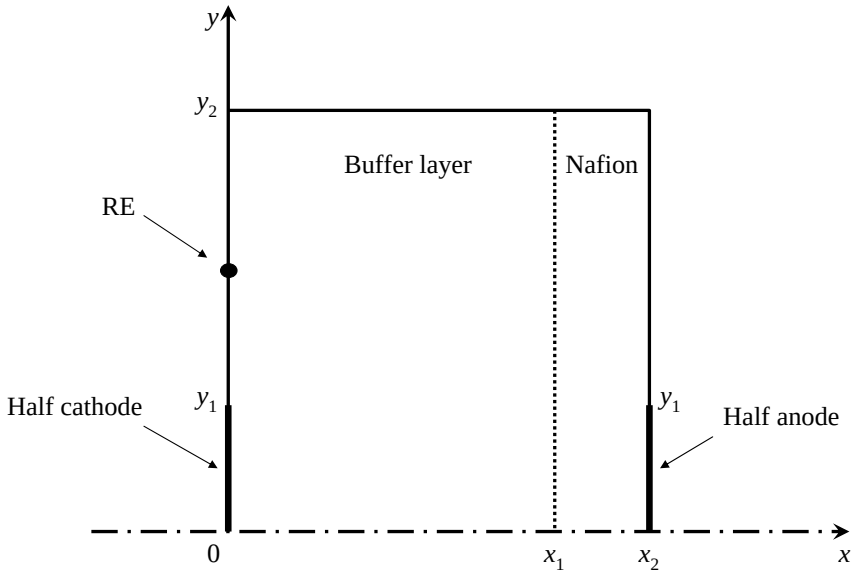

Figure 4.16: Half view of the electrolysis cell showing the actual RE placement

4.6.3 Reference electrode placement

The goal of this appendix is to get a deeper insight into the reference electrode placement one would choose in a 1-D model. In the actual cell setup, the reference electrode is positioned on the cathode side, 1 cm away from the center of the cathode along the y axis (figure 4.16). A primary-current-distribution analysis is performed in order to determine the equipotential lines in such a system. Laplace equation is solved everywhere but at the internal and external boundaries

$$\nabla^2 \Phi_2 = 0, \tag{4.56}$$

where Φ_2 is the potential in the ion-conducting phases (liquid phase of the buffer layer and Nafion). At the electrode/electrolyte boundaries, the potential Φ_2 is set. At the boundaries between the insulator and the electrolyte, the current density along x, i_x is set to zero

$$i_x = -\kappa \frac{\partial \Phi_2}{\partial x} = 0. \tag{4.57}$$

κ denotes the ionic conductivity of the buffer layer or the Nafion. At the internal boundary between the buffer layer and the Nafion membrane, the continuity of the potential and of the current density along x is considered. Finally, at the boundaries $y = 0$ and $y = y_2$, the current density along y is set to zero

$$i_y = -\kappa \frac{\partial \Phi_2}{\partial y} = 0. \tag{4.58}$$

The equations are cast in finite differences, and the system of equations is solved using Matlab. The input parameters of the model are provided in table 4.6.

Table 4.6: Input parameters for the analysis of the primary current distribution in the BL-type cell.

Buffer layer conductivity (S/m)	κ_{BL}	5.75
Nafion conductivity in the K^+ form (S/m)	κ_{CEM}	4.57
Half-width of the electrode (cm)	y_1	0.5
Thickness of the buffer layer (cm)	x_1	0.08
Thickness of the Nafion membrane (cm)	$x_2 - x_1$	0.0177
Width of the insulator (cm)	$y_2 - y_1$	3.31

The potential distribution is provided in figure 4.17. Because of the small distance between the two electrodes as compared to the electrode size, the potential variation is almost restricted to the region between the cathode and anode, and it is fairly uniform outside. A reference electrode as far as 1 cm from the center of the cathode (along y) falls within this fairly uniform region. The equipotential line at $x = 0$ and $y = 1$ cm cut the x axis at $x = 0.0475$ cm ($y = 0$). This distance is independent on the potential Φ_2 applied at the cathode.

List of Symbols

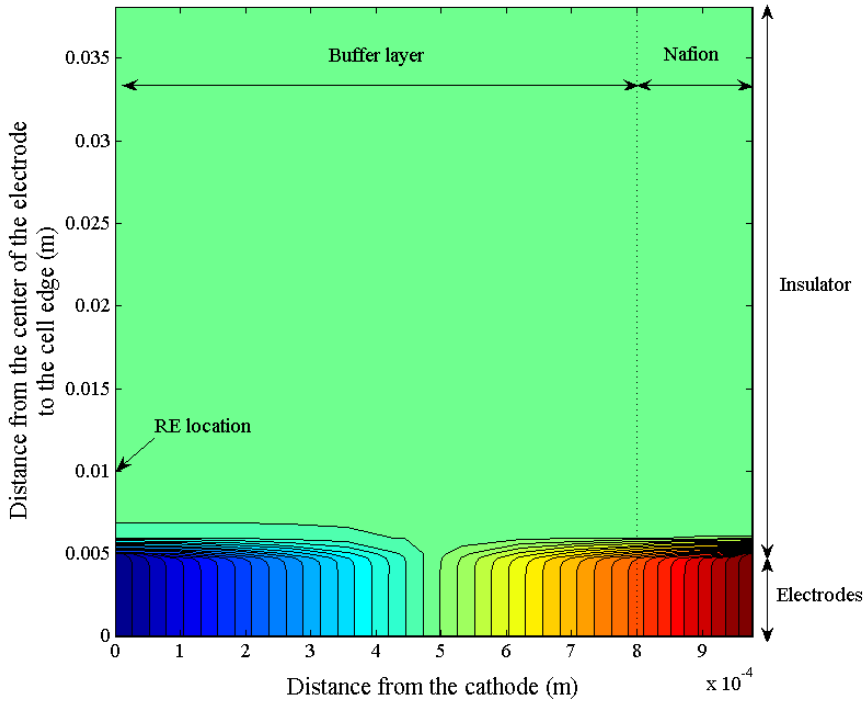

Figure 4.17: 2-D potential distribution in the electrolysis cell. $\Phi_{2A} = -1$ mV and $\Phi_{2C} = 0$.

a_{p-q} Surface area of interface between phases p and q per unit volume of medium (1/m)

a^b_{p-q} Surface area of interface between phases p and q per cross-sectional area of the cell at a boundary

b constant term due to nonideality of the membrane phase (J/mol)

$c_{i,p}$ Concentration of species i in phase p (mol/m^3)

c^0_i Initial concentration of component or species i (mol/m^3)

$c_{T,p}$ Sum of concentrations of species in phase p (mol/m^3)

$\mathbf{d}_{i,p}$ Driving force of species i in phase p (J/m^4)

$D_{i,p}$ Diffusion coefficient of species i in phase p (m^2/s)

$\mathscr{D}_{ij,p}$ Binary diffusion coefficient for interaction between species i and j in phase p (m^2/s)

F Faraday's constant (96,487 C/mol)

f_i Activity coefficient of component or species i

h Mesh interval for finite differences (m)

$\mathbf{i}$ Current density (A/m^2)

i_x Current density along x (A/m^2)

i_y Current density along y (A/m^2)

k_B Boltzmann's constant (1.38065×10^{-23} J/K)

$k_{f,k}$ Forward rate constant of reaction k (units depend on reaction; see table 4.1)

K_k Equilibrium constant of reaction k (units depend on reaction; see table 4.1)

M_i Molar mass of species i (g/mol)

$\mathbf{N}_{i,p}$ Flux density of species i in phase p (mol/m^2 s)

n_k Number of electrons exchanged in electrochemical reaction k

n_p Number of phases

n_r Number of reactions

n_r^b Number of reactions at a boundary

n_{r_e} Number of independent equilibrated reactions

$n_{r_e}^b$ Number of independent equilibrated reactions at a boundary

n_{s_p} Number of species in phase p

$p_{i,p}$ Partial pressure of species i in phase p (bar)

$p_{T,p}$ Total pressure of species i in phase p (bar)

p_0^{vap} Water vapor pressure (bar)

R Ideal-gas constant (8.314 J/mol K)

R Resistance (Ω m^2), referred to the cross-sectional area

R_k Rate of reaction k (mol/m^2 s for a heterogeneous reaction and mol/m^3 s for a homogeneous reaction)

R_k^b Rate of reaction k at a boundary (mol/m^2 s)

$\mathcal{R}_k$ Rate of reaction k times the volume fraction of the phase (homogeneous reaction) or times the surface area per unit volume of medium (heterogeneous reaction) (mol/m^3 s)

$\mathcal{R}_k^b$ Rate of reaction k at a boundary times the surface area per cross-sectional area of the cell (mol/m^2 s)

$s_{i,k}$ Stoichiometric coefficient of species i in reaction k

T Temperature (K)

V Cell potential (V)

V_c Electrode potential vs. a specified reference electrode (V)

$\bar{V}_{i,p}$ Partial molar volume of component i in phase p (m^3/mol)

$\mathbf{v}_p$ Superficial fluid velocity within phase p (m/s)

x Distance across the cell from cathode gas channel (m)

$x_{i,p}$ Mole fraction of species i in phase p

y Distance along the gas channel (m)

y_{CM} Number of moles of cations C^+ (H^+ or K^+) over the total number of moles of cations in the membrane

z_i Charge of species i

β_k Charge transfer coefficient of reaction k

δ_l Thickness of layer l (m)

ϵ_p Volume fraction of phase p

ε_i Lennard-Jones energy of gaseous species i (J)

Γ_i Activity coefficient of species i

κ Conductivity (S/m)

Φ_1 Electric potential of the electron-conducting phase (V)

Φ_2 Electric potential of the ion-conducting phase (V)

η_i Integral number of moles of species i per cross-sectional area of cell (mol/m^2)

η_i Current efficiency for species i

λ Water content in the membrane phase

$\mu_{i,p}$ Electrochemical potential of species i in phase p (J/mol)

θ_i fractional surface coverage of adsorbed species (or empty site) i

σ_1 Electronic conductivity of the solid phase (S/m)

σ_i Lennard-Jones characteristic length of gaseous species i (nm)

σ_{ij} Arithmetic mean of Lennard-Jones characteristic lengths of gaseous species i and j (nm)

superscript

b Variable or parameter defined at a boundary

eff Effective value of diffusion coefficient, because of tortuosity

subscript

A Anode

BL Buffer layer

C Cathode

CEM Cation-exchange membrane

g Variable or parameter relative to the gas phase

l Variable or parameter relative to the liquid phase

m Variable or parameter relative to the membrane phase

RE Reference electrode

s Variable or parameter relative to the solid phase

s_a Variable or parameter relative to the anode catalyst

s_c Variable or parameter relative to the cathode catalyst

$\square$ Empty sites

Bibliography

[1] K. Ushikoshi, K. Mori, T. Kubota, T. Watanabe, and M. Saito *Applied Organometallic Chemistry*, **14**, 819–825, 2000.

[2] *Syntrolysis*. http://www.inl.gov/factsheets/docs/syntrolysis.pdf, last date accessed 2010.

[3] Y. Hori, K. Kikuchi, and S. Suzuki *Chemistry Letters*, **11**, 1695–8, 1985.

[4] Y. B. Vassiliev, V. S. Bagotzky, N. V. Osetrova, O. A. Khazova, and N. A. Mayorova *J. Electroanal. Chem.*, **189**, 271–294, 1985.

[5] S. Ikeda, T. Takagi, and K. Ito *Bulletin of the Chemical Society of Japan*, **60**, 2517–22, 1987.

[6] M. Azuma, K. Hashimoto, M. Hiramoto, M. Watanabe, and T. Sakata *Journal of Electroanalytical Chemistry and Interfacial Electrochemistry*, **260**, 441–5, 1989.

[7] M. Azuma, K. Hashimoto, M. Hiramoto, M. Watanabe, and T. Sakata *Journal of the Electrochemical Society*, **137**, 1772–8, 1990.

[8] H. Noda, S. Ikeda, Y. Oda, K. Imai, M. Maeda, and K. Ito *Bulletin of the Chemical Society of Japan*, **63**, 2459–62, 1990.

[9] Y. Hori, H. Wakebe, T. Tsukamoto, and O. Koga *Electrochim. Acta*, **39**, 1833–1839, 1994.

[10] M. M. Halmann, *Chemical fixation of CO_2*. CRC press, Boca Raton, FL, 1993.

[11] M. Jitaru, D. A. Lowy, M. Toma, B. C. Toma, and L. Oniciu *J. Applied Electrochem.*, **27**, 875–889, 1997.

[12] C. M. Sanchez-Sanchez, V. Montiel, D. A. Tryk, A. Aldaz, and A. Fujishima *Pure and Applied Chemistry*, **73**, 1917–1927, 2001.

[13] L. Geiser, E. Varesio, and J. L. Veuthey *Journal of Pharmaceutical and Biomedical Analysis*, **31**, 1059–1064, 2003.

[14] A. M. C. Fojas *personal communication*, 2005.

[15] R. L. Cook, R. C. MacDuff, and A. F. Sammells *Journal of the Electrochemical Society*, **135**, no. 6, 1470–1471, 1988.

[16] R. L. Cook, R. C. MacDuff, and A. F. Sammells *Journal of the Electrochemical Society*, **137**, no. 1, 187–9, 1990.

[17] R. L. Cook and A. F. Sammells *US patent*, **US 4,959,131**, 1990.

[18] D. W. Dewulf and A. J. Bard *Catalysis Letters*, **1**, 73–80, 1988.

[19] M. Shibata, K. Yoshida, and N. Furuya *Journal of Electroanalytical Chemistry*, **442**, no. 1-2, 67–72, 1998.

[20] H. Yano, F. Shirai, M. Nakayama, and K. Ogura *Journal of Electroanalytical Chemistry*, **533**, no. 1-2, 113–118, 2002.

[21] R. Kostecki and J. Augustynski *Berichte der Bunsen-Gesellschaft*, **98**, no. 12, 1510–15, 1994.

[22] R. Shiratsuchi and G. Nogami *Journal of the Electrochemical Society*, **143**, no. 2, 582–6, 1996.

[23] S. Ishimaru, R. Shiratsuchi, and G. Nogami *Journal of the Electrochemical Society*, **147**, no. 5, 1864–1867, 2000.

[24] Y. Hori, H. Konishi, T. Futamura, A. Murata, O. Koga, H. Sakurai, and K. Oguma *Electrochim. Acta*, **50**, no. 27, 5354–5369, 2005.

[25] Y. Hori, H. Ito, K. Okano, K. Nagasu, and S. Sato *Electrochim. Acta*, **48**, no. 18, 2651–2657, 2003.

[26] J. R. Varcoe, R. C. T. Slade, and E. Lam How Yee *Fuel Cells*, **5**, no. 2, 187–200, 2005.

[27] A. Z. Weber and J. Newman *Chemical Reviews*, **104**, 4679, 2004.

[28] K. A. Mauritz and R. B. Moore *Chemical Reviews*, **104**, 4535, 2004.

[29] K. D. Kreuer, S. J. Paddison, E. Spohr, and M. Schuster *Chemical Reviews*, **104**, 4637, 2004.

[30] D. M. Bernardi and M. W. Verbrugge *Journal of the Electrochemical Society*, **139**, 2477, 1992.

[31] M. Eikerling, Y. I. Kharkats, A. A. Kornyshev, and Y. M. Volfkovich *Journal of the Electrochemical Society*, **145**, 2684, 1998.

[32] T. E. Springer, T. A. Zawodzinski, and S. Gottesfeld *Journal of the Electrochemical Society*, **138**, 2334, 1991.

[33] T. F. Fuller, *Solid Polymer Electrolyte Fuel Cells*. Ph.D. thesis, University of California, Berkeley, CA, 1992.

[34] A. Z. Weber and J. Newman *Journal of the Electrochemical Society*, **151**, no. 2, A311, 2004.

[35] J. Newman and K. E. Thomas-Alyea, *Electrochemical Systems*. John Wiley & Sons, Inc., NJ, 3rd edition ed., 2004.

[36] T. Okada, H. Satou, M. Okuno, and M. Yuasa *Journal of Physical Chemistry B*, **106**, 1267–1273, 2002.

[37] A. Z. Weber and C. Delacourt *Fuel Cells*, **8**, no. 6, 459–465, 2008.

[38] P. N. Pintauro and D. N. Bennion *Ind. Eng. Chem. Fundam.*, **23**, 230–234, 1984.

[39] J. Newman *Ind. Eng. Chem. Res.*, **34**, 3208–3216, 1995.

[40] D. N. Bennion, "Mass Transport of binary electrolyte solutions in membranes," tech. rep., University of California, Los Angeles, CA, 1966.

[41] P. N. Pintauro and D. N. Bennion *Ind. Eng. Chem. Fundam.*, **23**, 234–243, 1984.

[42] T. Okada, S. Kjelstrup Ratkje, and H. Hanche-Olsen *Journal of Membrane Science*, **66**, 179–192, 1992.

[43] M. Ottoy, T. Frland, S. Kjelstrup Ratkje, and S. Moller-Holst *Journal of Membrane Science*, **74**, 1–8, 1992.

[44] T. Okada, S. Moller-Holst, O. Gorseth, and S. Kjelstrup *Journal of Electroanalytical Chemistry*, **442**, 137, 1998.

[45] A. Z. Weber, *Modeling Water Management in Polymer-Electrolyte Fuel Cells*. Ph.D. thesis, University of California, Berkeley, CA, 2004.

[46] K. S. Førland, T. Okada, and S. K. Ratkje *Journal of Electrochemical Society*, **140**, no. 3, 634–637, 1993.

[47] J. P. Meyers, *Simulation and Analysis of the Direct Methanol Fuel Cell*. Ph.D. thesis, University of California, Berkeley, CA, 1998.

[48] Adam Z. Weber and John Newman *Journal of the Electrochemical Society*, **151**, no. 2, A326–A339, 2004.

[49] G. A. Olah and G. K. Surya Prakash *US patent*, **US 7,608,743 B2**, 2009.

[50] T. Yamamoto, D. A. Tryk, A. Fujishima, and H. Ohata *Electrochimica Acta*, **47**, 3327–3334, 2002.

[51] Y. Hori and S. Suzuki *J. Electrochem. Soc.*, **130**, no. 12, 2387–2390, 1983.

[52] N. Gupta, M. Gattrell, and B. MacDougall *J. Appl. Electrochem.*, **36**, 161–172, 2006.

[53] N. Hoshi, M. Kato, and Y. Hori *J. Electroanal. Chem.*, **440**, no. 1-2, 283–286, 1997.

[54] Y. Hori, A. Murata, K. Kikuchi, and S. Suzuki *Journal of the Chemical Society, Chemical Communications*, **10**, 728–9, 1987.

[55] M. Maeda, Y. Kitaguchi, S. Ikeda, and K. Ito *Journal of Electroanalytical Chemistry and Interfacial Electrochemistry*, **238**, no. 1-2, 247–58, 1987.

[56] H. Noda, S. Ikeda, A. Yamamoto, H. Einaga, and K. Ito *Bulletin of the Chemical Society of Japan*, **68**, no. 7, 1889–95, 1995.

[57] T. Ohmori, A. Nakayama, H. Mametsuka, and E. Suzuki *Journal of Electroanalytical Chemistry*, **514**, no. 1-2, 51–55, 2001.

[58] G. B. Stevens, T. Reda, and B. Raguse *Journal of Electroanalytical Chemistry*, **526**, no. 1-2, 125–133, 2002.

[59] A. W. B. Aylmer-Kelly, A. Bewick, P. R. Cantrill, and A. M. Tuxford *Faraday Discussions of the Chemical Society*, **56**, 96–107, 1973.

[60] E. Lamy, L. Nadjo, and J. M. Savéant *J. Electroanal. Chem.*, **78**, 403–407, 1977.

[61] A. Gennaro, A. A. Isse, M. G. Severin, E. Vianello, I. Bhugun, and J. M. Savéant *Journal of the Chemical Society-Faraday Transactions*, **92**, no. 20, 3963–3968, 1996.

[62] C. Amatore and J. M. Savéant *J. Am. Chem. Soc.*, **103**, no. 17, 5021–3, 1981.

[63] R. Kostecki. Ph.D. thesis, University of Genève, 1994.

[64] R. H. Perry and D. W. Green, *Perry's Chemical Engineers' Handbook*. McGraw-Hill Handbooks, 1999.

[65] D. A. Palmer and R. Van Eldik *Chem. Rev.*, **83**, no. 6, 651–731, 1983.

[66] L. Hsueh and J. Newman *I&EC Fundam.*, **10**, 615–620, 1971.

[67] A. K. Hauser and J. Newman *J. Electrochem. Soc.*, **136**, no. 10, 2820–2831, 1989.

[68] A. K. Hauser and J. Newman *J. Electrochem. Soc.*, **136**, no. 11, 3249–3255, 1989.

[69] J. F. Yan, T. V. Nguyen, R. E. White, and R. B. Griffin *J. Electrochem. Soc.*, **140**, no. 3, 733–742, 1993.

[70] Sunde S. *J. Electroceramics*, **5**, no. 2, 153–182, 2000.

[71] J. Christensen and J. Newman *J. Electrochem. Soc.*, **151**, no. 11, A1977–A1988, 2004.

[72] T. W. Chapman, A. P. Barrios, and Y. Meas *J. Electrochem. Soc.*, **154**, no. 8, D411–D417, 2007.

[73] M. M. Tlili, M. Benamor, C. Gabrielli, H. Perrot, and B. Tribollet *J. Electrochem. Soc.*, **150**, no. 11, C765–C771, 2003.

[74] M. Takahashi, Y. Kobayashi, and H. Takeuchi *J. Chem. Eng. Data*, **27**, 328–331, 1982.

[75] S. Kotrly and L. Sucha, *Handbook of Chemical Equilibria in Analytical Chemistry*. Ellis Horwood Limited, John Wiley & Sons, New York, 1985.

[76] D. D. Wagman, W. H. Evans, V. B. Parker, R. H. Schumm, and I. Halow, *The NBS tables of chemical thermodynamic properties*, vol. 11. The American Chemical Society and The American Institute of Physics for the National Bureau of Standards, 1982.

[77] B. Trémillon and G. Durand, *Préliminaires à l'étude de l'électrolyse*, vol. J1602. Techniques de l'ingénieur, 1999.

[78] P. Kedzierzawski and J. Augustynski *Journal of the Electrochemical Society*, **141**, no. 5, L58–L60, 1994.

[79] P. V. Danckwerts, *Gas-liquid Reactions*. McGraw-Hill chemical engineering series, 1970.

[80] B. E. Poling, J. M. Prausnitz, and J. P. O'Connell, *The Properties of Gases and Liquids*. McGraw-Hill chemical engineering series, 2004.

[81] A. Z. Weber, R. M. Darling, and J. Newman *J. Electrochem. Soc.*, **151**, no. 10, A1715–A1727, 2004.

[82] *Etek Datasheet*. http://www.etek-inc.com, last date accessed 2007.

[83] D. Fan and R. E. White *J. Electrochem. Soc.*, **138**, no. 6, 1688–1691, 1991.